Title
Validation of Multiparametric Magnetic Resonance Imaging Techniques for Evaluating the Prostate

Author
Starobinets, Olga

Publication Date
2017

Peer reviewed|Thesis/dissertation

Validation of Multiparametric Magnetic Resonance Imaging Techniques for Evaluating the Prostate

by

Olga Starobinets

DISSERTATION

Submitted in partial satisfaction of the requirements for the degree of

DOCTOR OF PHILOSOPHY

in

Bioengineering

in the

GRADUATE DIVISION

of the

[redacted]

Acknowledgements

Elements of this dissertation have been published elsewhere. Chapter 2 was published in *Abdominal Radiology*. Chapter 3 was published in *Journal of magnetic resonance imaging : JMRI*. Chapter 7 has been accepted for publication in *NMR in Biomedicine.*

First and foremost I would like to acknowledge and express my gratitude to Sue Noworolski. She has been my employer, my instructor, my mentor, my research advisor, and very much a role model for over half a decade now. Sue, thank you for your patience, your guidance and for taking a chance on me in the first place. When I started in Sue's lab I knew very little about imaging; in fact, I knew absolutely nothing that was useful. Looking back I can only image the level of exasperation I must have caused in those early days. Sue has not only taught me about imaging and programming, study design and scientific writing, she has shown by example how to achieve that elusive work/life balance and to celebrate small victories whenever they come. Sue's work ethic, her immense technical knowledge and abilities, her enthusiasm, dedication, and genuine concern for others served as inspiration throughout this sometimes lengthy journey and helped me navigate those moments of doubt, which we all inevitably struggle with.

I would also like to thank John Kurhanewicz. John is one of the kindest people I know. He always has something positive and encouraging to say. John is extremely busy, sometimes I wonder if he ever sleeps but he has always made time to meet with me, review my abstracts, discuss my papers, and in general be this positive supportive force. John, your appreciation and devotion to science, your vision, and dedication to research are inspiring and reassuring. I am extremely grateful to have had you as my mentor and advisor.

Natalie, I don't think I could have made it through the last few years with my sanity intact if not for you. You've been my cube mate, my partner in crime at conferences, my sounding board, my cheerleader, and one of my best friends. I'll be haunting our cube till you graduate. You are one the most hard-working and dedicated people I have ever met. You have pushed me to be a better person and a better scientist and I have no doubt that you will succeed, exceed, and be brilliant at anything you choose to pursue. I'll genuinely miss you but I think we are friends for life, confined spaces, blood, sweat, and tears will do that to two people.

I've had the privilege to meet and work with some fantastic people while at UCSF. Justin, thank you for being such a kind and supportive friend and for equanimity with which you allowed Natalie and me to drag you to lunches, dinners, and happy hours. I have utmost faith in you and your abilities. I know you'll make an excellent doctor and I can't wait to cheer you on as you reach your goal. Thank you, Sonam, for your positive energy and happy outlook on life. While you are thriving under the Swedish sun, we still miss you a ton! Thank you, Chris, for organizing happy hours and getting us out of the lab. Jed, thanks for always, always being ready and happy to help. Lorenzo, thank you for coffee runs and for making me laugh even through the longest, toughest days. I would also like to thank Antonio Westphalen for sharing his knowledge and for his willingness to help enthusiastically and with good cheer.

I wouldn't be where I am today without my family. I'd like to thank my parents for bravely leaving their lives behind and immigrating with three kids, no money, and very limited English to this country. Thank you for teaching us hard work and unwaveringly believing in us. I'd like to thank my siblings, who still know nothing about prostates, yet manage to be extremely supportive. I would especially like to thank my husband. Artem, you have been my rock through this journey - a very intelligent, funny, loving, kind, and supportive rock. I couldn't have asked

for a better partner. I appreciate your patience and sense of humor more than you know. Thank you for making me laugh and enjoy life. My final, final thank you goes to our unborn daughter, who is approaching 36 weeks as I'm writing. While your dad and I can't wait to meet you, thanks for staying put and allowing me to finish this, kiddo!

Dedicated to my amazing family

Abstract

Validation of Multiparametric Magnetic Resonance Imaging Techniques for Evaluating the Prostate

by

Olga Starobinets

Prostate cancer is extremely common. With recent advancements in cancer detection, an increasing number of men at a younger age face the difficult choice between delaying potentially life-saving interventions and seeking curative treatments, which are typically accompanied by a host of side effects. Non-invasive disease characterization is a promising step toward identifying patient-specific cancer management strategies. Due to the excellent performance of anatomic imaging and the ability to characterize physiologic properties via functional imaging modalities, multiparametic magnetic resonance imaging (mpMRI) has the potential to make a significant impact on the way prostate cancer is viewed by both patients and clinicians.

This thesis will introduce multiparametric MR imaging in the context of prostate anatomy. It will address the issues of aligning MR imaging to the whole-mount histopathology images (commonly regarded as a reference standard) and discuss characterization and stratification of prostatic lesions based on mpMR imaging. This work will also introduce a semi-automatic approach to lesion segmentation on histopathology and report on the prostate cancer composition in the radical prostatectomy population. Furthermore, this thesis will investigate the prevalence of "sparse" prostatic lesions, discussing their clinical significance and exploring mpMRI capabilities to detect these cancers. Finally, this work will examine the influence of prostate treatments, specifically 5-alpha reductase inhibitors (often used to treat benign prostatic

hyperplasia), on the structure of prostatic tissues, their effect on the appearance of prostatic tissues on mpMRI, and what role such treatments play in our ability to properly detect malignancies post treatment.

Table of Contents

List of Figures

List of Tables

Symbols and Abbreviations

5-ARIs = 5α-reductase inhibitors

ACR = American College of Radiology

ADC = apparent diffusion coefficient

AR = androgen receptor

AUC = area under the receiver operating characteristics curve

AS = active surveillance

BPH = benign prostatic hyperplasia

COV = coefficient of variation

DCE = dynamic contrast-enhanced

DHT = dihydrotestosterone

DRE = digital rectal exam

DWI = diffusion weighted imaging

ECE = extra capsular extension

EPE = extra prostatic extension

EPI = echo planar imaging

ERC = endorectal coil

FOV = field of view

FSPGR = fast spoiled gradient echo

FSE = fast spin echo

GS = Gleason Score

Gd-DTPA = gadopentetate dimeglumine

GVF = gradient vector flow

HGPIN = high-grade prostatic intraepithelial neoplasia

K_{ep} = rate constant between extracellular extravascular space and plasma space

K^{trans} = volume transfer constant

MP = multiparametric

MRSI = magnetic resonance spectroscopic imaging

PCa = prostate cancer

PFC = perflurocarbon

PI-RADS = Prostate Imaging Reporting and Data System

PSA = prostate specific antigen

PZ = peripheral zone

ROI = region of interest

SI = signal intensity

SNR = signal-to-noise ratio

SVI = seminal vesicle invasion

TRUS = transrectal ultrasound

Tx = treated

TZ = transition zone

Un = untreated

v_{EES} = fractional extravascular, extracellular volume

v_L = fractional luminal volume

CHAPTER 1

Introduction

Prostate cancer (PCa) is the second leading cause of cancer-related deaths among American men. In 2017 over 160,000 of the US men will be diagnosed with prostate cancer, with almost 27,000 men dying from the disease.[3] Prostate cancer is extremely heterogeneous; some cancers are indolent and can safely remain untreated for decades, while other prostatic malignancies are quick to progress and generally require intervention. Considering the often-indolent nature of the disease and the fact that definitive treatments for PCa are often associated with a host of side effects ranging from incontinence to impotence,[5] active surveillance (AS) has emerged as a preferred option for management of localized low-risk prostate cancer. Active surveillance is an approach based on monitoring prostate cancer while postponing definitive treatments. Despite several reassuring large-cohort, long-term studies indicating the safety of active surveillance[7,8] and studies showing the positive effects of active surveillance on the quality of life,[9,10] AS is still an underutilized management option with >80% of US men eligible for AS choosing to pursue curative treatment instead.[13] This reluctance likely stems from anxiety over misdiagnosed cancer and worry over missed progression to high-risk disease. These concerns are understandable since the current, conventional methods for diagnosing and tracking prostate cancer, consisting of digital rectal exam (DRE), prostate specific antigen (PSA) testing, and ultrasound guided prostate biopsies, come with a host of limitations and may result in under-grading and under-staging of PCa.[14] The ushering of the active surveillance era puts a more urgent emphasis on our ability to accurately locate, characterize, and monitor the disease. Multiparametric magnetic resonance imaging (mpMRI), a noninvasive imaging technique that can be used to identify and locate prostate cancer, offers an appealing alternative to the

conventional methods for PCa diagnosis. In this thesis, we introduce multiparametric MR imaging in the context of prostate anatomy and address some of the challenges associated with tissue characterization using mpMRI and issues involved in validation of mpMR imaging for accurate PCa diagnosis.

In Chapter 3, we present a semi-automatic software-based method of registering in vivo prostate MR images to digital histopathology for unmolded prostates, as well as prostates that have been molded prior to fixation to simulate distortion due to the endorectal coil. Accurate mapping between in-vivo MRI and digitized pathology is extremely important in establishing validity of imaging findings. The presented software was shown to successfully morph histology-based prostate images into corresponding MR images. Percent overlap improved from 80.4±5.8% prior to morphing to 99.7±0.62% post morphing. Molded prostates had a smaller distance between landmarks (1.91±0.75mm) versus unmolded (2.34±0.68mm), indicating a better alignment of internal structures within the prostate, but this did not reach statistical significance.

The study presented in Chapter 4 characterized prostate cancers and validated mpMRI in detecting PCa and predicting PCa aggressiveness by correlating mpMRI findings with whole-mount histopathology. Logistic regression (LR) was used to identify optimal combinations of parameters to separate benign from malignant tissues, clinically significant disease from PCa considered clinically unimportant, as well as low-risk from high-risk PCa within the peripheral and the transition zones of the prostate. MpMRI was shown to provide excellent separation between benign tissues and PCa, and across PCa tissues of different aggressiveness. The final models prominently featured spectroscopy and dynamic contrast-enhanced (DCE)-derived

metrics (two modalities often undervalued in mpMRI acquisition) underlining their importance within a comprehensive mpMRI exam.

Chapter 5 presents a new semi-automatic technique for lesion segmentation, accurate region contouring and region area estimation on whole-mount histopathology slides. The chapter describes the development of a software-based segmentation procedure and covers the user initialized gradient vector flow (GVF) active contouring technique used to obtain accurate cancer region outlines. This approach was shown to perform well even when applied to "subjective" contours (such as dotted outlines). Additionally, this technique was demonstrated to be robust to the variations in user initialization and to perform well for regions within a wide range of sizes. The coefficients of variation computed as part of a repeatability study were small ranging from 0.0018 to 0.0166, indicating the overall robustness of the technique.

In Chapter 6 we establish the incidence and Gleason grading of sparse lesions on whole-mount histopathology in post-prostatectomy samples, identify the imaging characteristics of sparse cancers on mpMRI modalities, and discuss their clinical implications. Based on the histopathology findings, sparse cancers were found to be entirely low grade in the transition zone and predominantly low-grade (83%) in the peripheral zone and thus overall likely pose limited malignant potential for spread and progression. On imaging, sparse low-grade cancers and sparse higher-grade disease were shown to have similar imaging characteristics to dense low-grade PCa. However, statistically significant differences were found between sparse low-grade cancers and benign tissues on several imaging modalities within the peripheral zone, indicating the value of mpMRI for focal treatment planning.

Chapter 7 discusses the effects of treatments on prostate mpMR imaging; more specifically, this study investigated how 5α-reductase inhibitors (often prescribed for patients

with enlarged prostates due to benign prostatic growth) affect the discrimination between low-grade prostate cancer and benign tissues on mpMRI. A better separation between low-grade cancerous and benign regions was observed for prostatic tissues exposed to 5-ARIs for the majority of the MR measures of interest and overall with an mpMRI approach. Additionally, a reduction in the coefficient of variation was noted for most of the MR measures in the treated cohort when compared to the untreated group. Of clinical interest, these findings suggest that pretreatment with 5-ARI may facilitate a better discrimination of low-grade prostate cancer from benign tissues with mpMRI.

Chapter 8 provides a summary of the findings and their clinical implications. It also discusses potential future directions and applications for mpMRI.

CHAPTER 2

Background

Parts of Section 2.2 of the following chapter are reprinted from "Practical aspects of prostate MRI: hardware and software considerations, protocols, and patient preparation" by Olga Starobinets, Natalie Korn, Sonam Iqbal, Susan M Noworolski, Ronald Zagoria, John Kurhanewicz, and Antonio C Westphalen. The manuscript was published in *Abdominal Radiology* in May 2016 (41(5): 817-830). Olga Starobinets, Natalie Korn, and Sonam Iqbal conducted the literature review and co-wrote the publication. Susan Noworolski, Ronald Zagoria, and John Kurhanewicz edited the manuscript. Antonio Westphalen defined the scope of the review and supervised the project.

2.1 Prostate Cancer

One in 7 men in the US will be diagnosed with prostate cancer during his lifetime[3]. While more men are being diagnosed at a younger age (with mean age of diagnosis shifting from 70 to 65 years old in the past 30 years[15]), over the last few decades there has been a significant decline in PCa mortality. Between 1991 and 2005, prostate cancer mortality declined by 42% from 103 to 60 deaths per 100,000 men among 50–84 year old males.[16] This trend can be attributed to the improvements in PCa treatments (explaining 22-33% of the mortality decline) but more significantly to the introduction of the prostate antigen specific (PSA) screening.[16] However, the story of PSA screenings is not without controversy. According to a recent study PCa overdiagnosis estimates range from 1.7% to 67%.[17] A 2009 study published in the New England Journal of Medicine found that 1410 men would need to be screened and 48 additional cases of prostate cancer would need to be treated to prevent one death from prostate cancer.[18] To mitigate overdiagnosis and overtreatment of clinically insignificant prostate cancer, in 2012, US

Preventative Services Task Force (USPSTF) issued a recommendation against using PSA-based screening for prostate cancer in men regardless of age.[19] To understand the low sensitivity of PSA screening one has to take a closer look at the prostate gland and the processes that take place there.

The prostate is a small muscular gland located in the pelvis, surrounded by the rectum posteriorly and the bladder superiorly, with urethra running through its center (Figure 2.1). The prostate produces and secretes about 30% of the seminal fluid. In line with its function, the gland is made up of two primary tissues: glandular tissue (facilitates secretion) and fibromuscular tissue (contracts to expel fluids during ejaculation).

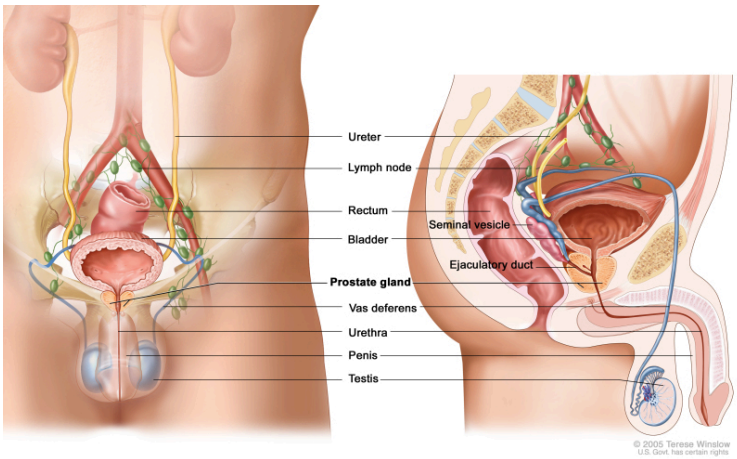

Figure 2.1: Anatomy of male reproductive and urinary systems, showing the prostate gland. A prostate is a walnut sized gland that typically continues to grow throughout a man's life. When enlarged the prostate may obstruct the urine flow by constricting the urethra running through the center of the gland. Large nerve bundle surround the prostate on both sides. In order to preserve erectile function, bilateral nerve sparing is desirable during prostatectomy.
Adapted from https://www.ncbi.nlm.nih.gov/

The prostate is typically divided into the peripheral zone, the central zone, the transition zone, and the fibromuscular stroma (Figure 2.2). The majority of prostate cancers (70-80%) originate in the peripheral zone with the transition and the central zones responsible for the rest.[20] Adenocarcinomas of the prostate are not believed to originate in the anterior fibromuscular stroma; however, cancers originating within the PZ, CZ, or TZ may invade the fibromuscular

stromal tissues.[21] The transition zone is also the site of origin for benign prostatic hyperplasia (BPH), benign growth that can significantly increase the size of the gland, compressing the peripheral zone and constricting the urethra, often resulting in lower urinary tract problems. Additionally, high-grade prostatic intraepithelial neoplasia (high-grade PIN or HGPIN), often seen as a precursor to prostate cancer, is estimated to occur in 15% of men in the 40-49 age group, with HGPIN prevalence continuing to rise with age.[22] Finally, atrophy and prostatitis, inflammation of the prostate (chronic and acute), round up the list of common processes taking place within the prostate gland (Figure 2.2).

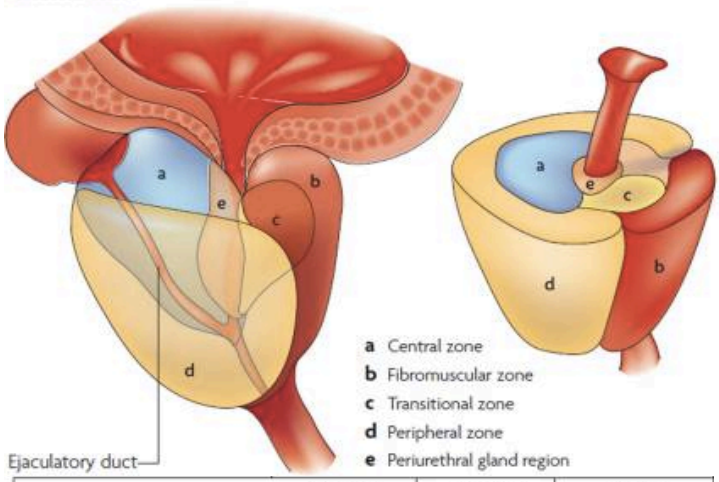

	Peripheral	Transition	Central
Focal atrophy			
Acute inflammation			
Chronic inflammation			
Benign prostatic hyperplasia			
High-grade PIN			
Carcinoma			

High prevalence
Medium-high prevalence
Low prevalence
None

Figure 2.2: Zonal anatomy of the prostate gland with zonal prevalence for disease states.
The majority of cancer lesions occur in the peripheral zone of the gland, fewer cancers are found in the transition zone and almost none arise in the central zone. Chronic inflammation is more prevalent than acute inflammation and can be prominent in both the peripheral and the transition zones. Most benign prostate hyperplasia (BPH) lesions develop in the transition zone. High-grade PIN is mostly found in the peripheral zone. The various patterns of prostate atrophy are also much more commonly found in the peripheral zone, with fewer occurring in the transition zone and only occasional atrophic region found within the central gland.
The figure is adapted from a paper by Angelo M. De Marzo *et al*. Inflammation in Prostate Carcinogenesis. Nat. Rev. Cancer. 2007 Apr; 7(4): 256-269.[1]

How do these processes relate to the sensitivity of the PSA testing? PSA is a glycoprotein produced in the epithelium of the prostate. Under normal circumstances, very little PSA is secreted into the blood stream. However, in the presence of BPH,[23,24] atrophy,[25] prostatitis,[23,24] or prostate cancer[26] the PSA levels in the blood become elevated, indicating the overall presence of atypical processes but limiting the usefulness of PSA as a PCa biomarker.

Fortunately, PSA testing is not the only tool urologists have available for diagnosing prostate cancer. Digital rectal exams involve physicians inserting a finger into the rectum and feeling the prostate (that lies in front of the rectum) for any lumps or anomalies. Predictably, the prostate area accessible for evaluation through such means is rather limited. A recent large-scale study demonstrated a limited value of DRE especially in the setting of normal PSA.[27] PSA testing and DRE examination are considered noninvasive; suspicious findings on these modalities typically trigger transrectal ultrasound (TRUS)-guided biopsy. Gleason grading assigned to the detected malignant prostatic tissues is one of the most powerful predictors of patient outcome.[28]

Around 1.3 million prostate biopsies are performed in the United States every year.[29] Prostate biopsy involves the removal of small tissue samples (typically 10-16 cores are collected) with a needle inserted through the rectal wall under the guidance of an ultrasound. Following the procedure a pathologist assigns a Gleason score to the biopsy specimen.[30] The Gleason grading system is based on the histology patterns of the cancer cells in the stained prostatic tissue sections (Figure 2.3).[11,31] The five basic grade patterns are used to generate a Gleason score, which can range from 2 to 10, by adding the primary grade pattern and the secondary grade pattern. The primary and the secondary patterns correspond to the predominant and the second most common patterns found in the tissue. Due to this comprehensive grading scheme, prostate

biopsy serves as a standard reference for histological diagnosis of prostate cancer. Nevertheless, prostate biopsies have their drawbacks.

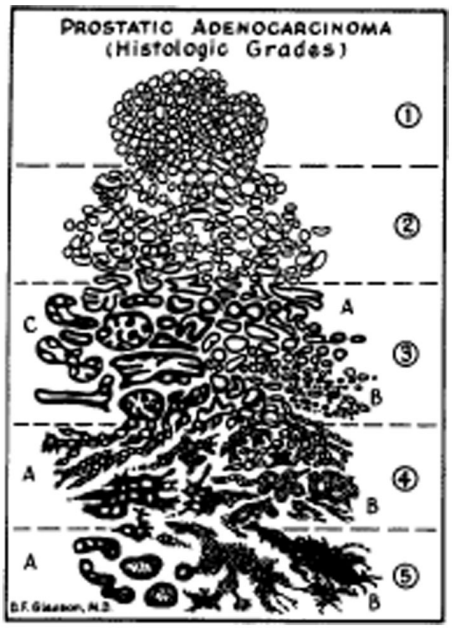

Figure 2.3: Prostate cancer Gleason grading.
Gleason grades reflect the degree of differentiation of prostate cancer. Gleason grades 1 and 2 closely resemble normal prostatic glands. Gleason pattern 2 is characterized by an increase in variability in gland size and shape, as well as increased infiltrations of stroma in-between the glands than is seen for pattern 1. Gleason pattern 3 is the most common grade and is associated with modern level of differentiation. The glandular structure is still recognizable; however, the glands are misshapen, haphazardly spaced, demonstrating irregular extensions into the stroma. Gleason grade 4 is characterized by poorly differentiated cancer growth, with infiltrative fused masses forming chains or strands of malignant epithelial cells. Gleason grade 5 is the most poorly differentiated pattern, typically forming solid sheets of malignant cells, often with a necrotic core. To better characterize prostatic cancer, instead of assigning a single Gleason patter, a Gleason Score, which is the sum of the two most common Gleason grades associated with the tumor (ranging from 2 to 10) is assigned instead[11].
Adapted from Gleason DF. Classification of prostatic carcinoma. *Cancer Chemother Rep.* 1966;50:125–128.[12]

Due to a largely random and limited sampling, with less than 1% of the prostate sampled during the biopsy, prostate cancer may remain undetected (more than 30% of prostate cancers are missed on TRUS biopsies[32]) or the Gleason score of the tumor may be underestimated. Gleason score might be underestimated in as many as 45% of biopsied cases when compared to Gleason grading on post-prostatectomy samples.[32] Additionally, prostate biopsies are not indolent procedures. Complications due to prostate biopsies include pain, infections, prostatitis, cystitis, sepsis, endocarditis, gastrointestinal hemorrhage, hematuria, and urinary symptoms.[33]

While limitations associated with PSA testing and the invasive nature combined with sampling errors of TRUS-guided biopsies paint a grim picture as to the state of PCa screening, eliminating PCa screening altogether is a dangerous prospect. Gulati *et al.* used a simulation

model to predict that discontinuing PSA screening in the US would increase prostate cancer mortality by 13-20% when compared to continued screening.[34] Clearly, an alternative approach is warranted. Imaging (such as provided via mpMRI scans) offers the best alternative means of detecting PCa and differentiating indolent disease from the more aggressive, lethal cancers. By evaluating the entire gland, MRI addresses some of the limitations associated with TRUS-guided biopsies and offers an alternative to strictly ultrasound-guided biopsies through the possibility of both imaging-based disease detection and MR/ultrasound fusion prostate biopsies.[35]

2.2 Multiparametric MRI

2.2.1 Introduction

Magnetic resonance imaging has been used in medicine since the 1980s; however, multiparametric MRI has only recently been introduced into a routine clinical practice for the diagnosis of prostate cancer. MpMRI of the prostate encompasses various sequences, including T1- and T2-weighted MR imaging, diffusion-weighted imaging (DWI), proton magnetic resonance spectroscopic imaging (1H-MRSI), and dynamic contrast enhanced (DCE) MRI,[36,37] shown in Figure 2.4.

As such, in addition to the anatomic data, the mpMRI exam offers information about the microscopic mobility of water (Brownian motion), biochemical characteristics, neovascularity, and cellular structure of the prostatic tissue. Since these characteristics are different for malignant and benign tissues, high-resolution mpMRI provides valuable data that helps to characterize the extent and biological behavior of prostate cancer. Owing to these capabilities, MR imaging of the prostate is increasingly being used to assist patients and clinicians to make management decisions.[38-42]

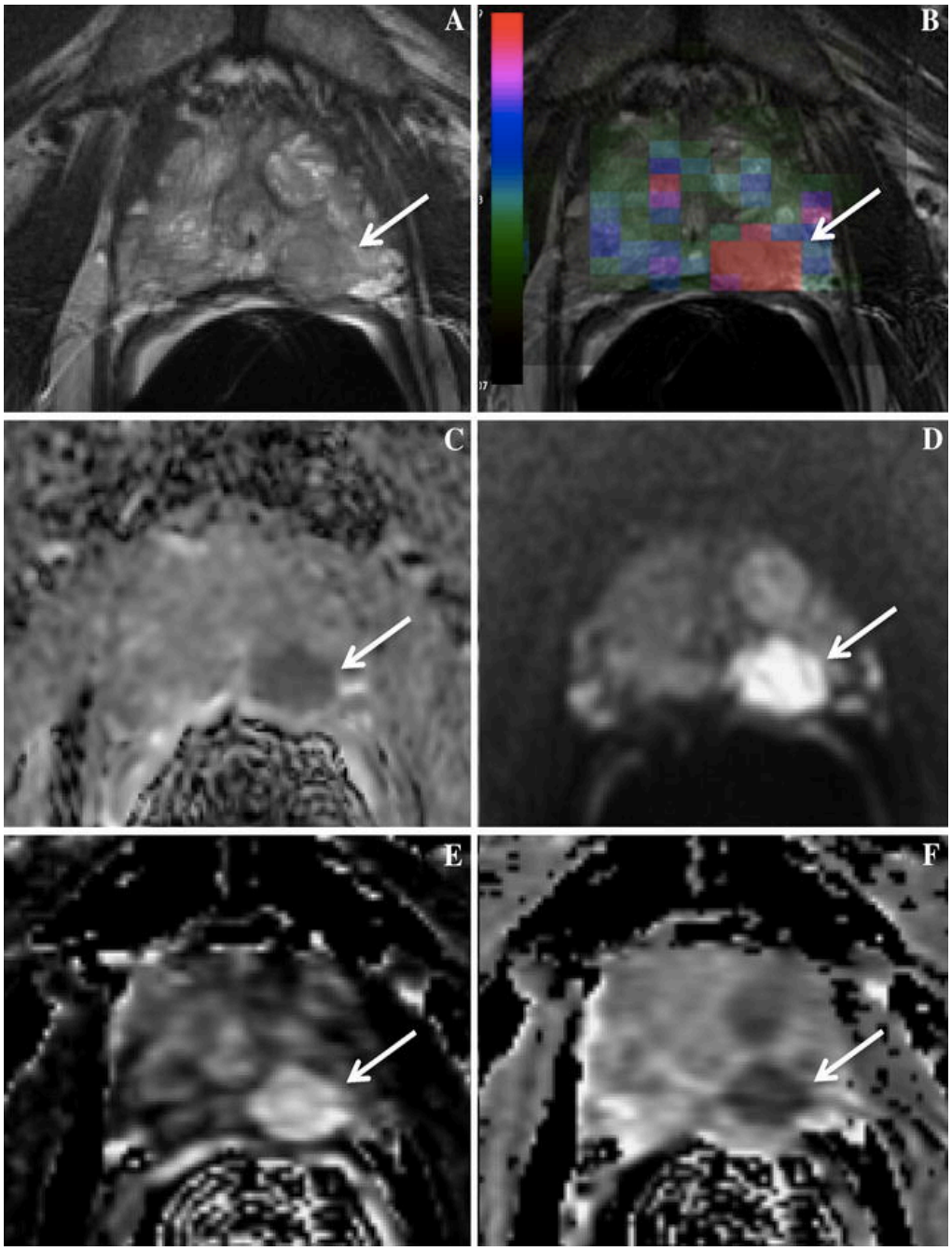

Figure 2.4: Examples of some of the images acquired as part of mpMRI scan.
An untreated 78 year-old man with serum PSA of 9.8 ng/ml showing a a) coil-corrected T2-weighted FSE image, b) MRSI choline metabolite map created in SIVIC[2], c) rFOV ADC map (b=0, 600 sec/mm^2), d) coil-corrected rFOV DWI (b=1350 sec/mm^2), and DCE-derived semiquantitative parameters of e) enhancement slope, and f) washout slope. Subsequent TRUS–MRI fusion-guided biopsy revealed a Gleason 4+3 lesion in the left apex. The cancer region is indicated by the arrow.

The mpMRI exam offers a comprehensive assessment of prostatic tissues using an array of metrics that can be tailored according to the patient's clinical need. Among the main patient-

specific factors that determine optimal mpMRI performance is the patient treatment history.[43] The imaging metrics most relevant to diagnosis may change for imaging patients after radiation,[44,45] focal brachytherapy,[46] hormone treatment,[47,48] and/or surgery.[47,49,50] Additionally, implants associated with abdominal and pelvic comorbidities—such as hip replacements [51,52] or lumbar fusions[53] can significantly affect image quality for certain modalities.

2.2.2 Hardware and Software Considerations

Multiparametric prostate imaging was initially implemented on 1.5 Tesla (1.5T) scanners.[54-62] To acquire scans with diagnostic value, both a pelvic phased array and an endorectal coil (ERC) were used in combination.[63] In prostate MR imaging, ERCs provide a significant improvement in signal-to-noise ratio (SNR) and spatial resolution when compared to pelvic phased array coils alone.[64] This has a profound impact on the quality of the SNR-starved functional imaging; i.e., 1H-MRSI and DWI. Traditional ERCs use a balloon-filled coil that achieves nine-fold SNR improvement over a phased-array alone.[64] After insertion into the rectum, the balloon is inflated, with 40-80 ml of either an inert fluid that matches the susceptibility of the prostatic tissues, e.g. perflurocarbon (PFC) or barium sulfate,[64] or alternatively with air or water. Using an inert fluid instead of air or water improves the homogeneity of the magnetic field and decreases susceptibility artifacts between the rectum and the prostate.[65,66] These inflatable ERCs provide better coverage, are associated with fewer motion artifacts, and are faster to position when compared to rigid coils.[64] Using either a rigid or an inflatable ERC creates an inhomogeneous reception profile which results in higher signal intensity (SI) near the rectal wall and may hinder cancer detection in the peripheral zone. Fortunately, this signal nonuniformity can be easily rectified using readily available coil-correction software.[67]

The introduction of 3-Tesla (3T) clinical scanners presented an opportunity to enhance image quality by trading the increased SNR for improvements in spatial and temporal resolutions, decreasing the necessity of an ERC. However, the SNR increase provided by an ERC can only be partially replaced by a two-fold SNR improvement associated with doubling the magnet strength. Nevertheless, with advances in pulse sequence design, several groups reported that studies done solely with 6 to 32 phased array surface coils at 3T yielded comparable images as the exams conducted with 1.5T scanners with an endorectal coil.[68-72] Comparison studies with and without ERC at 3T have shown increased sensitivity (0.45, no ERC and 0.75, with ERC) and positive predictive value (0.64, no ERC and 0.80, ERC) for prostate cancer detection[73] (Figure 2.5). However, considering patient discomfort, patient preparation, costs, coil placement time, and anatomical distortion associated with ERCs, the use of ERCs in prostate imaging is still being actively debated.

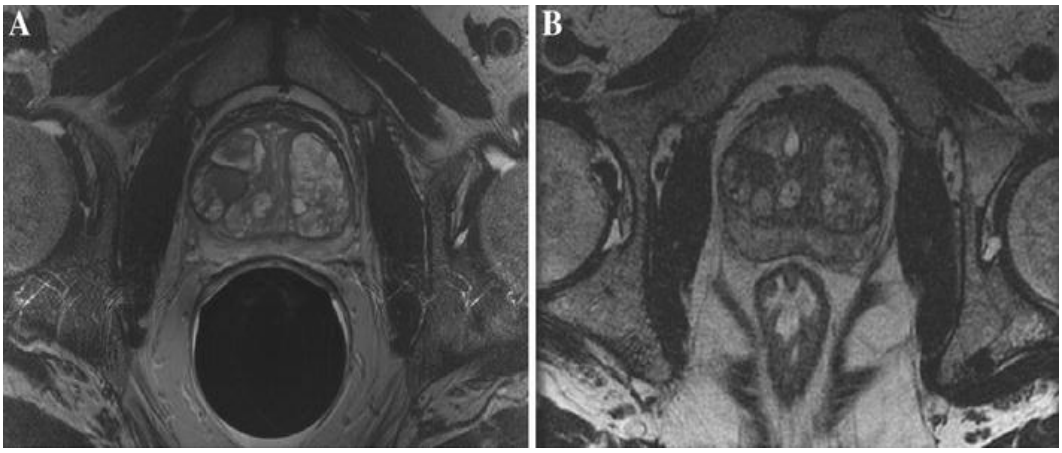

Figure 2.5: T2-weighted images demonstrating differences between acquisitions with and without ERC.
An untreated 66 year-old man with no prior biopsies and serum PSA of 7.9 ng/ml. Oblique axial FSE T2-weigthed images acquired with the same protocol, resulting in 0.35x0.35x3mm in-plane resolution a) with an endorectal coil and b) without an endorectal coil. This patient was scanned twice in three months in anticipation of the MR-guided biopsy. We observe a noticeably increased noise in the image without an ERC, as well as diminished delineation between nodules inside the gland.

2.2.3 Localizer images

Patients are usually scanned in the supine position to maximize patient comfort and minimize respiratory-induced prostate motion between acquisitions. However, when an ERC is not used, the prone position may be a better alternative for some men. Imaging patients in the prone position can result in higher respiratory motion artifacts, but may be necessary to facilitate comfort for certain patients.[74,75] MR imaging of the prostate begins with a low-resolution 3-plane localizer 'scout'. These images are used to locate the prostate and establish the orientation of the coils in relation to the gland prior to scanning.

2.2.4 T1-weighted MR imaging

A multiparametric MR imaging exam of the prostate typically includes an axial large field-of-view T1-weighted scan of the entire pelvis to assess regional lymph nodes for abnormal size, shape, or intensity. Identification of these lymph nodes is facilitated by the T1 contrast between the high signal intensity of visceral fat and lower signal intensity of large or irregularly shaped lymph nodes.[76] To ensure that lymph nodes in the drainage pathway are imaged during the exam, the T1-weighted scan prescription extends superiorly to the aortic bifurcation.[77] T1-weighted imaging is also used to diagnose post-biopsy hemorrhage, which demonstrates high signal intensity.[76] Hemorrhage often has low T2 signal intensity, mimicking cancer, and may introduce significant artifact on DWI and 1H-MRSI, and confound results from DCE MR imaging. For this reason, an interval of at least 6 weeks between the most recent prostate biopsy and the MRI scan is recommended.[78,79] In addition, T1-weighted images may offer an opportunity to detect osseous metastases.

2.2.5 T2-weighted MR imaging

Multiplanar high-resolution two-dimensional (2D) fast spin-echo (FSE) T2-weighted MR images provide exquisite soft-tissue contrast and excellent depiction of zonal anatomy, and are the backbone of MR imaging of the prostate. As mentioned earlier, the majority of prostate cancers are adenocarcinomas that arise within the peripheral zone. Most have low signal intensity against the background of the bright peripheral zone tissue. Similarly to peripheral zone cancers, transition zone lesions usually have low signal intensity on T2-weighted MR images, but can be difficult to distinguish from benign tissue, in particular in the presence of BPH. T2-weighted MR imaging is also the main sequence utilized to assess locoregional spread of cancer;[80,81] the diagnostic accuracy, though, is higher when it is combined with other functional sequences.[82] Prognosis, management, and treatment options of prostate cancer are greatly affected by cancer stage, in particular by the presence of extra prostatic extension (EPE) and/or seminal vesicle invasion (SVI).

High-resolution 2D FSE T2-weighted images are acquired in the true sagittal plane, as well as the oblique axial (Figure 2.4a) and oblique coronal planes of the prostate.[83] Slice thickness of ≥3mm, without a gap, and the in-plane dimension of ≤0.7mm (phase) × ≤0.4mm (frequency) are typically used. For most patients a field-of-view of 12-18 cm allows for the inclusion of the entire gland and seminal vesicles. High-resolution 3D FSE T2-weighted MR imaging has emerged as a promising technique, allowing for the acquisition of isotropic images and saving time by reducing the number of sequences that need to be obtained. However, the quality of the 3D sequence may be limited if acquired on older or low-field magnets. While the T2 contrast is not the same as seen in 2D acquisitions, it is clinically acceptable.[84] Westphalen *et al.* showed that the preference for the 2D or 3D FSE MR images varies widely among radiologists, but without differences in their ability to delineate the anatomy and identify

cancer.[85] This same study did find differences in image sharpness and presence of some artifacts. The 2D FSE images were sharper than the 3D ones, but demonstrated more artifacts (Figure 2.6).

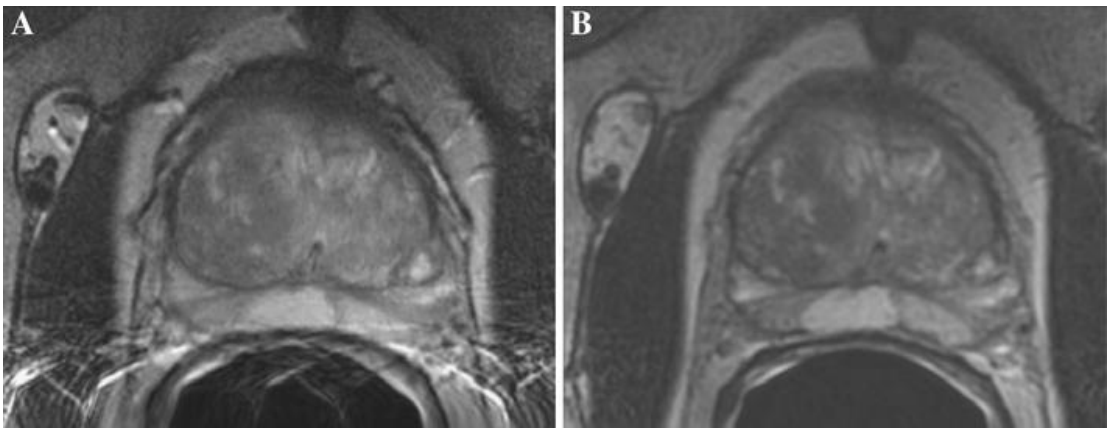

Figure 2.6: Comparison of 2D and 3D FSE T2-weighted MR images.
An untreated 61 year-old man with biopsied Gleason 3+3 prostate cancer and serum PSA of 5.6 ng/ml showing an oblique axial a) T2-weighted FSE anatomic image and b) T2-weighted CUBE anatomic image. The phase-encoding direction aliasing artifact present in the FSE image is not present in the CUBE image. However, the CUBE image is noticeably blurred in comparison to the FSE.

2.2.6 Diffusion-weighted MR imaging

DWI exploits the random motion of water molecules in biological tissues (Brownian motion) to characterize disease. These images are primarily utilized to calculate apparent diffusion coefficient (ADC) maps (Figure 2.4c). The glandular structure of the normal peripheral zone of the prostate compared to the shrunken glands or tightly packed cancerous tissue defines a well-established contrast between healthy and tumor tissue on DWI and the corresponding ADC maps.[86] Perhaps not surprisingly, DWI has been shown to increase the sensitivity and specificity of multiparametric MR imaging for the detection of prostate cancer.[87-89] It has also been shown to improve the assessment of tumor aggressiveness when combined with conventional T2-weighted imaging, with an inverse relationship between the ADC map intensity and the Gleason score.[90] A threshold of approximately 850×10^{-6} mm^2/s has been used to distinguish between low- and high-grade tumors.[91] Yet, because of substantial overlap of ADC values seen in BPH

and cancers, and variability across the various imaging platforms and due to different acquisition parameters, a qualitative visual assessment may be preferred.

Adequate characterization of the random motion of water requires information about its movement in multiple directions. Accordingly, DWI is usually comprised of at least three separate acquisitions, each measuring diffusion in a different direction. Due to this unique sequence structure, DWI is particularly prone to artifact from patient motion between directional acquisitions. To mitigate this problem, images are usually acquired with an echo-planar imaging (EPI) pulse sequence, designed to decrease scan time.

For pelvic cancer detection on 3T scanners, the b-value is generally divided into mid (between 500 and 800 s/mm^2) and high (between 1000 and 2500 s/mm^2) b-values (Figure 2.4d).[92,93] Scanning on older magnets usually excludes b-values above 1000 s/mm^2 due to limits in gradient hardware. Using a lower b-value emphasizes extracellular effects in the resulting ADC maps, whereas using a high b-value emphasizes intracellular motion. Recently, it has become popular to utilize more than one b-value for the assessment of prostate cancer. Imaging with a mid-range b-value will normally have a greater SNR, which can result in finer resolution and a decreased number of signal averages per image. However, a high b-value acquisition reduces the signal from normal prostatic tissue, increasing the sensitivity to abnormal cellular environments.[94] One method of gaining the advantage of contrast of a high b-value while still having the high SNR and fine resolution of a lower b-value acquisition is to extrapolate and compute the theoretical image output for higher b-values.[95] These images show higher SNR than traditional DWI collected with the equivalent high b-values, and can be utilized on older 1.5T scanners where gradient hardware may not allow acquisition with high b-values.[96]

In addition to more heavily diffusion weighted images, a low b-value image is acquired with a b-value in the range of 0 -100 s/mm^2.[97] This image serves as a reference, to fit a slope to the signal per b-value per direction, which is combined to define the ADC map. Additionally, the lower b-values aid in removing the effect of perfusion on the resulting ADC map.

DWI is heavily affected by susceptibility artifacts, which increase in magnitude with higher field strength.[98] Images acquired with EPI, in particular, suffer from severe susceptibility artifact at the interfaces of tissue with air, blood, or fecal matter in the rectum. Performing a rectal enema before the exam reduces susceptibility artifact from air or fecal matter in the rectum.[99,100] A promising recent development for artifact reduction is reduced field-of-view imaging, which has been shown to improve image quality and contrast between tumor and healthy tissue, as well as to decrease susceptibility artifact in prostate DWI (Figure 2.7).[101]

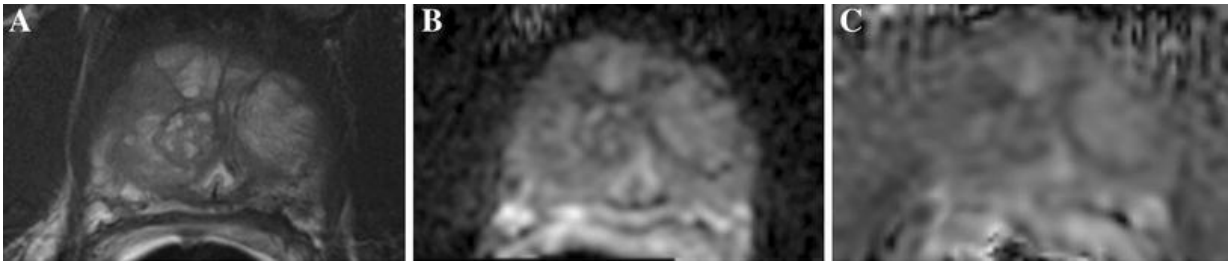

Figure 2.7: Comparison of reduced and full FOV ADC maps.
An untreated 74 year-old man with biopsied Gleason 3+3 prostate cancer and serum PSA of 6.85 ng/ml. An oblique axial a) T2-weighted FSE anatomic image, b) rFOV ADC map, and c) full FOV ADC map show the advantages of the rFOV method for distinguishing boundaries of the prostate and BPH nodules within the prostate. We also see susceptibility artifact from a node of fecal matter or air in the medial rectum, which significantly blurs the rectal wall on c) and less so on b).

2.2.7 Proton magnetic resonance spectroscopic imaging

Proton magnetic resonance spectroscopic imaging is a technique used to study in-vivo cellular metabolism, and has been established as a powerful technique for assessing patients with prostate cancer. Benign and malignant tissues can be differentiated based on the metabolic changes associated with prostate cancer.[102,103] Normal prostatic glandular epithelial cells produce

and secrete high levels of citrate (2.5-2.7ppm).[104,105] Prostate cancer disrupts the epithelial tissues and triggers a metabolic shift from citrate production to citrate oxidation; the overall effect is a substantial reduction in citrate levels in malignant prostate tissues (Figure 2.8).[106-108]

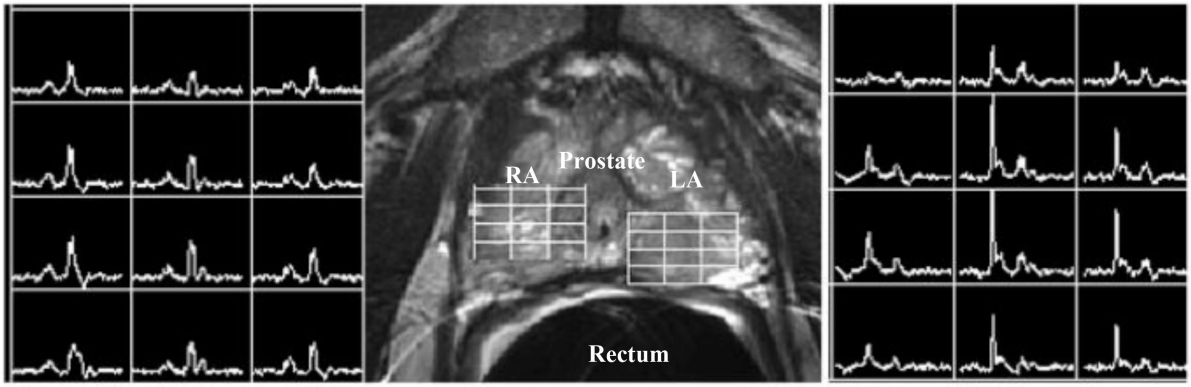

Figure 2.8: Example of magnetic resonance spectra in benign and malignant prostate tissues. An untreated 78 year-old man with serum PSA of 9.8 ng/ml. MRSI demonstrating highly elevated choline (right panel) in the left apex (LA), drastically different from the contralateral healthy tissues (left panel) in the right apex (RA) that demonstrate the presence of citrate without elevated choline. Subsequent TRUS–MRI fusion-guided biopsy revealed a Gleason 4+3 lesion in the left apex.

Furthermore, increased cell density and elevated cell membrane turnover leads to increased levels of choline (3.21ppm) in prostate cancer (Figure 2.4b).[109-111] Creatine (3.02ppm) is another metabolite of interest; it is maintained at a relatively constant level in both healthy and malignant prostatic tissues and serves as an internal reference.[108] Lastly, some groups found it informative to track metabolic changes associated with polyamine.[103] Polyamines (especially spermine) are found in healthy prostate epithelial cells, and similar to citrate, their levels are dramatically reduced in prostate cancer.[112]

Due to the multifocal nature of prostate cancer, a high-resolution metabolic mapping of the entire prostate is required for accurate cancer localization and diagnosis. The 1H-MRSI acquisition has evolved from single voxel spectroscopy to 3D 1H-MRSI that is typically acquired using phase encoding in all three directions, but is time-consuming. Improvements in pulse sequence design have enabled the acquisition of metabolic information from the entire prostate at high resolution within less than 7 minutes with voxel sizes ranging from 0.2cm^3 to 0.5

cm^3, making 1H-MRSI a clinically feasible technique.[113,114] These include using flyback echo-planar readout gradients to improve efficiency and robustness to errors and non-uniform undersampling, and compressed sensing to accelerate the acquisition.[115,116] A number of techniques have been used to reduce the negative effects of periprostatic fat, including outer volume saturation (OVS) with very selective suppression (VSS) pulses,[117] band selective inversion with gradient dephasing (BASING)[118,119] and spectral-spatial radiofrequency pulses.[120,121]

The 1H-MRSI sequence is usually prescribed off the axial T2-weighted MR images with a volume selected to maximally cover the prostate while excluding the seminal vesicles, periprostatic fat, and as much of the rectum as possible. Standard post-processing involves zero-filling, apodization using Gaussian or Lorentzian filtering, and Fourier transform of the free induction decay signal, as well as baseline and phase corrections.[2,122-124]

Interpretation of 1H-MRSI data is often done on a voxel-by-voxel basis, which can be time consuming and introduce interobserver variability. An alternative approach to review these metabolites is to observe peak area ratios, such as the choline+creatine to citrate ratio within each voxel: choline and creatine are typically combined due to signal overlap. In 2004, Jung *et al*. proposed a standardized scoring system for peripheral zone tissues based on metabolic data, ranging from 1 (definitely normal) to 5 (definitely cancer).[125] And in 2007, Futterer *et al*. introduced standardized thresholds for differentiation of benign and malignant tissues in the peripheral zone and central gland of the prostate.[126] Several studies reported significant correlations between peak area ratios and Gleason scores;[127,128] yet, interpretation can be hindered by choline contamination from the seminal vesicles or urethra,[108,129] or by prostatitis,[130,131] which can result in false positive findings.

2.2.8 Dynamic Contrast-Enhanced MR Imaging

Dynamic contrast-enhanced MR imaging (DCE MRI) follows the time course of tissue enhancement post contrast agent injection to evaluate the properties of tissue microstructure and neovascularity. Prostate cancer brings about changes in the cellular structure of the tissues, which result in altered interactions of the tissues with the injected contrast. It is believed that MR contrast agents do not reach the lumen of the healthy glandular tissues.[132,133] Conversely, prostate cancer is marked by the loss of the basement membrane outside the glandular epithelial cells, which allows the contrast to enter the glands, resulting in a greater and faster tissue enhancement seen in DCE studies. In addition to continuing alterations in tissue microstructure, prostate cancer progression is also associated with neoangiogenesis.[134-138] The rapid growth and division of tumor vasculature results in disorganized, irregularly shaped, immature vessels.[139-141] DCE takes advantage of the unique characteristics associated with the abnormal tumor vasculature to assess aggressiveness of the disease. The usefulness of DCE in detecting, localizing, and staging prostate cancer is well documented in literature.[87,142-146] Additionally, several studies have reported promising findings on the utility of DCE parameters in discriminating prostate cancer based on aggressiveness of the disease.[147,148] While DCE is an invaluable sequence in certain instances where other acquisition sequences will show artifact (i.e. for patients with hip replacements), DCE results might be confounded by the presence of prostatitis in the peripheral zone [36,39,149] or by mixed BPH nodules in the transition zone.[21,36,39,150]

DCE imaging is often done with a 3D Fast Spoiled Gradient Echo (3D-FSPGR) pulse sequence. T1-weighted images are collected before, during, and after administration of a contrast agent. A DCE scan is often preceded by a T1 mapping, a measurement of the native tissue relaxation time (T10) obtained using a series of volume acquisitions with variable flip angle

values. Once the native T1 mapping is complete, several pre-contrast dynamic T1-weighted volumes are acquired to establish a baseline. The contrast agent is administered as an intravenous bolus at a rate of 2-4 ml/s followed by a 20 ml saline flush using a power injector. To ensure patient safety, patient's kidney function should be evaluated prior to contrast injection. Estimated glomerular filtration rate (eGFR) based on the blood creatinine levels are often used as indicators of kidney health. Once injected, the contrast agent does not penetrate the healthy prostate glands but collects in the extravascular extracellular space (EES), where it serves to shorten local relaxation times, producing high signal intensity on T1-weighted images. The contrast is cleared from the blood via renal excretion.

DCE MRI studies typically utilize weight adjusted (0.1 mmol/kg of body weight) paramagnetic gadolinium chelate gadopentetate dimeglumine (Magnevist), gadobutrol (Gadovist), or gadodiamide (Omniscan).[151] Aiming for a reasonable spatiotemporal resolution, a five-minute DCE acquisition yields dynamic imaging with a temporal resolution in the range of 3-10 seconds, a spatial resolution in the range of 0.7 x 0.7mm to 1.9 x 1.9mm with a slice thickness of 3-4mm.[60,95,147,148,150,152-156] Compressed sensing techniques have been implemented into DCE sequences to improve spatiotemporal resolution or increase the coverage. Recently, Rosenkrantz *et al.* reported the use of a high spatiotemporal resolution DCE technique GRASP (Golden-angle Radial Sparse Parallel), which allows for image acquisition with spatial resolution of 1.1 x 1.1 x 3.0 mm and temporal resolution of 2.3s.[157]

Tissue enhancement observed during DCE can be interpreted either by visually inspecting the raw images (qualitative approach) or by using semi-quantitative or quantitative methods.[158-161] The qualitative analysis of the DCE images[162-164] is based on the premise that the blood vessels recruited by the prostate tumors are leaky.[165,166] When the contrast is injected, the

cancerous tissues demonstrate early and rapid enhancement followed by a quick washout, which is noticeably different from a slow and steady enhancement observed for normal tissues. An observer may evaluate regions of interest within the prostate by categorizing the overall enhancement as: 1) persistent - a steady enhancement, usually indicative of benign pathology, 2) plateau – the initial uptake is followed by a constant enhancement, slightly suspicious for malignancy, 3) washout – a sharp uptake is followed by a steep washout, strongly suspicion for malignancy (Figure 2.9). While the qualitative approach is quick and intuitive, it fails to comprehensively assess heterogeneous tissues and is inherently subjective and difficult to standardize among imaging centers.

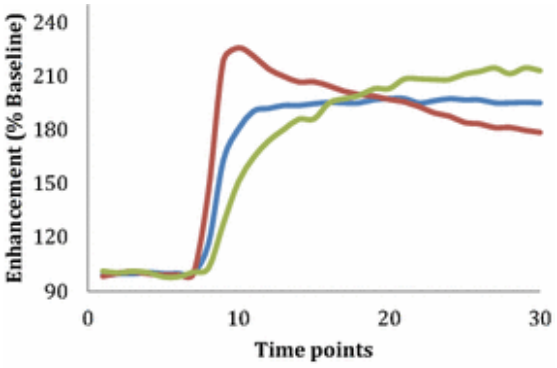

Figure 2.9: Enhancement curves associated with DCE imaging.
Three main types of overall enhancement seen in prostate tissues: persistent enhancement, typically indicative of benign pathology (green); plateau, slightly suspicious for malignancy (blue); and washout, strongly suspicious for malignancy (red).

Semi-quantitative analysis characterizes the enhancement curve on a voxel by voxel basis by calculating curve parameters such as maximum enhancement slope (Figure 2.4e), time to peak, peak enhancement, washout slope (Figure 2.4f), and area under the curve.[148,167] Although this approach is extensively used in the assessment of DCE-MRI, the semi-quantitative parameters provide little physiologic insight into behavior of the tumor vessels and the usefulness of the computed metrics can be limited when comparing data across different imaging protocols. Normalization to muscle has been suggested to aid in generalization of semi-quantitative parameters.[132]

The final approach to analyzing DCE images aims to estimate physiologically interpretable, kinetic parameters by fitting pharmacokinetic models to the enhancement curves.[144,168,169] The most common is the two-compartmental model. The two compartments are the plasma space of the vasculature and the interstitial space between the prostate cells. The two main parameters derived from such models are K^{trans} (the volume transfer constant between plasma and extracellular space, expressed in units of min^{-1}) and v_e (the fractional volume of extracellular space per unit volume of tissue).[146,170-173] While K^{trans} maps offer diagnostically valuable information, acquiring stable measurements from quantitative analysis remains a challenge. Quantitative methods are affected by a number of variables such as changes in cardiac output, accurate tissue T1 and arterial input function (AIF) measurements, as well as the underlying assumptions made by the software packages. Accuracy of T1 measurements is greatly aided by T10 mapping.[174] Ideally, the AIF (the concentration of the contrast agent in the feeding blood supply) is measured for each individual patient in the femoral artery.[175-177] Unfortunately, in a clinical setting, the required temporal resolution may be difficult to achieve. A common approach is to use a population-averaged AIF in the form of a bi-exponential decay.[152] Finally, there are several open source and commercially available software packages for both clinical and preclinical quantitative DCE analysis.[178-182] However, few studies have been done to assess reproducibility of pharmacokinetic measurements obtained with different software packages.

2.2.9 Limitations

Use of mpMRI exams for the diagnosis and staging of prostate cancer has become prominent at medical centers around the world[183-185] and is likely to continue expanding into increasing modalities in the age of precision medicine. However, mpMRI of the prostate did not yet gain the same level of acceptance of other imaging tests; and this is at least in part due to the

use of suboptimal protocols, lack of standardization, and inadequate patient preparation. The American College of Radiology, in conjunction with the European Society of Urogenital Radiology and the AdMeTech Foundation, has developed standards for the Prostate Imaging Reporting and Data System (PI-RADS).[186] Currently in its version number 2, in addition to providing guidelines for interpretation and reporting of mpMRI, PI-RADS establishes the minimum acceptable technical parameters for scanning patients.

Another significant hurdle in widening mpMRI acceptance has to do with difficulties associated with proper validation of imaging with histopathology. Histopathology samples acquired in patients post radical prostatectomy serve as a gold standard for validation studies. However, imaging to histopathology alignment presents serious challenges. The next chapter discusses these challenges and presents a semi-automatic technique for aligning the acquired T2-weighted images to the whole mount histopathology slides.

CHAPTER 3

Semi-automatic Registration of Digital Histopathology Images to In-vivo MR Images in Molded and Unmolded Prostates

Parts of this chapter are reprinted from "Semi-automatic registration of digital histopathology images to in-vivo MR images in molded and unmolded prostates" by Olga Starobinets, Richard Guo, Jeffry P Simko, Kyle Kuchinsky, John Kurhanewicz, Peter R Carroll, Kirsten L Greene, and Susan M Noworolski. The manuscript was published in *Journal of magnetic resonance imaging : JMRI* in February 2014 (39(5): 1223-1229). Olga Starobinets and Susan Noworolski wrote the manuscript. Richard Guo and Olga Starobinets co-wrote the registration software. Olga Starobinets performed the data analyses. Jeffry Simko and Kyle Kuchinsky processed the histopathology. John Kurhanewicz edited the manuscript. Peter Carroll and Kirsten Greene performed radical prostatectomy surgeries. Susan Noworolski conceptualized the study and supervised the project.

3.1 Abstract

The purpose of this work was to evaluate a semi-automatic software-based method of registering in vivo prostate magnetic resonance (MR) images to digital histopathology images using two approaches: 1) in which the prostates were molded to simulate distortion due to the endorectal imaging coil prior to fixation, and 2) in which the prostates were not molded. T2-weighted MR images and digitized whole-mount histopathology images were acquired for twenty-six patients with biopsy-confirmed prostate cancer who underwent radical prostatectomy. Ten excised prostates were molded prior to fixation. A semi-automatic method was used to align MR images to histopathology. Percent overlap between MR and histopathology images, as well as distances between corresponding anatomical landmarks were calculated and used to evaluate

the registration technique for molded and unmolded cases. The software successfully morphed histology-based prostate images into corresponding MR images. Percent overlap improved from 80.4±5.8% prior to morphing to 99.7±0.62% post morphing. Molded prostates had a smaller distance between landmarks (1.91±0.75mm) versus unmolded (2.34±0.68mm), $p<0.08$. Molding a prostate prior to fixation provided a better alignment of internal structures within the prostate, but this did not reach statistical significance. Software-based morphing allowed for nearly complete overlap between the pathology slides and the MR images.

3.2 Introduction

It is estimated that 1 in 7 men in the United States will be diagnosed with prostate cancer during his lifetime.[187] Early and accurate prostate cancer diagnosis is important in managing the disease. With the introduction of prostate-specific antigen (PSA) screening early diagnosis and treatment of prostate cancer became possible.[188] While radical, whole-gland therapy is favored for treatment of advanced, often multifocal prostate cancer, such an approach is associated with a host of long-term genitourinary and rectal side effects.[189] A targeted treatment might be preferred for patients presenting with less advanced disease. Focal treatments however require accurate disease localization, staging, and monitoring.[89,190] MRI imaging is a noninvasive technique that can be used in detection and localization of prostate cancer.[41,191] MRI is poised to play a significant role in the image-guided targeted biopsies and the planning of targeted treatments such as high intensity focused ultrasound (HIFU), radiofrequency ablation (RFA), cryosurgery, photodynamic therapy (PDT) or brachytherapy.[192]

To establish the validity of imaging findings, accurate mapping between in-vivo MRI and digitized pathology images of the resected prostate is essential. Currently there is no established technique that allows for an accurate and timely alignment of postoperative histology images to

preoperative in-vivo MR images obtained with an endorectal coil. Although the endorectal coil introduces prostate deformation, it offers a significant improvement in signal to noise ratio and spatial resolution.[193]

Several factors hinder registration efforts including prostate distortion during scanning, particularly due to an endorectal coil,[194] specimen shrinkage during formalin fixation on the order of 10-15%,[195,196] prostate deformation during surgery, and differences in slicing plane angles.[197] Additional factors such as the time between the MR scan and the surgery may further impede registration.

Registration methods based on anatomical landmarks,[198] fiducial markers,[199] biomechanical modeling,[200] multiattribute combined mutual information,[201] and spatially weighted mutual information[202] have been described in the literature. These can require subjective and time consuming user-intervention,[198,203,204] make assumptions about the tissue distortion,[201,205,206] or require additional information, such as MR imaging of the ex vivo prostate gland[198,203] or placement of fiducial markers.[199,204] The purpose of this study was to evaluate a semi-automatic software-based method of registering digital histopathology images to in vivo prostate magnetic resonance (MR) images using two approaches. These groups were: 1) in which the prostates were molded prior to fixation to replicate the mechanical distortion due to the endorectal coil, and 2) in which the prostates were not molded.

3.3 Materials and Methods

3.3.1 Patients

This study was approved by the Committee on Human Research at this institution and was compliant with the Health Insurance Portability and Accountability Act. Written, informed consent was obtained from all subjects. Twenty-six patients who underwent radical

prostatectomy for a biopsy-proven prostate cancer were studied. Patients who underwent treatment for their prostate cancer prior to surgery or whose surgery was more than 120 days after their MRI were excluded from the study. The patients' mean age was 62.7 ± 5.8 years and the average Gleason score was 7.2, range GS 6 to GS 9. For this study, the time interval between MRI scan and prostatectomy was 23.4 days, ranging from 2 to 97 days. Patient characteristics are summarized in Table 3.1.

3.3.2 MR Imaging

All patients were imaged with an expandable balloon endorectal coil (Medrad, Inc., Indianola, PA, USA) and the GE pelvic phased array on a 3T MR scanner (GE Healthcare, Waukesha, WI, USA). Fast spin echo (FSE) T2-weighted images were acquired in an oblique axial plane with FOV = 18 cm, slice thickness = 3mm, matrix = 256 × 256, and TR/TE = 6000/96. Images were corrected for the inhomogeneous reception profile associated with the combined endorectal coil and pelvic phased array.[207]

Table 3.1: Patient Characteristics

Variable	Molded (N=10)	Unmolded (N=16)
Age (years)	60.4 (6.0)	64.1 (5.3)
Prostate weight (gm)	49.6 (21.4)	43.8 (9.7)
Prostate volume (cm^3)	36.0 (19.0)	29.7 (9.6)
Gleason score	7.0 (1.0)	7.4 (0.9)
Days to surgery	20.5 (14.3)	25.2 (28.9)
PSA (ng/mL)	4.3 (2.1)	8.7 (8.4)
Tumor volume (cm^3)	2.8 (2.9)	5.1 (5.4)

Mean (Standard Deviation)

3.3.3 Molding

After surgery, prostates were weighed and inked. Ten patients had their prostates molded. Molding was accomplished by securing the excised prostate within a plastic mesh basket prior to fixation (Figure 3.1). This basket was made in-house of heat sensitive moldable plastic and was

designed such that the posterior side of the prostate underwent a concave curvature, intended to imitate the inflated endorectal probe. A cover was secured to the anterior portion of the prostate and compressed with rubber bands in the anterior/posterior direction, approximately by 15%, the compression typically observed with an endorectal probe.[194] Prostate dimensions noted on T2-weighted MRI images were provided as a reference for molding. An opening was made in the basket to accommodate the seminal vesicles and vas deferentia.

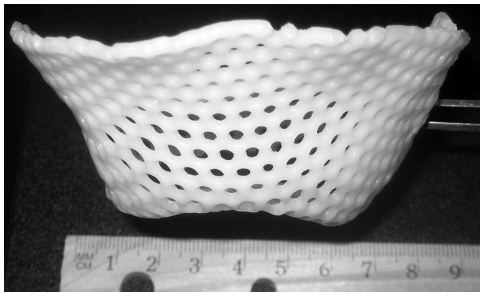

Figure 3.1: The mesh basket. The mesh basket was made in-house out of heat sensitive moldable plastic and was used for molding the excised prostates.

All molded and unmolded prostatectomy specimens were formalin-fixed for at least 24 hours. Prostates were then serially cross-sectioned from apex to base at 3-4mm intervals using a manual meat slicer (Hobart, Troy, OH, USA). Tissue slices were embedded in paraffin, cut as whole-mount histologic sections and stained with hematoxylin and eosin. Slides were arranged from superior to inferior in two columns in an 8.5 x 11 inch space and digitized as a single image per sheet. Ten minutes per prostate were required to complete digitization.

3.3.4 Registration

In-house software written in C and Image Magick (ImageMagick Studio LLC, Landenberg, PA, USA) were used to manipulate the images. The digitized histopathology images were automatically cropped into slices (Figure 3.2a). Label sides were automatically detected based upon more than 5 blue or green pixels found on the right-most or left-most 200 pixels within the image. Extraneous markings were removed automatically by identifying non-violet pixels and surrounding pixels. Images were visually inspected and any remaining

markings removed (Figure 3.2b). Pathology images were visually matched to corresponding axial T2w images according to their level in the prostate and common anatomical landmarks. Prostates were manually segmented from surrounding tissues on T2w images (Figure 3.2c). Manual steps of matching pathology to the MR images and segmenting the prostate on the MR images required 25 minutes per prostate to complete. Pathology slides were automatically centered and rotated to align with the corresponding MR images (Figure 3.2b). Next, pathology images were globally stretched or shrunk to correspond to the T2w images (global alignment). In the second stage, pathology images were stretched or shrunk differently in the right-left direction and in the anterior-posterior direction to match the maximum extent in each direction to that of the T2w images (x-y alignment). In the final stage, each row and each column in a pathology image was stretched or shrunk to match the MRI prostate, first in the left-to-right direction and then in the anterior-to-posterior direction (line-by-line alignment) (Figure 3.2d). Automatic image processing steps required less than a minute to complete.

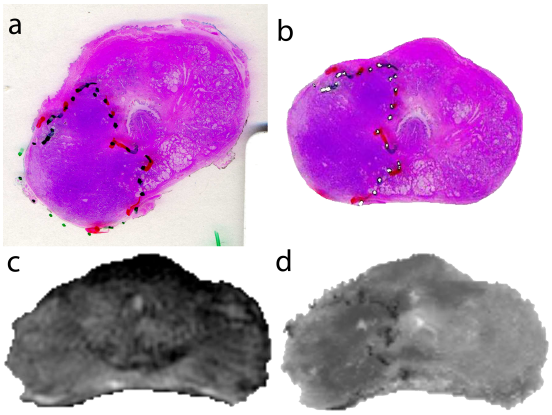

Figure 3.2: Alignment steps: a. Original histopathology slide. b. Cleaned up slide from (a) with background markings removed. c. T2-weighted MR image of a segmented prostate matched to the histopathology slide (b). d. Histopathology slide from (b) aligned to match MR image from (c).

3.3.5 Registration Assessment

The accuracy of registration was assessed in two ways. First, the percent overlap between pathology and MR images was calculated and compared for each alignment stage. Second, three visually identified landmarks marking the boundary of the peripheral zone and the central gland

were placed at approximately midline, then midway between the midline and the left side, and lastly, midway between the midline and the right side on a midgland level in each set of images. Distances between these landmarks in-plane were compared on an aligned midgland pathology slide and on the corresponding MR slice for all cases. Evaluations were made for Stage I – global alignment, Stage II – x-y alignment, and Stage III – line-by-line alignment for both the molded and unmolded cases. Alignment metrics were compared between the molded and unmolded cases. Using the right and the left-side landmark coordinates in-plane rotation angles for landmarks placed on the pathology images and the MR images were computed for molded and unmolded prostates at both x-y and line-by-line alignment stages.

3.3.6 Factors Potentially Impacting Alignment

Gleason Score obtained during surgery, gland volume as measured by visually outlining the gland on the T2-weighted images, gland weight as measured post-surgery, age and serum prostate specific antigen (PSA) within a year of surgery were measured or obtained. The alignment metrics of this study were compared with each of these metrics: Gleason Score, gland volume, gland weight, age, and PSA.

3.3.7 Statistical Methods

Statistical analyses were carried out using JMP software (JMP, Version 10, SAS Institute Inc., Cary, NC). Distances between anatomical landmarks for molded and unmolded prostates were computed. The mean and standard deviation were calculated for the two groups and a Student t-test was performed. The percent overlap mean and standard deviation values were calculated for each stage of the morphing process for molded and unmolded prostates. A Wilcoxon signed rank test of matched pairs for pair-wise comparison of mean values within a patient for percent overlap at each stage in the alignment process was done. For comparisons of

patient characteristics between molded and unmolded, t-tests were done if the distributions were normal, and a Wilcoxon test used if not normally distributed. A p-value of 0.05 was used to define significance.

3.4 Results

Patient demographics are given in Table 3.1, demonstrating no significant difference between molded and unmolded groups in terms of age and Gleason Score ($p>0.1$, t-tests), or in terms of prostate volume, prostate weight, days to surgery, or tumor volume ($p>0.1$, Wilcoxon test). PSA was variable, with a maximum value of 38.5 ng/ml in the unmolded group compared to 8.5 ng/ml in the molded group, and was significantly higher in the unmolded cases, $p<0.05$, Wilcoxon test. Without this outlier of 38.5 ng/ml, which was more than two times higher than any other value in the group, the PSA was not significantly different between the groups.

An example of images from a patient with a biopsy-proven cancer (Gleason 3+3) and a PSA level of 5.5 ng/ml, who underwent prostatectomy, is shown in Figure 3.3.

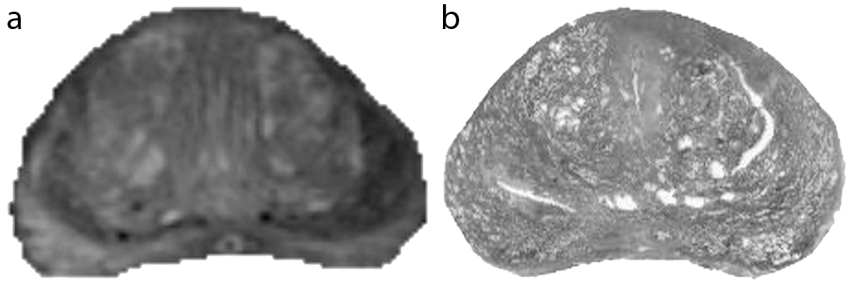

Figure 3.3: Molded prostate: a. A segmented prostate on an axial T2-weighted MR image. b. Corresponding histopathology slide. The excised prostate was molded prior to fixation to mimic the peripheral zone curvature due to the endorectal coil seen on the MR image of the prostate (a).

This excised prostate was molded prior to fixation. Figure 3.3 demonstrates that the compression and induced curvature experienced by the gland in the anterior-posterior direction due to the basket allowed the prostate to better resemble the shape of its MR counterpart, yielding a global alignment %overlap of 85.5%. Figure 3.4 presents the images from a patient with a biopsy-

proven cancer (Gleason 3+4) and a PSA level of 6.2 ng/ml, who underwent prostatectomy. This excised prostate was not molded.

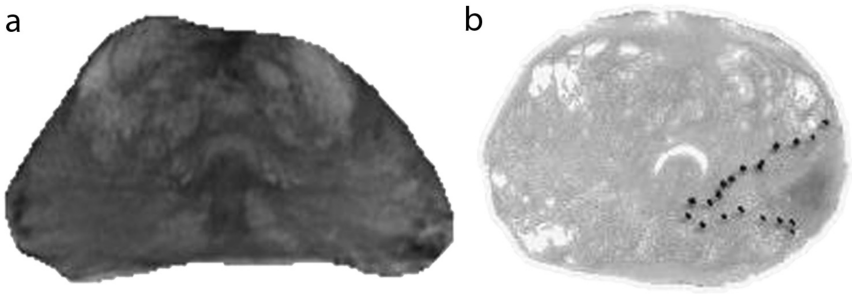

Figure 3.4: Unmolded prostate: a. A segmented prostate on an axial T2-weighted MR image. b. Corresponding histopathology slide. The excised prostate was not molded prior to fixation. Instead of mimicking the peripheral zone curvature due to the endorectal coil seen on the MR image of the prostate (a), prostate in (b) is rounder especially at the peripheral zone and does not exhibit a similar curvature as (a).

Figure 3.4 illustrates that the prostate compression and induced curvature due to the endorectal probe seen on the MR image is not observed on the corresponding histology slice for the unmolded prostate. This case had a %overlap at the global alignment stage of 72.2%, which was less than the molded case of Figure 3.3.

3.4.1 Analyses

When percent overlap between MR images and histopathology was calculated for global, x-y, and line-by-line alignment stages, there were no statistically significant differences between percent overlap values for molded and unmolded groups. With global alignment, molded prostates had 79.1±5.6% and unmolded prostates had 81.6±5.9% overlap with MR images, $p>0.3$. The percent overlap increased to 84.9±5.4% and 84.4±6.3% for x-y aligned molded and unmolded prostates respectively, $p>0.97$. In the final stage of line-by-line alignment, percent overlap reached 99.7±0.46% for molded and 99.7±0.71% for unmolded prostates, $p>0.97$ (Figure 3.5). In a pair-wise comparison, it was determined that on average, percent overlap increased by

3.95% between global and x-y alignment stages, and then by another 15.1% between x-y and line-by-line alignment stages, $p<0.001$.

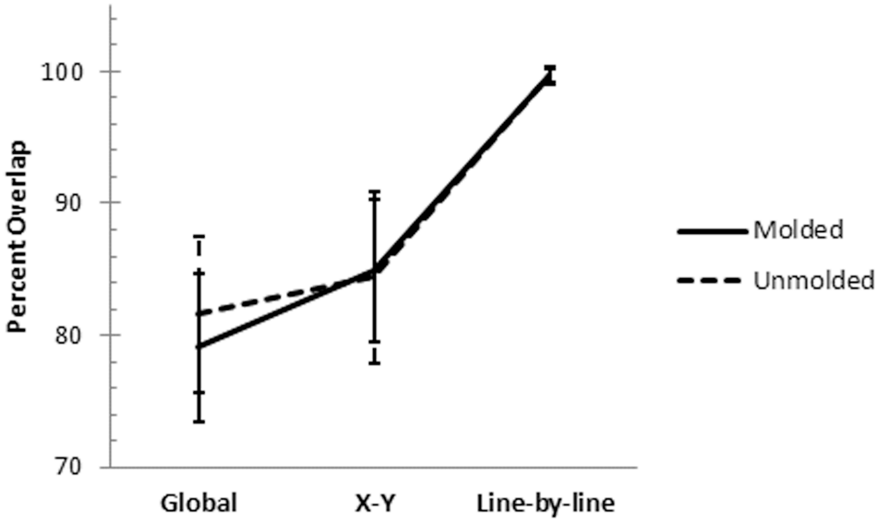

Figure 3.5: Percent overlap between histopathology and MR images at different stages of alignment. Error bars indicate standard deviation.

An example shown in Figure 3.6 demonstrates the three landmarks positioned within the prostate on the MR slice (Figure 3.6a), as well as the corresponding x-y (Figure 3.6b) and line-by-line (Figure 3.6c) aligned histopathology images.

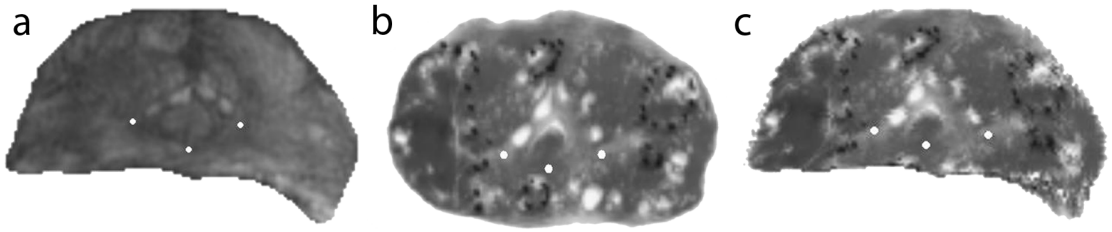

Figure 3.6: Placement of landmarks shown on a. Segmented prostate on an axial T2-weighted MR image. b. Corresponding histopathology slide. c. Histopathology slide from (b) aligned to the MR image from (a).

For each landmark, the in-plane distances between MR and the x-y aligned pathology coordinates were calculated. The mean distance for the three landmarks was determined to be 1.47mm for this case. Also, for each landmark, the distance between the MR and the line-by-line

aligned pathology image was computed; the mean distance for the three landmarks was determined to be 1.13mm. Landmark distances were calculated for midgland slices for all molded and unmolded prostates. For both groups, the landmark distance values were normally distributed. For x-y aligned prostates, the average distance between corresponding landmarks was 2.34±0.68mm for unmolded and 1.91±0.75mm for molded prostates (Table 3.2). There was a trend toward molded prostates having smaller average and maximum landmark distances, but with a p-value of 0.079, the result did not reach significance. For the line-by-line alignment stage, the average distance between corresponding landmarks was 1.67±0.58mm for unmolded and 1.62±0.58mm for molded prostates. With a p-value of 0.422, there were no statistically significant differences between the two groups. There were no differences in the time it took to process the specimens in each group. For every prostate, approximately 45 minutes were required to complete all the alignment steps.

Table 3.2: Three-point landmark distance

Alignment	Molded	Unmolded
X-Y		
Mean (SD)	1.91 (0.75)	2.34 (0.68)
Min, Max (mm)	0.870, 3.08	1.13, 3.54
Line-by-line		
Mean (SD)	1.62 (0.58)	1.67 (0.58)
Min, Max (mm)	0.955, 2.80	0.693, 3.27

SD = Standard Deviation

There was no significant in-plane rotation between the pathology and the MR images, based on the right and left side landmark coordinates. For the x-y alignment stage, the mean rotation angle was -0.58 ±3.1 degrees for unmolded and -1.04±1.30 degrees for molded prostates. With a p-value of 0.48, there were no statistically significant differences between the two groups. For the line-by-line alignment, the mean rotation angle was -0.66±4.21 degrees for

unmolded and -0.59±1.87 degrees for molded prostates. Once again, with a p-value of 0.38, no statistically significant differences between the molded and the unmolded prostates.

No trends for percent overlap or landmark distances were observed to be associated with Gleason Score, tumor volume, prostate weight, PSA, or prostate volume, $p>0.05$ for all comparisons, linear regression. Landmark distances before and after line-by-line alignment significantly increased with age, $p<0.05$, linear regression.

3.5 Discussion

This study demonstrated that computationally morphing the prostate allowed an almost complete overlap of 99.7% between the pathology slides and the MR images with good alignment of internal structures. These results were robust across different prostates, with no bias in alignment when compared to Gleason Score, tumor volume, prostate weight, PSA or prostate volume. The internal alignment was worse for older patients although no statistical corrections were made for the multiple comparisons performed. After the global alignment and the separate x-y stretching/compressing, the average distance between landmarks was 2.17±0.73mm, ranging from 0.87mm to 3.54mm. After the final line-by-line alignment stage, this distance decreased to an average of 1.65±0.57mm, ranging from 0.693mm to 3.27mm. These internal distances between structures were less than the typical distortion caused by the endorectal coil, which are an average anterior-posterior compression of 4.1mm and an average right-left expansion of 3.7mm.[194] This demonstrates that the alignment at least partially compensates for the endorectal coil distortion. Therefore, this technique can be used to align the histopathology to other functional imaging modalities obtained with an endorectal coil such as MR spectroscopy, diffusion-weighted imaging, and the dynamic contrast enhanced MR imaging.

The first part of our registration method entailed a rigid alignment with global stretching/shrinking separately in the x and y directions. We obtained an internal alignment of 2.34±0.68mm for unmolded prostates, which was similar to other studies in the literature, which report registration errors ranging from 2.3 to 2.89mm.[198-200] These studies involved user intervention to identify internal landmarks,[198] additional scanning of the ex vivo prostate, ex-vivo imaging[198,203] and/or fiducial markers[199,204] to guide the histopathology sectioning of the gland. In contrast, our method did not require extensive user intervention or ex vivo prostate scans, which may be difficult to incorporate into a standard clinical protocol. Furthermore, in a clinical setting time efficiency is crucial. Our computational method required less than an hour to align histopathology images for an entire prostate to the corresponding in-vivo MR images, while other groups reported registration times ranging from several hours to several days.[198-200]

The second stage of our alignment incorporated non-rigid registration and resulted in internal alignment to landmarks of 1.67±0.58mm for unmolded prostates, without significant rotation between histopathology and the MR images. These results are similar or better than other automatic alignment methods reported in the literature. Patel *et al.* based an alignment on spatially weighted mutual information, which had virtually the same performance as our method, with 1.65mm registration error, ranging from 1.05mm to 2.03mm.[202] An advantage of their method is that it does not necessitate prostate segmentation from MRI images; however, the results presented in the study were limited to 7 slices collected from 2 patients and require further exploration in a larger cohort. Samavati *et al.* described a biomechanical model-based deformable registration approach and reported a target registration error of 2.1mm for a finite element modeling registration method.[200] For this method, several ex-vivo scans were done and additional magnetic resonance elastography (MRE) studies had to be carried out on the excised

prostate specimens. The sample size in this study was limited to 4 prostates. Other non-rigid methods that used additional information performed slightly better. A method based on user-identified landmarks within both the in vivo and ex vivo prostate resulted in a 1.59mm registration error.[198] However, with the sample size of 3, these findings need to be verified with a larger sample size. The method by Ward *et al*., which based histology specimen slicing on ex vivo MRI with fiducial markers, attained a 1.1mm error in a study of 13 prostate specimens.[199] While our method had a slightly higher registration error, it was similar and did not require scans of the ex vivo gland or time consuming and subjective identification of landmarks within the gland and was evaluated on more, specifically 26, subjects. Overall, compared to others in the literature, our alignment methods produced similar or better results, required less time, and were validated in a larger cohort of patients.

This study also looked at the effects of molding on registration outcomes. Molding the prostate during pathological preparation of the gland provided a better alignment of internal structures within the prostate, but this did not reach significance. Most prostate molding efforts described in the literature involve post formalin fixation molding done with patient-specific molds, which can be expensive and time-consuming to make.[208-210] Formalin fixation makes the gland rigid and tough, limiting the extent to which the prostate can be molded. To avoid this, prostates in this study were fixed while in the molding basket. We saw a trend toward molded prostates having a better alignment of internal structures, which did not reach statistical significance. While molding tended to aid the alignment of internal structures at the x-y alignment stage, the line-by-line alignment seemed to compensate for this, resulting in a similar internal alignment of the molded and unmolded prostates, implying that molding is not required if the line-by-line alignment is performed. The trend in improvement in the alignment of internal

structures post x-y alignment for molded cases versus unmolded cases suggests that further improvements in our molding technique may result in further improvement in alignment.

There were a few limitations to this study. First, we had a single size basket that was used to mold prostates that ranged in size from 15.2ml to 75.8ml. Individualized or tailored sized baskets may have improved the alignment. Second, the compression of the gland varied across subjects. While efforts were made to defer to MR images for guidance, properly modulating compression remains difficult. Third, the alignment of the histopathology slides to the corresponding MR images was done in 2D, which assumes that the prostate specimen was sliced along the same plane as the in vivo MR images were acquired. While the MR images were acquired in an anatomic, axial plane, this may not necessarily match the orientation of the prostate ex vivo, leading to sections obtained at different angles than the MRI. Fourth, we used a manual meat slicer to standardize the slicing of the histopathology sections; if any cases or portions of prostates varied in their shrinkage with fixation, the histology slices may not correspond to the MR images. Fifth, histopathology slices represent microns of tissue whereas the MR images span 3mm of tissue and may not correspond well. Sixth, while our method tried to incorporate mechanical compression to mimic the in vivo prostate deformation and then non-rigid registration, distortion within the gland may have been more pronounced. This could occur when a BPH nodule shifts or expands out of plane or tears the tissue during processing. Other limitations include: 1) the use of subjective, user-identification of the prostate within the MR images and user confirmation or modification of the identification of the prostate within the histopathology images; 2) the use of subjective, user-identified landmarks within the gland to assess the alignment, which may affect the registration metrics. However these landmarks were not used during the alignment procedure, which was automated; and 3) a limited number of cases

were studied, which may have hindered detection of significant differences between the molded and unmolded prostate alignments.

In conclusion, this study presented a semi-automatic alignment method demonstrating an almost complete overlap between histopathology slides and MR images with good alignment of internal structures. While user-intervention was required to segment the prostate in the MR images and to assess and adjust the automatic segmentation, if necessary, on the histopathology, neither user-intervention nor additional scans were required during the alignment procedures. Thus, this is a promising technique for more broad use for alignment of histopathology to MR images. Molding the prostate during pathological preparation of the gland may provide a better alignment of internal structures within the prostate, but this did not reach significance.

CHAPTER 4

Characterization and Stratification of Prostate Lesions Based on Comprehensive Multiparametric MR Imaging Using Detailed Whole Mount Histopathology as a Reference Standard

4.1 Abstract

The purpose of this study was to characterize prostate cancers (PCa) based on multiparametric MR (mpMR) measures derived from MRI, diffusion, spectroscopy, and dynamic contrast-enhanced (DCE) MRI and to validate mpMRI in detecting PCa and predicting PCa aggressiveness by correlating mpMRI findings with whole-mount histopathology. Seventy-eight men with untreated PCa received 3T-mpMR scans prior to radical prostatectomy. Cancerous regions were outlined, graded, and cancer amount estimated on whole-mount histology. Regions of interest were manually drawn on T2-weighted images based on histopathology. Logistic regression (LR) was used to identify optimal combinations of parameters to separate 1) benign from malignant tissues, 2) Gleason Score (GS) 3+3 disease from ≥GS3+4, and 3) low risk (≤GS3+4) from high-risk disease (≥GS4+3) for peripheral zone (PZ) and transition zone (TZ). Performance of the models was assessed using repeated four-fold cross-validation. LR models yielded area under the curve (AUC) of 1.0 when separating benign from malignant tissues in both PZ and TZ. Within PZ, combining apparent diffusion coefficient (ADC), maximal enhancement slope, and choline/creatine yielded AUC=0.82 for separating GS3+3 from ≥GS3+4 PCa. Combining ADC, washout slope, choline/creatine, and choline/citrate yielded AUC=0.80 for discriminating low-risk and high-risk disease. Within TZ, washout slope outperformed any combination of parameters yielding AUC=0.81 for discriminating GS3+3 and ≥GS3+4 cancers.

When separating low-risk and high-risk PCa, combining K_{ep} and choline/creatine yielded AUC=0.83. MpMRI provides excellent separation between benign tissues and PCa, and across PCa tissues of different aggressiveness. The final models prominently featured spectroscopy and DCE-derived metrics underlining their value within a comprehensive mpMRI exam.

4.2 Introduction

Approximately one in seven men in the United States will receive a prostate cancer (PCa) diagnosis during his lifetime.[211] Given the often-indolent nature of the prostate tumors and potentially adverse consequences of the available treatments, accurate disease risk stratification is essential for identifying patient-specific cancer management strategies.[212] Currently, prostate-specific antigen and digital rectal exam are the main diagnostic tools used in prostate cancer screening.[213] Suspicious findings on these noninvasive modalities are typically followed by a transrectal ultrasound-guided biopsy with the assigned Gleason grade of any detected malignancy being one of the most powerful predictors of patient outcome.[28]

Despite this, accuracy of Gleason score based on biopsy findings frequently suffers from inadequate tumor sampling with biopsy Gleason score underestimating actual Gleason score in up to 45% of radical prostatectomy cases. More than 30% of cancers are missed on transrectal ultrasound-guided prostate biopsies altogether.[32] Furthermore, prostate biopsy is not an indolent procedure, and can be associated with discomfort, pain, hematuria, rectal bleeding and risk of severe infection.[214] Multiparametric magnetic resonance imaging is a noninvasive technique that can be used for detection and localization of prostate cancer.

The utility of diffusion weighted imaging (DWI), T2-weighted imaging, magnetic resonance spectroscopic (MRS), and Dynamic contrast-enhanced (DCE) sequences in detecting and localizing prostate cancer is well documented in literature.[39,40] The next pertinent question is

whether mpMRI can be used to accurately determine the aggressiveness of the disease. Several studies have examined various imaging parameters as potential biomarkers for Gleason score, and have yielded mixed results for Gleason score correlations with T2-weighted imaging,[215] ADC,[90,216-218] MRS[127,219] and DCE MRI.[148,217,220] The purpose of this study was to use a logistic regression approach to improve the characterization of prostate cancers based on multiparametric MR measures derived from MRI, diffusion, spectroscopy, and dynamic contrast-enhanced MRI and to validate mpMRI in detecting PCa and in predicting PCa aggressiveness by correlating mpMRI findings with whole-mount histopathology generated from radical prostatectomy specimens.

4.3 Materials and Methods

4.3.1 Patients

This study was approved by the Committee on Human Research at this institution and was compliant with the Health Insurance Portability and Accountability Act. Seventy-eight patients were studied. Two sets of patients were pooled for this study: 1) patients scheduled for surgery, recruited during a urological oncology clinic to receive mpMRI prior to surgery identified prospectively and 2) patients who received mpMRI and then pursued surgical treatment post imaging identified retrospectively. Written, informed consent was obtained from all subjects. Patients who underwent any treatment for their prostate cancer prior to surgery, or whose surgery was more than a year after their MRI were excluded from the study. No MRI exam was performed less than 6 weeks after prostate biopsy.

4.3.2 MR Imaging

All patients were imaged with an expandable balloon endorectal coil (MedRad, Bayer HealthCare LLC, Whippany, NJ) combined with an external phased array coil on a 3T MR

scanner (GE Healthcare, Waukesha, WI, USA). A perfluorocarbon fluid (Galden; Solvay Plastics, West Deptford, NJ, USA) was used to inflate the balloon coil. Fast spin echo (FSE) T2-weighted images were acquired in an oblique axial plane with FOV = 18cm, slice thickness = 3mm, matrix = 512×512, and TR/TE = 6000/96ms. Diffusion weighted imaging (DWI) was acquired using a 2D single-shot spin echo sequence TR/TE=4000/78-90ms, pixel bandwidth = 1952 (conventional acquisition), pixel bandwidth = 1305 (reduced-field-of-view acquisition[101]), b=0 and 600 s/mm^2, slice thickness=3mm. MRSI data was acquired using a 3D flyback, echo planar PRESS CSI acquisition, with a 16×12×10 matrix, acquired at 5.4 mm resolution, zero-filled to 5.4×2.7×2.7mm^3, 0.04cc voxels, TR/TE=2000/85ms,[221] MRSI data was not available in 4/78 subjects. DCE MRI was performed using a 3D fast SPGR sequence with TR/TE = 3.5/0.9ms, flip angle = 5°, slice thickness = 3mm slices, and a single-dose of gadopentetate dimeglumine (Gd-DTPA) (Magnevist; Bayer, Whippany, NJ) over ~5 minutes. The acquisition parameters are outlined in Table 4.1. T2-weighted images and MRSI were corrected for the inhomogeneous reception profile associated with the combined endorectal coil and the external phased array.[67] Apparent diffusion coefficient (ADC) maps were created using an in-house software, from the combined DWI (b=600 s/mm^2) and T2-weighted reference images (b=0 s/mm^2) using Eq. 4.1, where b is the b-value used for the diffusion-weighted acquisition reflecting the gradient strength and duration, S_{gm} is the geometric mean of the signal intensity over the six gradient directions, and S_0 is the signal intensity of the T2-weighted image acquired without diffusion gradients. The calculation was done on a voxel-by-voxel basis.

$$\mathrm{ADC} = -\frac{1}{\mathrm{b}} \ln \left(\frac{S_{gm}}{S_0}\right) \qquad [4.1]$$

Choline, creatine, and citrate levels were quantified by measuring the height of the peaks. Additionally, [Choline+Creatine]/Citrate ([Cho+Cre]/Cit), as well as Choline/Citrate (Cho/Cit) and Choline/Creatine (Cho/Cre) ratios were computed. DCE MRI maps were created based on

the semi-quantitative tissue enhancement parameters of peak enhancement, maximal enhancement slope, and washout rate.[132] Additionally, pharmacokinetic modeling was applied to the data using the assumption that the fractional plasma volume (vp) was 0.01.[222] The concentration of Gd-DTPA in the plasma was modeled as a biexponential Eq. 4.2

$$C_p = AmpD(a_1 e^{-m_1 t} + a_2 e^{-m_2 t}) \qquad [4.2]$$

where Amp=4, D = 0.1mmol/Kg of Gd-DTPA, a_1 = 3.99 kg/L, m_1 = 0.144 1/min, a_2 = 4.78 kg/L, m_2 = 0.011 1/min. The Amp was introduced to account for an offset between our experimental measures and this population average and was determined by minimizing the root-mean-square error (RMSE) of the fits.

A novel pharmacokinetic Luminal Water (LW) model was used.[223] In the LW model, a luminal water fractional volume parameter (v_L) is introduced to the extended Tofts Kermode model.[222] The model is designed based on the assumption that Gd-DTPA does not reach intact prostatic ductal lumen, preventing the water in the lumen from interacting with gadolinium molecules. The non-linear LW model was fitted to data using non-linear least squares estimation with the "optim" function in R (R Foundation for Statistical Computing, Vienna, Austria).[224] The quantitative DCE parameters of the transfer constant (K^{trans}), the fractional extravascular, extracellular volume (v_{EES}), the rate constant (K_{ep}) and v_L were computed. As the LW model is an extension of the Tofts Kermode model, only the LW model was used to avoid redundancy in the parameters and to provide the additional parameter of v_L.

Table 4.1: Scanning parameters

Imaging	PSD	TR/TE (ms)	FOV (cm)	Matrix Size	NEX	ST (mm)	In-Plane Res. (mm)	Temp. Res. (s)	b-value (s/mm²)
T2w	FSE	6000/100	18x18	512x512	1	3	0.35x0.35	N/A	N/A
Conv ADC	ss-EPI	4000/90	24x24	128x128	4	3	0.94x0.94	N/A	0, 600
rFOV ADC	ss=EPI	4000/90	18x9	128x64	6	3	0.70x0.70	N/A	0, 600
MRSI	3D PRESS	2000/85	varied	8x16	1	2.7	5.4x2.7	N/A	N/A
DCE	3D SPGR	3.5/0.9	26x26	256x256	0	3	1.02x1.02	10.417	N/A

PSD=pulse sequence design, ST= slice thickness, Res=resolution, T2w = T2-weighted MRI, Conv = conventional, rFOV=reduced FOV

4.3.3 Histopathology

Post prostatectomy, all prostate specimens were fixed using injected neutral-buffered formalin for at least 24 hours and then serially cross-sectioned from apex to base at 3mm intervals using a manual meat slicer (Hobart, Troy, OH, USA). All slices were then embedded in paraffin as whole-mount sections, cut at 4 micron thickness, stained with hematoxylin and eosin, and examined under light microscopy by the study pathologist with regions of interest marked. The slides were then digitally scanned for comparison to the MR images.

4.3.4 Identifying Regions of Interest

During histological review, cancerous regions on each slide were outlined and graded by the study pathologist using the Gleason system; the amount of cancer in each region was estimated, along with the various fractions of each Gleason grade in each cancer region. Benign tissue regions of cystic atrophy (dilated cystic glands) and normal prostate glandular tissue were also identified and outlined. Next, regions of interest were manually drawn freeform on T2-weighted images based on the digitized histopathology slides using anatomical cues, following a consensus of two readers, keeping within homogeneous regions.

Only the regions containing more than 50% cancer, with regions of interest (ROI) areas larger than 0.05cc were included in the analysis. ROIs were grouped based on region within the prostate (peripheral zone versus transition zone) and tissue of interest – cystic atrophy/normal

tissue or Gleason Grade groups. For each patient, average imaging parameters were computed across the ROIs in question, weighted by the ROI area, resulting in one measure per patient for each tissue grouping.

4.3.5 Statistical Analysis

Statistical analysis was carried out using the JMP software (JMP, Version 10, SAS Institute Inc., Cary, NC). A p-value of 0.05 or less was used to define statistical significance. Descriptive statistics were listed as mean ± standard deviation when normally distributed and as median (first quartile (Q1), third quartile (Q3)) when not normally distributed. Non-parametric Wilcoxon signed-rank paired tests were used to compare all the imaging parameters of interest across tissue types. For the four subjects with missing MRSI data, mean MRSI values over ROIs within the group of interest were substituted for the missing MRSI values in order to include these four patients in the analysis. A stepwise logistic regression analysis was performed for all imaging modalities and combinations of imaging parameters. A forward stepwise logistic regression with a threshold p-value of 0.1 was used to identify the imaging parameters to be included in the combined model. The area under the ROC (receiver operating characteristic) curve (AUC) was computed and its performance was evaluated in distinguishing 1) benign tissues from malignant, 2) GS3+3 disease from ≥GS3+4 PCa, 3) grouped GS3+3 and GS3+4 disease from ≥GS4+3 PCa. Sensitivity and specificity values were also reported. Optimal sensitivity and specificity pairs were chosen off of the ROC curve with the assumption that false negatives and false positives come at similar costs. Separate analyses were carried out for the transition zone and the peripheral zone tissues. To assess performance of each model, repeated k-fold cross-validation with 100 iterations and k=4 was performed.

4.4 Results

No adverse events due to mpMRI scans performed in the course of this study were reported. The patients' mean age was 63.7±6.3 years, the median pre-surgical PSA was 6.2 ng/ml (Q1=4.3 ng/ml, Q3=8.35 ng/ml), the median prostatectomy Gleason score was 7 (Q1=6, Q3=8), ranging from GS 6 to GS 10. For this study, the median time interval between MRI scan and prostatectomy was 40 days (Q1=14 days, Q3=83.8 days), ranging from 2 to 201 days.

The distribution of Gleason scores across patients, the ROI numbers, and lesion-based ROI sizes used in the analyses are summarized in Table 4.2. In the peripheral zone 241 cancer ROIs were drawn for 62 patients, while in the transition zone 101 cancer ROIs were drawn for 22 patients. Nineteen cases had both peripheral zone and transition zone lesions. The median size of these averaged, lesion-based ROIs in the peripheral zone was 0.30cc (Q1=0.16cc, Q3=0.52cc), ranging from 0.05cc to 8.28cc, while in the transition zone the median lesion-based ROI size was 0.20cc (Q1=0.15cc, Q2=0.60cc), ranging from 0.06cc to 2.05cc.

Table 4.2: Patient, region of interest (ROI) counts, and lesion based ROI sizes for healthy and cancerous tissues.

Prostate Region	Tissue Type	Number of Patients	Number of ROIs	Median (Q1, Q3) Lesion-based ROI size (cc)
Peripheral Zone	Benign	67	218	0.31 (0.16, 0.59)
	3+3	22	54	0.26 (0.20, 0.34)
	3+4	25	78	0.38 (0.14, 0.59)
	4+3	18	42	0.26 (0.15, 0.57)
	4+4	10	21	0.17 (0.13, 0.26)
	4+5	4	19	1.86 (0.36, 4.36)
	5+3	2	8	0.93 (0.56, 1.30)
	5+4	3	9	0.32 (0.30, 0.57)
	5+5	2	10	4.29 (2.30, 4.29)
Transition Zone	Benign	42	126	0.28 (0.12, 0.59)
	3+3	13	32	0.27 (0.16, 0.36)
	3+4	11	37	0.18 (0.11, 0.30)
	4+3	9	25	0.18 (0.15, 0.64)
	4+4	2	5	0.65 (0.37, 0.93)
	3+5	1	2	0.30 (0.30, 0.30)

Benign regions include cystic atrophy and normal peripheral zone tissues.
Not normally distributed data reported as median (first quartile (Q1), third quartile (Q3)).

An example of mpMR images obtained as part of the study and corresponding histopathological slides are illustrated in Figure 4.1 for a peripheral zone cancer and in Figure 4.2 showing a transition zone cancer.

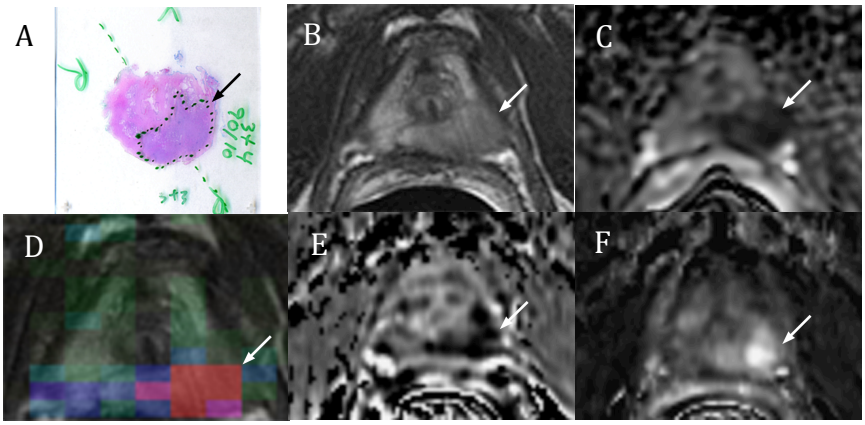

Figure 4.1: A 59 year-old male with serum PSA of 4.8 ng/ml and GS3+4 prostate cancer who underwent radical prostatectomy. a) H&E stained histology specimen, b) coil-corrected T2-weighted FSE image, c) ADC map, d) MRSI choline metabolite map, e) washout slope, f) maximal enhancement slope. The arrows designate cancerous lesions.

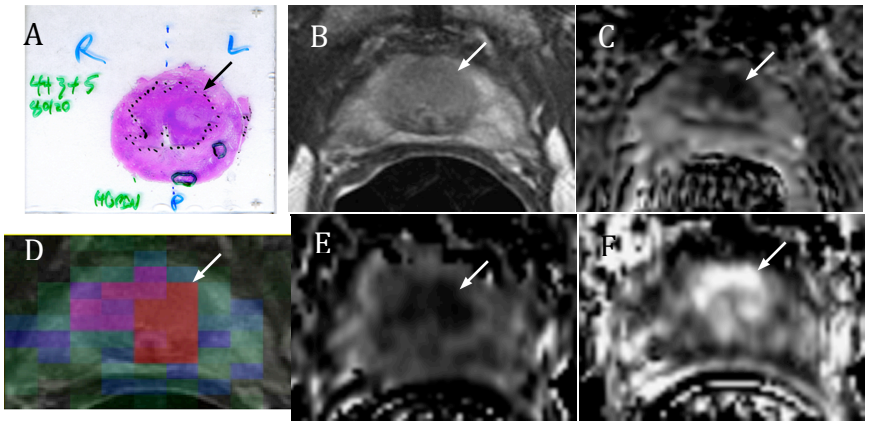

Figure 4.2: A 56 year-old male with serum PSA of 12.5 ng/ml and GS4+3+5 prostate cancer who underwent radical prostatectomy. a) H&E stained histology specimen, b) coil-corrected T2-weighted FSE image, c) ADC map, d) MRSI choline metabolite map, e) washout slope, f) maximal enhancement slope. The arrows designate cancerous lesions.

Figure 4.3 depicts the magnetic resonance spectra within the peripheral zone for the patient in Figure 4.1 demonstrating the quality of the acquired MRSI data. The citrate peaks are prominent within the right lobe of the prostate indicating benign nature of the tissues, the choline peaks are evident within the left lobe of the prostate indicating malignancy.

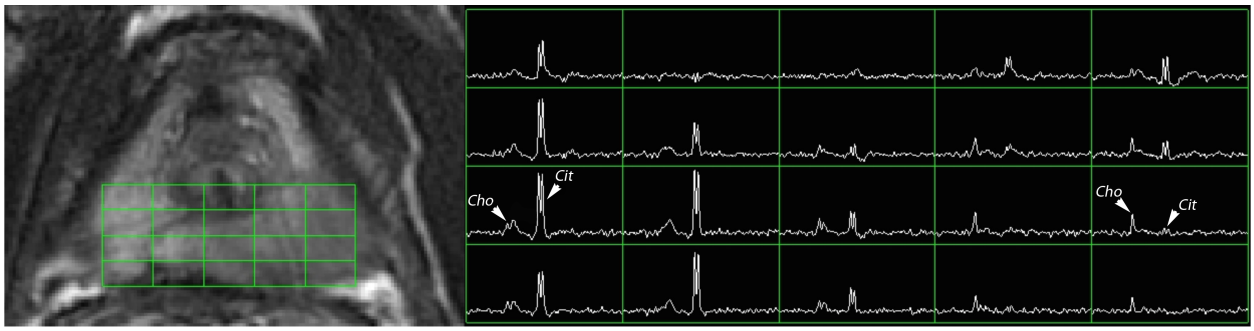

Figure 4.3: Magnetic resonance spectra for a 59-year old male with serum PSA of 4.8 ng/ml and GS3+4 prostate cancer who underwent radical prostatectomy (histopathology and mpMR images are displayed in Figure 4.1). Cit indicates the citrate peaks and Cho designates the choline peak.

Figure 4.4 summarizes the distribution of values observed for the imaging parameters in benign tissues, as well as in GS3+3, in GS3+4, and in those GS4+3 and higher cancer tissues (≥GS4+3) in the peripheral zone. To determine the discriminatory value of each measured imaging parameter independent of each other, values obtained for each tissue and tumor type were compared. Within the peripheral zone, statistically significant differences were noted between benign and GS3+3, benign and GS3+4, as well as benign and ≥GS4+3 for all imaging parameters. Additionally, statistically significant differences were noted between GS3+3 and ≥GS4+3 on ADC ($p=0.0065$), washout slope ($p=0.019$), Cho/Cit ratio ($p=0.04$), and Cho/Cre ($p=0.0001$), however, maximal enhancement slope did not reach statistical significance ($p=0.053$). Other results that did not reach statistical significance for group differences were GS3+3 compared to GS3+4 tissues on maximal enhancement slope ($p=0.0621$) and Cho/Cre ($p=0.07$). Cho/Cre was the only parameter for which statistically significant differences ($p=0.028$) were observed between GS3+4 and ≥GS4+3 cancers.

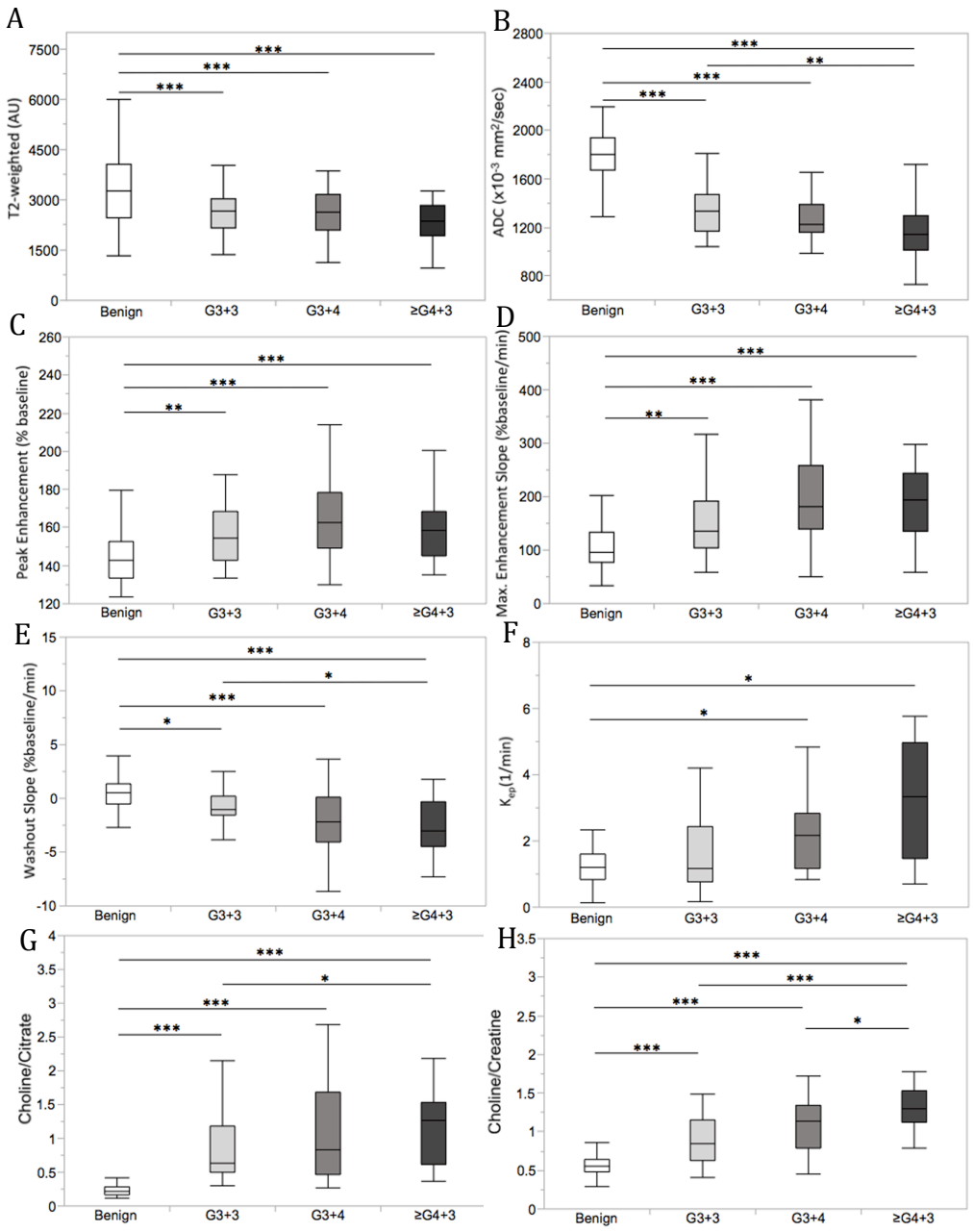

Figure 4.4: Box-plots comparing MR measures in normal peripheral zone tissues and GS3+3, GS3+4, and ≥GS4+3 peripheral zone cancers. A) T2-weighted intensity, B) ADC, C) Peak Enhancement, D) Maximal Enhancement Slope, E) Washout Slope F) K_{ep}, G) Choline/Citrate, H) Choline/Creatine. Horizontal lines within the box plots represent the median values. Whiskers are drawn to the furthest points within 1.5x interquartile range, where interquartile range is the difference between the 1st and the 3rd quartiles.
*** <0.0001, ** <0.001, * <0.05

Figure 4.5 summarizes the distribution of values observed for the imaging parameters in benign tissues, as well as GS3+3, GS3+4, and ≥GS4+3 cancers in the transition zone.

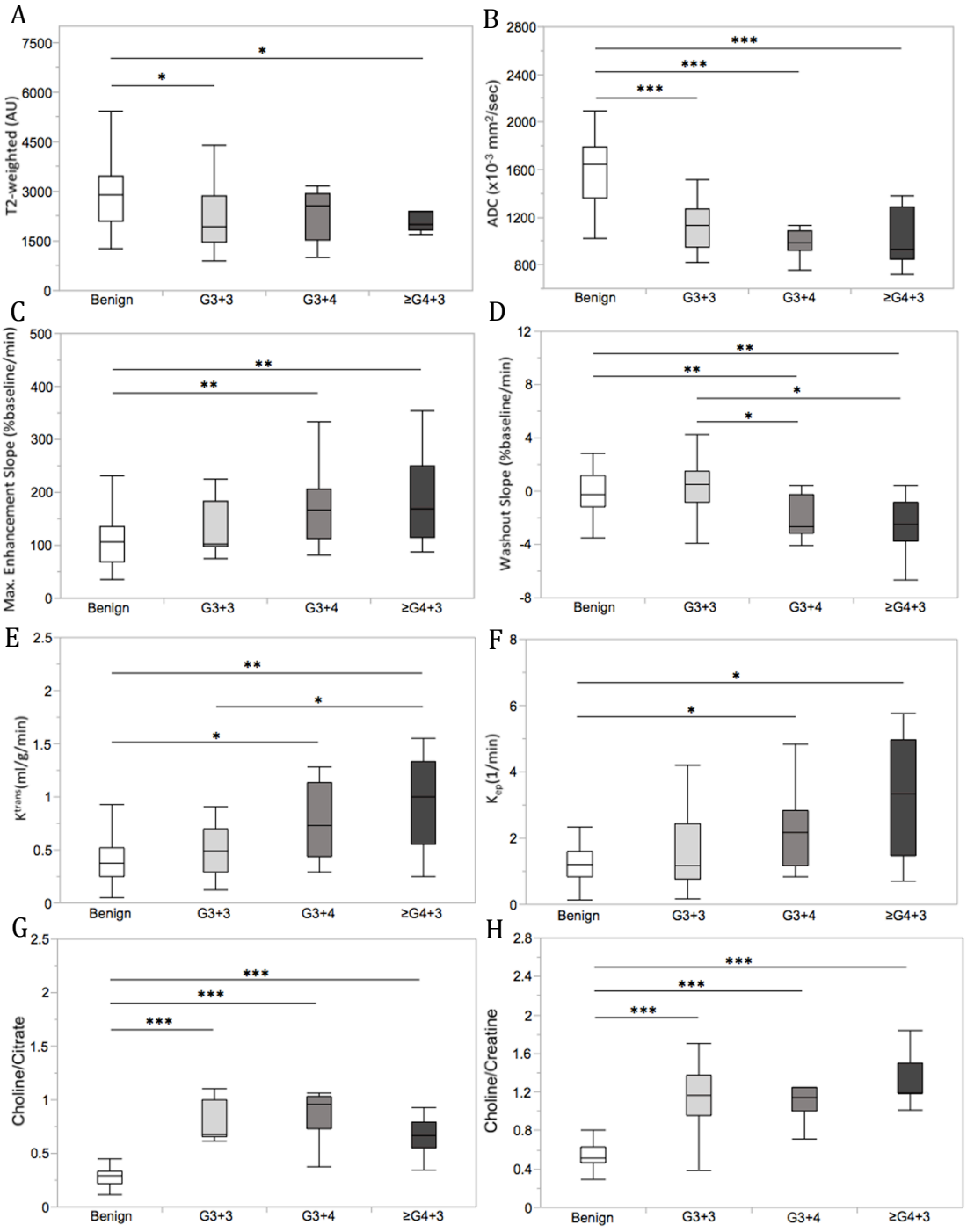

Figure 4.5: Box-plots comparing MR measures in normal transition zone tissues and GS3+3, GS3+4, and ≥GS4+3 transition zone cancers. A) T2-weighted intensity, B) ADC, C) Maximal Enhancement Slope, D) Washout Slope, E) K^{trans}, F) K_{ep}, G) Choline/Citrate, H) Choline/Creatine. Horizontal lines within the box plots represent the median values. Whiskers are drawn to the furthest points within 1.5x interquartile range, where interquartile range is the difference between the 1st and the 3rd quartiles.
*** <0.0001, ** <0.001, * <0.05

Within the transition zone, statistically significant differences between benign and GS3+3, benign and GS3+4, as well as benign and ≥GS4+3 cancers were noted on the majority of modalities as depicted in Figure 4.5. Additionally, statistically significant differences were observed between GS3+3 and ≥GS4+3 on washout slope (p=0.0451) and Cho/Cit ratio (p=0.0447). No statistically significant differences were noted between GS3+3 and GS3+4 cancers or between GS3+4 and ≥GS4+3 cancers.

The results for the logistic regression analyses to discriminate between tissue types including the AUC, the specificity, and the sensitivity, are given in Tables 4.3 and 4.4. The results for the peripheral zone are summarized in Table 4.3, while Table 4.4 contains the results for the transition zone.

Table 4.3: Peripheral zone – results of the logistic regression analysis with the area under the curve (AUC), sensitivity and specificity values demonstrating the capabilities of individual metric and combinations of parameters to discriminate tissues of interest.

Parameter	Benign/All Cancers			G3+3/≥G3+4			≤G3+4/≥G4+3		
	AUC	Sensitivity	Specificity	AUC	Sensitivity	Specificity	AUC	Sensitivity	Specificity
T2-weighted	0.73	86.4	55.2	0.56	60.9	59.1	0.62	66.7	61.5
ADC	0.90	94.9	77.6	0.68	73.9	63.6	0.68	57.6	79.5
Peak Enhancement	0.74	61.0	77.6	0.57	56.5	63.6	0.52	75.8	38.5
Max Enhancement Slope	0.82	81.4	70.7	0.66	45.7	86.4	0.56	54.6	66.7
Washout Slope	0.77	66.1	79.3	0.65	54.4	86.4	0.63	63.6	66.7
K^{trans}	0.75	59.3	86.2	0.60	91.3	31.8	0.54	42.4	74.4
K_{ep}	0.73	50.9	89.7	0.57	65.2	54.6	0.54	33.3	87.2
v_L	0.70	54.2	87.9	0.51	47.8	68.2	0.50	42.4	69.2
Choline/Citrate (CC)	0.98	100	89.7	0.72	73.9	72.7	0.61	72.7	59.0
[Choline+Creatine]/Citrate	0.96	88.1	91.4	0.65	56.5	77.3	0.58	54.6	71.8
Choline/Creatine (Cho/Cre)	0.94	94.8	84.8	0.79	77.3	82.6	0.73	64.1	87.9
Combined (ADC, K_{ep}, CC)	1.0	100	100						
Combined (ADC, Max Enhancement Slope, Cho/Cre)				0.82	86.4	73.9			
Combined (ADC, Washout, Cho/Cre, CC)							0.80	76.9	69.7

Table 4.4: Transition zone – results of the logistic regression analysis with the area under the curve (AUC), sensitivity and specificity values demonstrating the capabilities of individual metric and combinations of parameters to discriminate tissues of interest.

Parameter	Benign/All Cancers			G3+3/≥G3+4			≤G3+4/≥G4+3		
	AUC	Sensitivity	Specificity	AUC	Sensitivity	Specificity	AUC	Sensitivity	Specificity
T2-weighted	0.76	85.0	58.3	0.56	66.7	61.5	0.53	88.9	38.9
ADC	0.94	90.0	88.9	0.65	73.3	61.5	0.53	55.6	77.8
Peak Enhancement	0.61	65.0	58.3	0.53	80.0	38.5	0.53	77.8	38.9
Max Enhancement Slope	0.72	95.0	47.2	0.66	80.0	61.5	0.62	33.3	94.4
Washout Slope	0.68	40.0	97.2	0.81	73.3	84.6	0.68	77.8	61.1
K^{trans}	0.71	55.0	91.7	0.70	60.0	84.6	0.69	77.8	61.1
K_{ep}	0.36	100	28.0	0.68	66.7	76.9	0.70	55.6	88.9
v_L	0.55	75.0	47.2	0.68	60.0	84.6	0.65	66.7	72.2
Choline/Citrate (CC)	0.95	95.0	94.4	0.49	33.3	92.3	0.70	88.9	55.6
[Choline+Creatine]/Citrate	0.89	90.0	83.3	0.49	26.7	92.3	0.74	100	55.6
Choline/Creatine (Cho/Cre)	0.92	83.3	100	0.70	69.2	86.7	0.72	50.0	100
Combined (T2w, ADC, CC)	1.0	100	100						
Combined (Washout Slope)				0.81	73.3	84.6			
Combined (Kep, Cho/Cre)							0.83	83.3	77.8

The results of the repeated k-fold cross-validation of the combined models are summarized in Table 4.5, with the training and the validation ROC AUC, as well as the confidence intervals reported.

Table 4.5: The area under the curve (AUC) and the confidence intervals (CI) reported for the training and the validation models using the repeated 4-fold cross validation.

Region	Model	Benign/All Cancers			G3+3/≥G3+4			≤G3+4/≥G4+3		
		AUC	95% CI		AUC	95% CI		AUC	95% CI	
Peripheral Zone	Training	1.0	1.0	1.0	0.82 (± 0.04)	0.82	0.83	0.81 (± 0.03)	0.80	0.82
	Validation	0.99(± 0.02)	0.99	1.0	0.80 (± 0.11)	0.78	0.82	0.78 (± 0.10)	0.76	0.80
Transition Zone	Training	1.0	1.0	1.0	0.80 (± 0.06)	0.79	0.82	0.83 (± 0.05)	0.82	0.83
	Validation	0.97 (± 0.05)	0.96	0.98	0.85 (± 0.15)	0.82	0.87	0.77 (± 0.16)	0.74	0.81

4.5 Discussion

Using one or a combination of several quantitative parameters derived from MR imaging to separate benign tissues from PCa and discriminate among different levels of PCa aggressiveness is a promising step toward improving prostate cancer characterization. A few studies have reported on the associations of individual imaging parameters and prostate Gleason grading.[90,127,148,215-218] For instance, Wang *et al*. found statistically significant associations between higher Gleason scores and lower tumor to muscle signal intensity ratio on T2-weighted images.[215] Statistically significant negative correlations were reported between diffusion ADC values and prostate cancer Gleason scores.[90,216-218] Studies such as ACRIN have raised questions regarding suitability of spectroscopy for cancer detection, particularly for smaller ≤GS3+3 lesions[62]; however, despite this limitation, MRSI has been shown an excellent technique for cancer characterization.[127,219,225] The combinations of different metabolite ratios i.e. choline plus creatine to citrate, choline to citrate, or choline/creatine obtained from MRSI shows promise for discrimination of low-grade and higher-grade prostate tumors.[127,219,225] Several studies have also reported promising associations between DCE MRI derived parameters and Gleason grades.[148,217,220] Chen *et al*. observed a statistically significant association between the washout gradient and Gleason scores.[220] Peng *et al*. noted moderate correlations of K^{trans} with Gleason scores[217], while Vos *et al*. found that a combination of DCE MRI parameters (mean and 75th percentile values of enhancement slope, mean washout, and 75th percentile values of K^{trans}) may aid in separating low-risk from more aggressive cancers.[148] In the last few years, several groups have published predictive models obtained by considering sets of predictors made up of multiple imaging parameters.[217,226,227] Unfortunately, some studies are limited by the use of biopsy-based histopathology,[226] which is associated with sampling errors.[32] Others, while using prostatectomy

histopathology for imaging validation, performed an abbreviated imaging protocol, resulting in incomplete multiparametric models.[217] Additionally, most studies exclude lesions smaller than 0.5cc.[227,228] Such size restrictions may limit applicability of the findings to the growing active surveillance patient population.

This study examined all imaging modalities currently available in clinical scanning and used post-radical prostatectomy whole mount histopathology as the reference standard. To identify the purest cancer signatures, we only looked at regions with greater than 50% cancer composition on pathology and homogeneous imaging appearance. Unlike other studies, our cancer size restrictions were minimal. We included all regions of interest greater than 0.05cc, with resultant median cancer lesion-based ROI size of 0.3cc in the peripheral zone and 0.2cc in the transition zone, with lesion sizes ranging from 0.05cc to 8.28cc and 0.06cc to 2.05cc for the two regions respectively.

Within the peripheral zone, while statistically significant differences between benign and malignant tissues were observed for all imaging parameters, logistic regression yielded the highest AUC values for ADC, K_{ep}, and Cho/Cit. A combination of these parameters resulted in a complete separation of benign and malignant tissues with an AUC of 1.0. The stability of the model was demonstrated using repeated four-fold cross-validation, which yielded an AUC of 0.99 (95% confidence interval, 0.99 - 1). Similar results were seen in the transition zone by combining ADC, Cho/Cit ratio, and T2-weighted image intensity, which yielded an AUC of 1.0 with a validation AUC of 0.97 (95% confidence interval, 0.96 - 0.98), indicating the excellent performance of the model. Interestingly, Cho/Cit was the single best performing parameter for distinguishing benign and malignant tissues for both the peripheral zone and the transition zone, demonstrating AUC values of 0.98 and 0.95 respectively, higher than those observed for ADC.

These results are similar or better than those reported in literature: with AUC values for combined models for discrimination of normal and cancerous regions ranging from 0.82 to 0.96 in the peripheral zone[227,229,230] and 0.76 to 0.92 in the transition zone.[150,231,232]

Next, the ability of mpMRI parameters to distinguish GS3+3 from ≥GS3+4 prostatic cancers was investigated. Studies have noted the importance of identifying a Gleason 4 component in order to better monitor disease progression and minimize risk of prostate cancer specific mortality.[233] Within the peripheral zone a combination of ADC, maximal enhancement slope and Cho/Cre ratio yielded an AUC of 0.82 with a good sensitivity of 86.4 and a lower specificity of 73.9. This suggests that some of the GS3+3 cancers tend to look more aggressive on imaging. This is not surprising since separating GS3+3 and GS3+4 cancers with minimal Gleason 4 disease is a considerable challenge, and these aggressive appearing G3+3 tumors could be genetically[234] and metabolically[235] more aggressive leading to poorer outcomes. In the transition zone, washout slope was the best performing parameter, yielding an AUC of 0.81, which was higher than any AUCs obtained for multiple predictor models fitted. This result highlights the importance of using a comprehensive mpMR imaging, incorporating both DCE and MRSI when assessing the aggressiveness of prostate cancer at diagnosis in a contemporary early stage population of patients.

Finally, in order to assess our ability to distinguish low-risk from high-risk disease, we examined the performance of mpMRI parameters at separating grouped GS3+3 and GS3+4 cancers from ≥GS4+3 prostate lesions. At many institutions patients can continue with active surveillance in the presence of GS3+4 disease; however, diagnosis of GS4+3 cancers on biopsy typically triggers treatment with curative intent, which makes our ability to separate the two groups of clinical importance. Within the peripheral zone, a combination of ADC, K_{ep}, Cho/Cre,

and Cho/Cit yielded an AUC of 0.80 with a sensitivity of 76.9 and a specificity of 69.7, likely due to the considerable challenges associated with separating GS3+4 and GS4+3 lesions on imaging. In the transition zone, combined K_{ep} and Cho/Cre yielded an AUC of 0.83 for discriminating between low-risk (GS3+3/GS3+4) and high-risk (≥GS4+3) disease, with reasonable sensitivity of 83.3 and specificity of 77.8. It is important to note that all the models described above had very narrow confidence intervals and excellent corresponding validation AUC values, indicating the robustness of the final models.

Other studies have looked at separating low and high-risk prostate cancers. In a 2015 study, Vos *et al.* reported a combined AUC of 0.85 for separating low-grade PCa (defined as GG ≤3) from high-grade lesions (defined as GG ≥4) in the peripheral zone and an AUC of 0.92 for the transition zone.[227] Peng *et al.* also looked at using combined models to distinguish low-grade disease (GS3+3) and high-grade lesions (GS 7, 8, 9) and reported an AUC of 0.77 for their combined model within the peripheral zone.[217] These and our models show promise in using an mpMRI technique for evaluation of cancer. Our models go a step further in showing the ability of mpMRI to discriminate low-risk from high-risk prostate cancers even for smaller lesions, which is critical in the setting of early stage disease typically found in active surveillance patients.

The role of multiparametric MR imaging in prostate cancer management is continually evolving. T2-weighted imaging and DW imaging are universally accepted for PCa diagnosis. Version 1 of the Prostate Imaging – Reporting and Data System (PI-RADS) published in 2012 and designed to standardize acquisition, interpretation and reporting of mpMRI scans was based solely on T2-weighted imaging and DWI.[236] The current PI-RADS version 2 entirely omits MRSI and advises the use of qualitative DCE MRI only in cases of borderline findings on DWI

and T2w imaging in the peripheral zone and omits the use of DCE MRI for detection of lesions in the transition zone. Our study showed the importance of both MRSI measurements and DCE MRI-derived quantitative parameters for building better models for discriminating between prostatic cancerous and benign tissues, and more importantly for distinguishing between malignant prostatic tissues of various grades. These findings are important for improving therapeutic selection for individual patients, and for designing improved clinical trials of new therapeutic approaches.

Our study has several limitations. First, the regions of interest were manually drawn on MR images based on the histopathology; this approach could have potentially introduced bias toward outlining MR visible features as opposed to histologically evident cancers. Second, MR sequences were manually aligned to each other based upon visual assessment; however, it is possible that some regions were not perfectly transferred from one sequence to another. Third, this study only included cancer regions with greater than 50% cancer composition and homogeneous imaging appearance. This was done to identify the purest imaging signatures associated with PCa of different Gleason grades and to establish mpMRI capabilities in detecting these lesions. However, this selection process resulted in smaller ROIs than the histopathological lesions and does introduce bias to our results. Fourth, prostate tissues are extremely heterogeneous; in the analysis above normal tissues and cystic atrophy were presented as benign tissues. This is an oversimplification of the complex nature of the benign prostatic tissues, which requires further exploration. High-b DW imaging was incorporated into the imaging protocol part way through the study. Due to low numbers (only 35/78 patients had high-b DW imaging performed), high-b DWI, which has proven to be very useful in contemporary studies,[237,238] was not included in the models. Finally, truth in this study was based solely on pathologic grade at

surgery, mpMRI may be able to identify those GS3+3 tumors that could result in poor clinical outcomes.

In conclusion, this study demonstrated excellent separation of benign tissues and PCa, as well as cancers across Gleason Scores in the peripheral zone and in the transition zone using mpMRI, even in very small lesions. Quantitative measures of DWI, MRSI, and DCE MRI aided the discrimination between Gleason Grade groups of cancers, underlining the value of a comprehensive mpMRI protocol for evaluation of prostate cancer presence and aggressiveness.

CHAPTER 5

Semi-Automatic Technique for Segmentation and Evaluation of Prostate Cancer Regions as Outlined On Whole-Mount Histopathology

5.1 Abstract

The purpose of this study was to develop a technique for 1) segmentation of prostate cancer regions outlined on whole-mount histopathology slides and 2) accurate estimation of the segmented region areas. Image processing and color segmentation techniques in Matlab were used to develop the procedure for cancer region segmentation. User initialized gradient vector flow (GVF) active contouring was then applied to the extracted cancerous regions to obtain an accurate outline of each region. Region areas were computed first in pixels and then converted to cm^2. The areas for 1193 cancer regions outlined on histopathology slides for 78 patients were successfully computed using these segmentation and contouring techniques. A small study was designed to test repeatability of the GVF snake contouring. Fifteen lesions differing in size and degrees of concavities were randomly chosen. For each region, the process of GVF snake initialization, lesion contouring, and region area computation was repeated 10 times and the coefficient of variation was calculated. The coefficients of variation were small ranging from 0.0018 to 0.0166, indicating the overall robustness of the technique.

5.2 Introduction

Histopathology is widely considered a reference standard for PCa diagnosis and lesion characterization. Pathology derived Gleason grading has been linked to critical clinical outcomes such as disease staging, progression to metastatic disease, and survival.[11] Lesion size and Gleason grading are the most accurate indicators of disease aggressiveness. Nevertheless,

accurate quantitative assessment of lesion volumes and grading in the radical prostatectomy specimen is difficult to come by. In a clinical setting, tumor volumes are often approximated, with size and Gleason grading details reported only for the largest lesions. Whole-mount slicing of the prostate, digitization of the histopathology slides, and detailed histopathological review provide a unique opportunity to get a better picture regarding the number of lesions, lesion volumes, and their aggressiveness in a surgical population. The goal of this project was to develop a semi-automatic way of accurately segmenting cancerous regions and determining the sizes of cancerous regions as outlined on the whole-mount histopathology slides by a prostate pathologist.

5.3 Theory

5.3.1 Traditional snakes

Active contours or snakes are commonly used in computer vision to identify the boundaries of an object. Snakes have first been introduced in 1987 in a seminal paper by Kass *et al.*[239] and defined as energy-minimizing splines guided by external constraint forces and influenced by image forces that pull them toward features such as lines and edges. The image forces tend to push the snake toward the prominent image features (such as lines or edges), while the external constraint forces act to position the snake near the local minimum of choice (such as specified by a user).

The snake is a contour represented parametrically as c(s)=(x(s), y(s)) where x(s) and y(s) are coordinates along the contour and s is taken to vary between 0 and 1 (Figure 5.1).

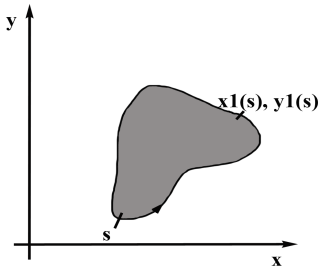

Figure 5.1: Parametric curve.
The contour or the snake is defined in the (x, y) plane of an image as a parametric curve c(s)=(x(s), y(s)). The snake is influenced by the internal, external and the image forces as described in Eq. 5.1.

The snake moves through the spatial domain of an image to minimize its energy function. The energy of the snake (E_{snake}) can be written as a weighted sum of forces acting upon it.[239]

$$E_{snake} = \int_0^1 E_{internal}(c(s)) + E_{image}(c(s)) + E_{constraint}(c(s))ds \qquad [5.1]$$

The integral notation implies an open-ended snake; however, closed ended snakes, created by joining the first and the last elements, are often used in practice.

$E_{internal}$ is the internal energy of the spline due to bending and imposes a smoothness constraint; E_{image} represents the image forces that push the snake toward the image features (i.e. edges, light or dark regions, terminations and etc.), $E_{constraint}$ represents the external constraints responsible for placing the snake near the local minimum (user input or automatic initialization).

5.3.1.1 Internal Energy

The internal spline energy ($E_{internal}$) can be written out in terms of elastic and bending energies, which can be viewed as tension and stiffness respectively (Eq. 5.2).

$$E_{internal} = \frac{1}{2}(\alpha(s)|c'(s)|^2 + \beta(s)|c''(s)|^2) \qquad [5.2]$$

The first order derivative $c'(s)$ makes the spline act like a membrane, while the second order derivative $c''(s)$ makes it act like a thin plate. In this manner, by adjusting the weights $\alpha(s)$ and $\beta(s)$ the elasticity and the rigidity terms of the snake are controlled. For instance, setting $\beta(s) = 0$ in one part of the model allows the snake to become second-order discontinuous and develop a corner. When no other constraints are applied, a snake collapses to a point; however, if the ends of the snake are fixed in space, it forms a straight line with evenly spaced elements.[240]

5.3.1.2 Image Energy

The image energy or the potential energy generated by processing an image I(x,y) produces a force that can be used to drive snakes towards features of interest.

The image forces act to attract the snake to the image features such as lines, edges, or terminations. As such, the image energy (E_{image}) can be written out as the sum of these individual energy components (Eq. 5.3).[240]

$$E_{image} = w_{line}E_{line} + w_{edge}E_{edge} + w_{termination}E_{termination} \quad [5.3]$$

E_{line} is defined by the image intensity (Eq. 5.4).

$$E_{line} = I(x, y) \quad [5.4]$$

Depending on the sign of w_{line} the snake will either be attracted to the lightest or the darkest nearby lines of the image and will try to align itself with either the lightest or the darkest nearby contour (Figure 5.2a).

By defining the edge energy E_{edge} as the gradient-based potential energy (Eq. 5.5), the snake is attracted to contours with large image gradients and thus it stops when it hits a hard edge (Figure 5.2b).

$$E_{edge} = -|\nabla I(x, y)|^2 \quad [5.5]$$

Finally, the snake can be attracted to corners and terminations using the energy term based on the line curvature (Figure 5.2c). This is usually done for a slightly smoothed image.

Assuming our image I(x,y) was smoothed to create image J(x,y) and the gradient direction is given by $\theta = \tan^{-1}(J_y/J_x)$, then the unit vectors along and perpendicular the image gradient are[240]

$$\mathbf{n}_{\parallel} = \begin{pmatrix} \cos\theta \\ \sin\theta \end{pmatrix} \qquad \mathbf{n}_{\perp} = \begin{pmatrix} -\sin\theta \\ \cos\theta \end{pmatrix}$$

The curvature of a contour can be written as

$$E_{termination} = \int_0^1 \frac{\partial\theta}{\partial \mathbf{n}_{\perp}} ds = \int_0^1 \frac{\partial^2 J/\partial \mathbf{n}_{\perp}^2}{\partial J/\partial \mathbf{n}_{\parallel}} ds \quad [5.6]$$

This can be ultimately written as

$$E_{termination} = \int_0^1 \frac{J_{yy}J_x^2 + J_{xx}J_y^2 - 2J_{xy}J_xJ_y}{(J_x^2 + J_y^2)^{3/2}} ds \quad [5.7]$$

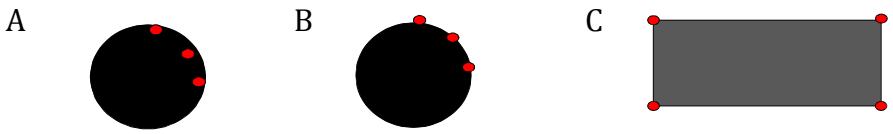

Figure 5.2: Examples of line, edge, and termination scenarios for snake contouring. a) With w_{line} set at a positive value, minimizing E_{line} puts the snake contour in a dark region ($w_{line}<0$ would ensure attraction to light regions) b) moving towards large image gradients, the snake stops when it hits a hard edge, c) the snake locates the corners by identifying points of high curvature within the region.

5.3.1.3 Constraint Energy

Snakes rely on "high-level" processes such as user input or automatic initialization to place them somewhere near a desired solution. An initialization protocol may locate the features of interest in an image and then a snake can be used for further refinement. Alternatively, a user may need to push the snake towards an image feature, while the energy minimization will take care of the rest, fitting the active contour to the data. In other words, both automatic and manual supervision can be used to control attraction and repulsion forces that drive snakes to and from specific features.

5.3.1.4 Euler Formulation

Typically, E_{image} and $E_{constraint}$ can be combined into external energy E_{ext}.

$E_{ext} = E_{image} + E_{constraint}$

The energy equation for the snake becomes

$$E = \int_0^1 \frac{1}{2}(\alpha(s)|c'(s)|^2 + \beta(s)|c''(s)|^2) + E_{ext}(c(s))ds \qquad [5.8]$$

When $\alpha(s)=\alpha$ and $\beta(s)=\beta$ are constants, minimizing the energy equation (Eq. 5.8) gives rise to the following Euler equation (Eq. 5.9).

$$\alpha c''(s) - \beta c''''(s) - \nabla E_{ext} = 0 \qquad [5.9]$$

Since a snake typically deforms over a series of iterations, each element x along the contour technically can be written as x(s,t) and not just x(s), with space s (curve) and time t (iteration) serving as parameters. Eq. 5.9 can be rewritten as

$$\alpha c''(s,t) - \beta c''''(s,t) - \nabla E_{ext} = 0 \qquad [5.10]$$

There are several strategies (briefly outlined below) that can be utilized to achieve a solution to this problem and ensure convergence of the active contour.[241]

5.3.1.5 Energy Minimization Strategies

Energy minimization is at the core of the active contouring. There are several approaches to solving the energy minimization problem; these can mostly be split into continuous and discrete categories.[242] The continuous methods are Newton-Raphson, as well as gradient based techniques (gradient descent, conjugate gradient, and proximal gradient), while discrete approaches include graph cuts, constrained optimization methods (linear programming), message passing algorithms (belief propagation), as well as simulated annealing[243] and iterative conditional modes, which are both based on Markov-Random-Fields.[242] It is not the intention of this work to provide mathematical formulations for these techniques; however, it might be useful to briefly look at the advantages and drawbacks associated with these methods. For instance, Newton-Raphson method typically requires the fewest number of steps to reach the minimum but is the most computationally expensive approach per step since the evaluation of both the first and the second derivatives is required at each iteration. Gradient descent approaches, on the other hand, are typically faster at each iteration (do not require calculation of the second derivative) but generally involve greater number of iterations to reach the minimum and are slower to converge. Unlike gradient descent techniques that are prone to local minima and require guidance from the user to ensure optimal solution, discrete optimization approaches tend to

obtain global minima of the energy function. Largely more receptive to automatic initialization, discrete techniques come with their own set of challenges such as limited applicability to non-submodular energy functions (graph cuts),[244] lack of guaranteed convergence (belief propagation),[245] stalling and lack of efficiency (linear programming),[242] slow convergence and necessity for additional steps/methods for verification of optimal solution (simulated annealing),[243,245] or sensitivity to initial estimate (iterative conditional modes).[242]

5.3.2 Gradient Vector Flow

Since their introduction, snakes have been widely used for edge detection[246], segmentation[247,248], motion tracking[249,250], and etc. The two main problems with the conventional snake models as described above are: 1) their performance tends to depend significantly on initialization (poor convergence for snakes initialized far from the minimum), 2) poor performance in scenarios involving boundary concavities.[251] Attempts have been made to address some of these shortcomings by introducing additional external forces such as the solenoidal fields[252] proposed by Prince *et al.*, as well as pressure forces[253] or distance forces[254] proposed by Cohen *et al.* as part of the balloon models. While these approaches performed better than the traditional active contour models, a comprehensive solution was not introduced until 1997 when Xu *et al.* proposed a new class of external forces called gradient vector flow (GVF) fields.[6,251,255]

The advantages of a GVF snake are its insensitivity to initialization (initialization can be made inside or outside of the object boundary) and its ability to move into concave boundary regions. The GVF approach begins by defining an edge map. An edge map is derived from the image and has the following properties: 1) the gradient of an edge map has vectors pointing toward the edges, 2) these vectors have large magnitudes only in the immediate vicinity of the

edges, and 3) in homogeneous regions where the image values are nearly constant, the edge map is nearly zero.[251] While the first property allows a snake initialized close to the edge to converge; the second and the third properties act to decrease the capture range of the snake, which is not desirable. To address this, a computational diffusion process is used to extend the gradient map farther from the edges into the homogeneous regions, which: 1) results in increased capture range of the external edge map force field, making the snake evolve toward the desired boundary; and 2) creates vectors that point into the boundary concavities, permitting the contour to reach these irregular boundaries[6].

Figure 5.3 demonstrates the capture range differences between the traditional potential force fields (Figure 5.3a,b - top panel) and the GVF fields (Figure 5.3c,d - bottom panel). The streamlines shown on the right hand side display the movement of free particles under the influence of the external forces. Straight away, it can be clearly seen that the range of GVF forces (Figure 5.3d) is significantly larger than that seen for the traditional potential forces (Figure 5.3b). Furthermore, GVF provides downward forces that allow for the contouring of the concavity in the U shape (Figure 5.3c) while the potential forces only provide sideways forces making it impossible for the snake to enter the concave region (Figure 5.3a).

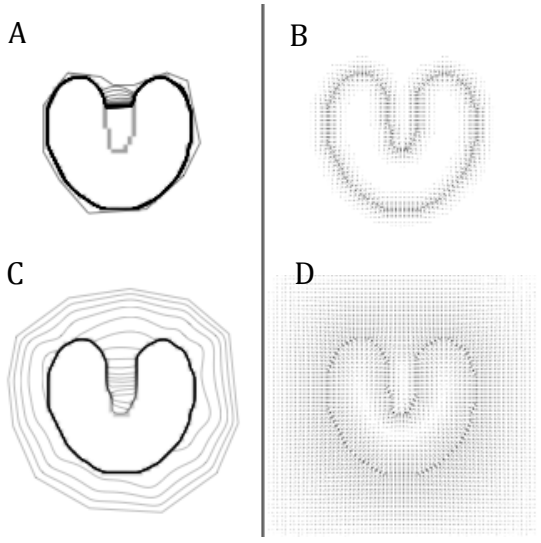

Figure 5.3: Left panel demonstrates convergence of the snake using a) traditional potential forces and c) GVF external forces. The images show that compared to the traditional potential forces depicted in (b), the GVF forces (d) have a larger capturing range and are capable of driving the active contours inside the concavities (c) that are unreachable with traditional potential forces (a).

The figure is adapted from a paper by Chenyang Xu and Jerry L. Prince. Snakes, Shapes, and Gradient Vector Flow. IEEE Transactions on Image Processing. 1998;7(3):359-369.[6]

The gradient of the edge map f(x,y) is computed from the original image I(x,y) using the following equations:

For binary images, Eq. 5.11 and 5.12 are used.

$$f^1(x,y) = -I(x,y) \quad [5.11]$$

$$f^2(x,y) = -G_\sigma(x,y) * I(x,y) \quad [5.12]$$

where $G_\sigma(x,y)$ is a 2D Gaussian function with standard deviation σ.

For grey scale images, Eq. 5.13 and 5.14 are used in edge map calculations instead.

$$f^3(x,y) = -|\nabla I(x,y)|^2 \quad [5.13]$$

$$f^4(x,y) = -|\nabla[G_\sigma(x,y) * I(x,y)]|^2 \quad [5.14]$$

The gradient vector flow field is defined as vector field **g**(x,y) = (u(x,y), v(x,y)) that minimizes the energy function (Eq. 5.15), where f(x,y) is the edge map and ∇f is the gradient of the edge map, μ controls the smoothness of the GVF field and is set according to the noise level in the original image (larger μ values are used for noisier images).

$$E = \iint \mu(u_x^2 + v_y^2 + u_x^2 + v_y^2) + |\nabla f|^2 |\mathbf{g} - \nabla f|^2 \, dxdy \quad [5.15]$$

This minimization is achieved by solving two resultant decoupled linear partial differential equations (Eq. 5.16 and 5.17).

$$\mu\nabla^2 u - (u - f_x)\left(f_x^2 + f_y^2\right) = 0 \quad [5.16]$$

$$\mu\nabla^2 v - (v - f_x)\left(f_x^2 + f_y^2\right) = 0 \quad [5.17]$$

∇^2 is the Laplacian operator $\nabla^2 = \frac{\partial^2}{\partial x^2} + \frac{\partial^2}{\partial y^2}$

When u and v are treated as functions of time t, rewriting these equations for $t \rightarrow \infty$ results in a pair of generalized diffusion equations

$$u_t(x,y,t) = \mu\nabla^2 u(x,y,t) - (u(x,y,t) - f_x(x,y))\left(f_x^2(x,y) + f_y^2(x,y)\right) \quad [5.18]$$

$$v_t(x,y,t) = \mu\nabla^2 v(x,y,t) - (v(x,y,t) - f_x(x,y))\left(f_x^2(x,y) + f_y^2(x,y)\right) \quad [5.19]$$

The iterative solution to these equations is set up by replacing x, y, and t terms with indices i, j, and k respectively, with Δx and Δy designating the spacings between pixels and Δt as the time step for each iteration. The partial derivatives can be written as

$$u_t = \frac{1}{\Delta t}(u_{i,j}^{k+1} - u_{i,j}^{k})$$

$$v_t = \frac{1}{\Delta t}(v_{i,j}^{k+1} - v_{i,j}^{k})$$

$$\nabla^2 u = \frac{1}{\Delta x \Delta y}\left(u_{i+1,j} + u_{i,j+1} + u_{i-1,j} + u_{i,j-1} - 4u_{i,j}\right)$$

$$\nabla^2 v = \frac{1}{\Delta x \Delta y}\left(v_{i+1,j} + v_{i,j+1} + v_{i-1,j} + v_{i,j-1} - 4v_{i,j}\right)$$

For convenience Xu *et al.*[6] defined:

$$b(x,y) = f_x(x,y)^2 + f_y(x,y)^2$$

$$c^1(x,y) = b(x,y)f_x(x,y)$$

$$c^2(x,y) = b(x,y)f_y(x,y)$$

Substituting the above partial derivatives into equations 5.18 and 5.19 provides the following iterative solution for the GVF:

$$u_{i,j}^{k+1} = \left(1 - b_{i,j}\Delta t\right)u_{i,j}^{k} + r\left(u_{i+1,j}^{k} + u_{i,j+1}^{k} + u_{i-1,j}^{k} + u_{i,j-1}^{k} - 4u_{i,j}^{k}\right) + c_{i,j}^{1}\Delta t \quad [5.20]$$

$$v_{i,j}^{k+1} = \left(1 - b_{i,j}\Delta t\right)v_{i,j}^{k} + r\left(v_{i+1,j}^{k} + v_{i,j+1}^{k} + v_{i-1,j}^{k} + v_{i,j-1}^{k} - 4v_{i,j}^{k}\right) + c_{i,j}^{2}\Delta t \quad [5.21]$$

where $r = \frac{\mu\Delta t}{\Delta x \Delta y}$.

To ensure convergence, the step size Δt, has to be $\Delta t \leq \frac{\Delta x \Delta y}{4\mu}$.

Once the GVF filed (**g**(x,y)) is identified, the external force term ($-\nabla E_{ext}$) in the Euler equation (Eq. 5.9) is substituted with **g**(x,y).

$$c_t(s,t) = \alpha c''(s,t) - \beta c''''(s,t) + \mathbf{g}$$

The equation is then solved through the iteration process such as described above or through gradient descent methods.

5.4 Selection of GVF Approach to Contour Histopathological Lesions

In the context of this project, the balloon approach as described by Cohen *et al.*[254] was preliminarily tested for edge detection of tumor outlines extracted from histology but proved to be inadequate in reaching the caveats so often seen with the lesions, nor did the algorithm perform well with "subjective" contours such as dotted lesion outlines. The balloon snake was often escaping outside the boundaries through the open spaces in the dotted outlines. Since concave, irregular boundaries were a common feature for the lesion regions and the overwhelming majority of lesions were outlined with a dotted line, GVF approach was chosen for its ability to adapt to subjective contours, its superior performance with concavities, as well as the ability to drive the snake toward the boundary from the inside, as well as from the outside the object boundary, which is extremely useful for very small lesions.

5.5 Methods

5.5.1 Histopathological Processing

Prostate specimens obtained in patients undergoing radical prostatectomy were processed according to a research protocol established at this institution. First, all prostate specimens were fixed using injected neutral-buffered formalin for at least 24 hours. Once fixed, each prostate gland was then serially cross-sectioned from apex to base at 3-4 mm intervals using a manual meat slicer (Hobart, Troy, OH, USA). All slices were then embedded in paraffin as whole-mount sections, cut at 4 micron thickness, and stained with hematoxylin and eosin. Each slide was closely examined by a study pathologist under the light microscope with cancerous regions and those corresponding to HGPIN outlined on the slides. A researcher was present during each

histological examination, taking detailed notes and drawings regarding lesion location, composition, etc. The slides were then digitally scanned. Image processing techniques were used to extract the outlined cancerous regions. For the majority of cases, dashed black or blue lines were used to outline the cancerous regions with solid green lines often designating HGPIN regions; however, in some instances this convention was reversed. These discrepancies were noted and corrected during the semi-automatic process of lesion extraction.

5.5.2 Lesion segmentation

Figure 5.4a shows an example of the digitized histopathology slides. Depending on the size of the prostate each patient had from one to three scanned pages worth of histopathology slides. In-house software was written in Matlab (MATLAB, 2016a, The MathWorks Inc., Natick, MA, USA) designed to 1) extract the lesion contours and 2) determine the area of each lesion.

5.5.2.1 Extraction of Lesion Contours

First, prostate segmentation was achieved by manually selecting a small area within the background, as well as an area within one of the prostate slices to get a representative color sample for each of these regions. The RGB (Red (R), Green (G), Blue (B) color spectrum) image (Figure 5.4a) was then transformed into the CIE (Commission Internationale de l'Eclairage) L*a*b* color space (Figure 5.4b). The L*a*b* space mimics human vision by creating a uniform perception space. Each location within the L*a*b* space is defined by three coordinates: L* represents the luminance or brightness, a* defines the location on the red/green axis, while b* specifies the position on the blue/yellow axis. Once the RGB histopathology image was transformed into the L*a*b* space, the a*b* compositions for the sampled colors within the two chosen regions were computed and used as color classifiers – one for the prostate slice and one for the background. Next, for each pixel within the image the Euclidian distance between the

pixel's color and each color classifier was computed. The smaller the distance, the closer the pixel matched the color classifier in question. Nearest neighbor classification was used to group the pixels based on the closest matching color classifier to yield the prostate segmentation results shown in Figure 5.4c. The segmented image was then converted to a binary image as depicted in Figure 5.4d and region-growing techniques were used to create prostate masks, as well as a mask for the ruler seen on the right hand-side (Figure 5.4e), which was later used during pixel to metric units conversion. L*b* image composition was then used to isolate the lesion markings (which appear as blue in L*a*b* space) (Figure 5.4f). The lesion-associated markings were then further refined by applying prostate masks and removing any labels or extraneous pixels (Figure 5.4g). Once downsampled to 5% of the original image size, the dotted regions depicted in the resulting image (Figure 5.4h) served as a starting point for the active contouring algorithm used in lesion size estimation. Once the dotted outlines for the individual lesions were extracted, gradient vector flow (GVF) snakes were used to determine the area of each lesion.

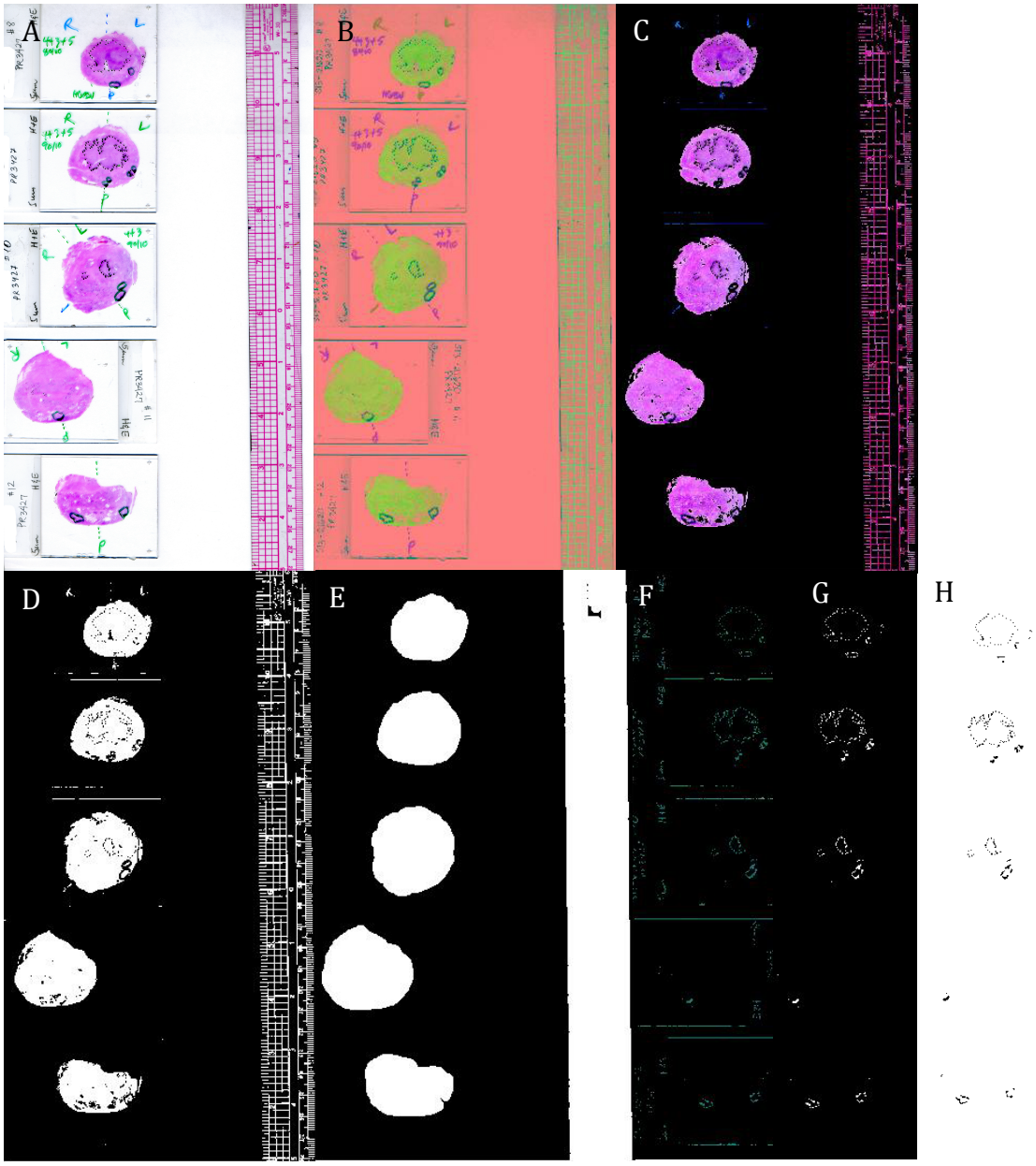

Figure 5.4: a) Example of digitized histopathology slides, with cancerous lesions outlined in black and HGPIN outlined in green. b) RGB image in 5.4a transformed into the L*a*b* space. c) Using L*a*b* color space for prostate segmentation. d) Binary image of the segmented prostates in 5.4c. e) Prostate masks created from the images in 5.4d using the region growing techniques. f) Using L*b* image composition in 5.4b to isolate the lesion markings. g) Extraneous markings are removed and lesions are displayed in a binary image. h) Downsampled complementary image to 5.4g, the starting point for active contouring.

5.5.3 Application of GVF Approach to Contour Histopathological Lesions

Each lesion identified on the histopathology was contoured using the GVF active contouring approach. Depending on the lesion size, a GVF snake was manually initialized by the user to either spread outward (Figure 5.5a) or to converge inward toward the lesion boundary (Figure 5.5b). For lesions larger than 40 pixels in size, a small circular 2 pixel in diameter GVF snake was initialized inside the lesion to spread outward toward the lesion boundaries; conversely, for lesions smaller than 40 pixels, a GVF snake 10 pixels in diameter was initialized to converge inward toward the lesion boundary.

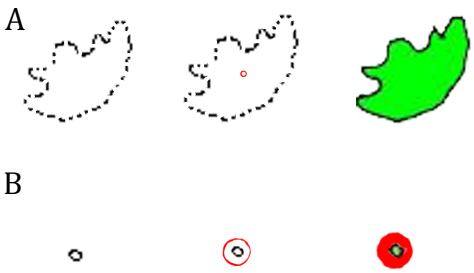

Figure 5.5: Top panel (a) depicts a large lesion (215 mm^2 in size) the snake for which was initialized within the boundary of the lesion. The bottom panel (b) depicts a small lesion (2.2 mm^2 in size) the snake for which was initialized from the outside the boundary of the lesion.

Initially, 1000 iterations were used to contour all lesions. Complete filling of each region was visually confirmed for all lesions. If the lesion was only partially filled after 1000 iterations, the number of iterations was increased to 1300. The time it took to contour each lesion was recorded. Once the lesion was entirely filled, the area in pixels was calculated (Figure 5.6).

Figure 5.6: Iterative process demonstrating the GVF snake spreading out to fill the contours of the lesion. Once the lesion was outlined, the area of the lesion in pixels was computed.

Once the area of each lesion was computed in pixels, a ruler, digitized along with histopathology slides, was used to convert the area values in pixels to cm^2. This was accomplished by isolating the centimeter markings on the ruler and computing the number of pixels within the 1 cm segment. This process was entirely automatic. Along side this automated processing, approximate pixels to cm conversion factor was computed using the size of the digitized image in pixels and the size of the standard 8.5 x 11 inch sheet of paper on which the slides were scanned. The two methods were used in tandem; if the discrepancy in the reported conversion values between the two techniques was more than 1 pixel/cm the user was alerted that a manual check was required to ensure accurate conversion.

5.5.4 Patient Study

Whole-mount histopathology slides from 78 patients who underwent radical prostatectomy for a biopsy-proven prostate cancer were studied. This was approved by the Committee on Human Research at this institution and was compliant with the Health Insurance Portability and Accountability Act. Whole-mount slides were processed in the manner described in 5.5.1. The GVF contouring combined with lesion segmentation procedures described above were used to contour and compute the areas for all the lesions identified by the study pathologist.

5.5.5 Repeatability study

A study was designed to test repeatability of the user initialized GVF snake edge detection technique. Fifteen lesions were randomly chosen – different in size and with varying degrees of concavities within lesion boundaries. For each lesion, the process of snake initialization, lesion contouring, and area computation was repeated 10 times. The coefficient of variation ($COV=\sigma/\mu$, where σ is the standard deviation and μ is the sample mean) was calculated for each lesion.

5.6 Results

5.6.1 Patient Study

A total of 1193 lesions within 78 patients were outlined by the study pathologist. All 1193 lesions were successfully contoured and their areas estimated using the techniques described above. The average lesion size was 307±498 pixels (55±89 mm^2), with lesions varying in size from 6 to 4727 pixels (1 to 849 mm^2). Approximately a quarter of lesions were smaller than 40 pixels in size and required GVF snakes initialized for convergence from outside the lesion boundary. Fewer than 2% of lesions were too large to be entirely filled within the initial setting of 1000 iterations. However, 1300 iterations were enough to completely contour all large lesions. Complete filling of each region was visually confirmed for all lesions. Despite the high number of iterations, it took approximately 13 seconds to contour each lesion.

5.6.2 Repeatability Study

Results for the repeatability study are shown in Figure 5.7. Fifteen lesions used in this study ranged in size from 12 pixels (2.15 mm^2) to 1201 pixels (215.6 mm^2). The smallest COV of 0.0018 was observed for the largest lesion of 1201 pixels (215.6 mm^2), while the largest COV of 0.0166 was noted for a smaller lesion of 77.2 pixels (13.9 mm^2). Interestingly, that was not the smallest lesion tested. The smallest lesions 12 and 13.9 pixels (2.15 and 2.5 mm^2 respectively) in size had comparatively small COV values of 0.003 and 0.006 respectively.

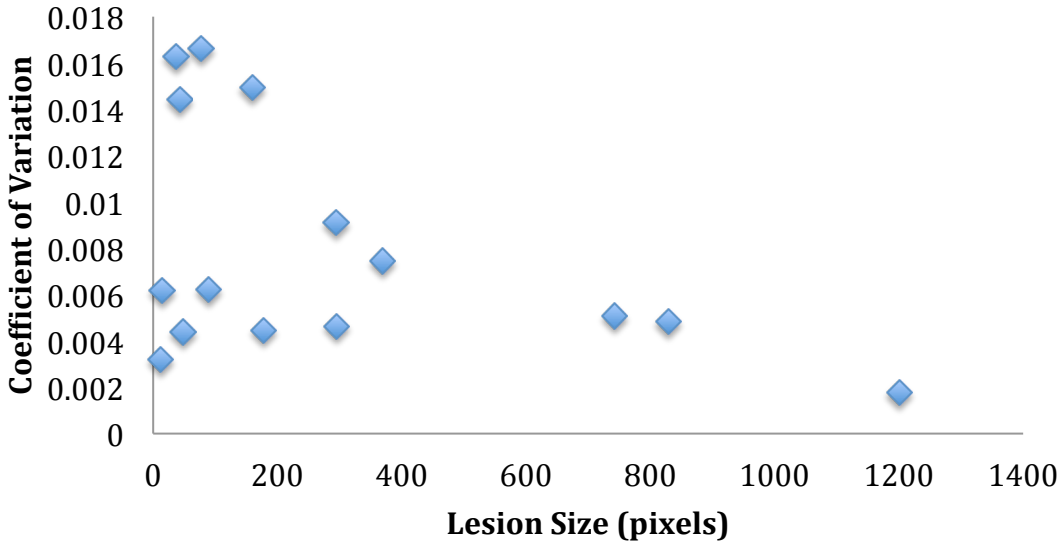

Figure 5.7: The coefficient of variation plotted against the lesion size. Fifteen lesions of varying sizes and concavities were randomly chosen, with snake initialization, active contouring, and area computations repeated 10 times for each lesion.

5.7 Discussion

This study demonstrated the excellent performance of GVF snakes for contouring subjective prostate lesion boundaries segmented from the histopathology slides. The GVF approach was chosen over the traditional active contouring techniques described in 5.3.1 for 1) its ability to adapt to subjective boundaries (such as dotted lesion outlines), 2) its superior performance with concavities (often seen with irregularly shaped lesions), and 3) its ability to drive the contour toward the boundary from the inside, as well as from the outside the lesion boundary (extremely useful for very small lesions).

Nearly 1200 lesions, within a wide range of shapes and sizes, were successfully contoured and their area evaluated using this technique. The small COV values observed in the repeatability study reveal that the use of GVF snakes for countering of the subjective lesions yields consistent results from which the lesion area values can be reliably computed. Additionally, the small COV values observed for even the smallest lesions indicate that the GVF

snakes perform consistently well when the snake converges onto the lesion boundary from the inside (larger lesions), as well as from the inside (smaller lesions).

In conclusion, a semi-automatic technique for lesion segmentation, region contouring and region area estimation has been described. This technique performed well even when applied to "subjective" contours (dotted lesion outlines), with the accuracy and high quality of contouring visually evaluated and confirmed for every cancer region. Additionally, this approach was demonstrated to be robust to the variations in user initialization and to perform well for regions within a wide range of sizes.

CHAPTER 6

Characterizing Sparse and Dense Prostate Cancers on Whole-Mount Histopathology and Evaluating These Lesions on Multiparametric MRI

6.1 Abstract

The study purpose was to establish size, incidence, and Gleason Score (GS) of prostate cancer (PCa) identified on whole-mount histopathology in post-prostatectomy population and to evaluate imaging characteristics associated with sparse cancers on mpMRI. This study included 78 men with untreated PCa who received 3T-MR scans prior to undergoing prostatectomy**.** Post-prostatectomy, all prostate specimens were processed whole-mount. During histological review, cancerous regions on each slide were outlined and graded using the Gleason system, with the amount of cancer in each region estimated. Regions with cancer occupying <50% and ≥50% of the cross-sectional area were considered sparse and dense respectively. Histopathology slides were digitized and processed using in-house software with cancer region sizes estimated. Contiguous 2D cancer regions identified on histopathology were grouped into 3D lesions and their volumes calculated. Lesions were classified as sparse or dense. Sparse lesions were defined in two ways: 1) "purely sparse" lesions were defined as lesions containing only sparse cancerous regions, any lesion containing a dense cancerous region was classified as dense; 2) "overall sparse" lesions were defined as lesions containing <50% overall cancer, any lesion containing ≥50% overall cancer was classified as dense.

On imaging, regions of interest (ROI) were manually drawn freeform in the peripheral zone (PZ) and the transition zone (TZ) on T2-weighted images based on histopathology. Within each patient, ROIs were grouped based on tissue type, Gleason Score, and sparse/dense

composition. Imaging measures consisting of T2-weighted image intensity, apparent diffusion coefficient (ADC), semi-quantitative dynamic contrast-enhanced (DCE) MRI parameters of peak enhancement, maximal enhancement slope, and washout slope were computed. For analysis, ROI area-weighted averages for each imaging measure were calculated for each tissue type and sparse/dense composition per patient. Non-parametric Wilcoxon signed-rank tests were used to compare imaging metrics across tissues of interest.

1193 (939 (PZ) and 254 (TZ)) cancerous regions were identified on histopathology. With "purely sparse" lesion definition, there were 152 dense and 54 sparse PZ lesions, 59 dense and 12 sparse TZ lesions identified. Sparse lesions were primarily low-grade. Within PZ, 53/54 lesions were ≤GS3+3, with a single high-grade GS4+3+5 lesion. Within TZ, all 12 sparse lesions were GS3+3. Using the "overall sparse" approach, 128 dense and 79 sparse PZ lesions and 52 dense and 19 sparse TZ lesions were identified on histopathology. 86% of sparse lesions in the PZ and 100% of sparse lesions in the TZ were ≤GS3+3. With both sparse lesion definitions, dense lesions were significantly larger than sparse lesions in both PZ and TZ.

On imaging, 246 dense and 45 sparse and 109 dense and 8 sparse 2D cancerous ROIs were drawn in the PZ and TZ respectively. Within PZ, no statistically significant differences were found between sparse ≤GS3+3 lesions and sparse ≥G3+4 lesions or ≥G4+3 lesions for any of the imaging metrics. No statistically significant differences were found between sparse and dense ≤GS3+3 lesions or between sparse ≥G3+4 cancers and dense ≤GS3+3 cancers for any of the parameters. Statistically significant differences were found between sparse ≤GS3+3 cancers and normal PZ tissues, as well as between sparse ≤GS3+3 cancers and benign PZ tissues on T2-weighted imaging, ADC, peak enhancement and maximal enhancement slope. No statistically

significant differences were found for TZ tissues; however, the number of sparse TZ lesions was low (N=5).

The size, Gleason grading, and prevalence of sparse cancers on histopathology was characterized. Sparse cancers were entirely low grade (≤G3+3) in the TZ and predominantly low-grade (96% or 83% depending on the definition of sparse lesions) in the PZ and thus likely pose limited malignant potential for spread and progression. Sparse GS3+3 and ≥GS3+4 cancers had similar imaging characteristics to dense GS3+3 cancers; there were statistically significant differences between sparse low-grade cancers and benign tissues on several imaging modalities in the PZ. This suggests that mpMRI may prove valuable for focal treatment planning and establishing lesion margins even in the setting of cancer sparsity.

6.2 Introduction

Prostate cancer (PCa) is extremely common, with one in seven men in the United States expected to receive a prostate cancer diagnosis during his lifetime.[3] However, not all prostate cancers are created equal, some are aggressive and require treatment, while others grow slowly and can be safely left untreated for decades.[5,7,117] It is, therefore, extremely important to be able to separate clinically significant tumors requiring treatment from the slow-growing indolent PCa. Prostate biopsies, often used in PCa diagnosis, are inherently limited by inadequate tumor sampling and frequently fail to convey the full extent of the tumor aggressiveness, thus providing limited confidence when it comes to treatment recommendations.[256,257] Multiparametric magnetic resonance imaging (mpMRI) is a noninvasive technique that has been gaining traction in detection and localization of prostate cancer.[39,142,170,209,258] By evaluating the prostate gland in its entirety, mpMRI sidesteps the greatest limitation associated with the needle biopsies. However, mpMRI comes with its own set of limitations. A major challenge in PCa characterization is posed by the heterogeneity of prostatic tissues. Aside from histologically assigned Gleason grading, which is traditionally used to estimate cancer aggressiveness, prostate cancers can also be categorized as dense or sparse based on the amount of cancerous and normal tissues within the lesion. The inability to detect sparse cancers on imaging is often sited as one of the limitations associated with mpMRI of the prostate.[259,260] However, the clinical relevance of these sparse lesions has remained largely unknown. The purpose of the study was 1) to establish the incidence and Gleason Score of sparse lesions on whole-mount histopathology in post-prostatectomy samples and 2) to identify the imaging characteristics of sparse cancers on mpMRI modalities and discuss their clinical implications.

6.3 Materials and Methods

6.3.1 Patients

This study was approved by the Committee on Human Research at this institution and was compliant with the Health Insurance Portability and Accountability Act. Seventy-eight patients who underwent radical prostatectomy for a biopsy-proven prostate cancer were studied. Patients who underwent any treatment for their prostate cancer prior to surgery, or whose surgery was more than a year after their MRI were excluded from the study. One patient was not included in this study due to the lack of cancerous regions on histopathology. No MRI exam was performed less than 6 weeks after prostate biopsy. This cohort has been described in an earlier study (Chapter 4).

6.3.2 MR Imaging

All patients were imaged with an expandable balloon endorectal coil (MedRad, Bayer HealthCare LLC, Whippany, NJ) combined with an external phased array coil on a 3T MR scanner (GE Healthcare, Waukesha, WI, USA). A perfluorocarbon fluid (Galden; Solvay Plastics, West Deptford, NJ, USA) was used to inflate the balloon coil. Fast spin echo (FSE) T2-weighted images were acquired in an oblique axial plane with FOV = 18cm, slice thickness = 3mm, matrix = 512×512, and TR/TE = 6000/96ms. Diffusion weighted imaging (DWI) was acquired using a 2D single-shot spin echo sequence TR/TE=4000/78-90ms, pixel bandwidth = 1952 (conventional acquisition), pixel bandwidth = 1305 (reduced-field-of-view acquisition)[101], b=0 and 600 s/mm^2, slice thickness=3mm. DCE MRI was performed using a 3D fast SPGR sequence with TR/TE = 3.5/0.9ms, flip angle = 5°, slice thickness = 3mm slices, and a single-dose of gadopentetate dimeglumine (Gd-DTPA) (Bayer, Whippany, NJ) over ~5 minutes. The acquisition parameters are outlined in Table 6.1. T2-weighted images were corrected for the inhomogeneous reception profile associated with the combined endorectal coil and the external

phased array.[67] Apparent diffusion coefficient (ADC) maps were created using an in-house software from the combined DWI (b=600 s/mm^2) and T2-weighted reference images (b=0 s/mm^2). DCE MRI maps were created based on the semi-quantitative tissue enhancement parameters of peak enhancement, maximal enhancement slope, and washout rate.[132]

Table 6.1: Scanning Parameters

Imaging	PSD	TR/TE (ms)	FOV (cm)	Matrix Size	NEX	ST (mm)	In-Plane Res. (mm)	Temp. Res. (s)	b-value (s/mm^2)
T2w	FSE	6000/100	18x18	512x512	1	3	0.35x0.35	N/A	N/A
Conv ADC	ss-EPI	4000/90	24x24	128x128	4	3	0.94x0.94	N/A	0, 600
rFOV ADC	ss=EPI	4000/90	18x9	128x64	6	3	0.70x0.70	N/A	0, 600
DCE	3D SPGR	3.5/0.9	26x26	256x256	0	3	1.02x1.02	10.417	N/A

PSD=pulse sequence design, ST= slice thickness, Res=resolution, T2w = T2-weighted MRI, Conv = conventional, rFOV=reduced FOV.

6.3.3 Whole Mount Histopathology

Following prostatectomy, all prostate specimens were fixed using injected neutral-buffered formalin for at least 24 hours. The prostates were then serially cross-sectioned from apex to base at 3-4mm intervals using a manual meat slicer (Hobart, Troy, OH, USA). All slices were then embedded in paraffin as whole-mount sections, cut at 4μm thickness, and stained with hematoxylin and eosin. The study pathologists then examined the slides under light microscopy, marking the regions of interest. Following the pathology review, the slides were digitally scanned for comparison to the MR images.

6.3.4 Identifying Regions of Interest

During histological review, cancerous regions on each slide were outlined and graded by the study pathologist using the Gleason system;[12] the amount of cancer in each region was estimated, along with the various fractions of each Gleason grade in each cancer region. In addition to cancer, percentages of HGPIN if present within a cancer region were reported. Finally, the amounts of benign glandular tissue and of stromal tissue within each cancerous region were also estimated. Next, regions of interest were manually drawn freeform on T2-

weighted images based on the digitized histopathology slides using anatomical cues, following a consensus of two readers, and keeping within homogeneous regions.

6.3.5 Histopathology Segmentation

A semiautomatic in-house software written in Matlab (MATLAB, 2016a, The MathWorks Inc., Natick, MA, USA) was used to segment the outlines of the individual cancer regions from the digitized histopathology slides. Following cancer region segmentation, gradient vector flow (GVF)[6,251,255] contouring was used to determine the area of each cancerous region. For further information on cancer region segmentation, the theory of GVF snakes, and the details regarding this post-processing technique please see Chapter 5.

6.3.6 Defining Sparsity and Identifying Sparse Lesions

6.3.6.1 Histopathology

Cancerous regions outlined on histopathology were classified as dense if 50% or more of the cross-sectional area was occupied by cancer; conversely, sparse cancerous regions were regions with less than 50% of the cross-sectional area occupied by cancer. Cancerous regions were grouped into lesions based on their locations on the adjacent histopathology slices. Assigning the overall Gleason Score and sparsity to the lesion was done in two ways. 1) The Gleason Score was assigned based on the most aggressive cancerous region within the lesion. "Purely sparse" lesions were defined as lesions containing only sparse cancerous regions. Any lesion containing a dense cancerous region was classified as dense. 2) Since the individual Gleason Grade percentages were available for every cancerous region of interest, Gleason Score of the lesion was computed as a cumulative result of all the cancerous regions included within the lesion weighted by the area of each cancerous region. "Overall sparse" lesions were defined as lesions containing less than 50% overall cancer. For each lesion a lesion volume was

computed by multiplying the total area of the included cancerous regions by the thickness of the cross sectional prostate slices (3mm).

6.3.6.2 mpMRI

In the context of imaging studies, sparsity within individual ROIs was defined in the following way: ROIs with cancer occupying 50% or more of the cross-sectional area were considered dense, while ROIs with cancer occupying less 50% of the cross-sectional area were considered sparse. For each patient, ROIs were grouped based on the location within the prostate (PZ/TZ), tissue type, Gleason score category (when applicable), and sparsity. A weighted average was calculated using ROI areas for each imaging measure. Based on these criteria, sparse lesions only contained sparse ROIs.

6.3.7 Statistical Analysis

Statistical analysis was carried out using JMP software (JMP, Version 11, SAS Institute Inc., Cary, NC). A p-value of 0.05 or less was used to define statistical significance. Analyses were done separately for tissues in the peripheral zone and for tissues in the transition zone. Descriptive statistics were listed as mean ± standard deviation when normally distributed. Two-tailed, heteroscedastic Student's t-tests were used to compare the sizes of dense and sparse lesions on histopathology. Additionally, two-tailed, heteroscedastic Student's t-tests were used to compare the volumes of the sparse, low-grade lesions and the rest (grouping sparse, higher-grade lesions and dense lesions). Non-parametric Wilcoxon signed-rank tests were used to compare the imaging parameters of interest across tissue types. Imaging metrics for sparse tissues of differing Gleason Scores were compared, as well as imaging parameters for sparse tissues and dense tissues, sparse tissues and normal tissues, and finally sparse tissues and benign tissues were compared. The normal tissues were defined to include: 1) in the PZ - normal PZ tissues and

cystic atrophy located in the PZ; and 2) in the TZ - normal TZ tissues and cystic atrophy located in the TZ. The benign tissues were defined to include: 1) in the PZ – normal PZ tissues, cystic atrophy, atrophy, and inflammation located in the PZ; and 2) in the TZ – normal CG tissues, cystic atrophy, atrophy, inflammation, and benign prostatic hyperplasia located in the TZ.

6.4 Results

6.4.1 Histopathology

A total of 1193 cancerous regions were drawn for 77 patients, 939 cancerous regions were drawn within the peripheral zone and 254 regions were drawn within the transition zone of the prostates (Table 6.2). Cancerous regions ranged in size from 0.01cm^2 to 8.49cm^2. Figure 6.1 demonstrates the distribution of tissues types observed for dense and sparse cancerous regions on histopathology. The contributors listed are the benign glandular and stromal tissues, cancer, and HGPIN. The zonal breakdown and the exact percentages of tissue types found are summarized in more detail in Table 6.2.

Table 6.2 Number of **cancer regions** outlined on histopathology, the areas of cancer regions outlined on histopathology and the distribution of tissues types within dense and sparse cancer regions.

Zonal Anatomy and Sparsity	**Histopathology Outlined Cancer Regions (N)**	**Histopathology Outlined Cancer Regions Area (cm^2)**	**Tissue Types**			
			Glandular (% Lesion)	Stromal (% Lesion)	Cancer (% Lesion)	HGPIN (% Lesion)
Dense PZ	571	0.77±1.12	3	27	69	1
Dense TZ	176	0.63±0.70	1	27	71	0
Dense Overall	**747**	**0.73±1.04**	**3**	**27**	**70**	**1**
Sparse PZ	368	0.25±0.42	11	58	25	5
Sparse TZ	78	0.23±0.41	6	65	26	1
Sparse Overall	**446**	**0.24±0.42**	**10**	**59**	**25**	**4**

Area values are displayed as Mean ± Standard deviation

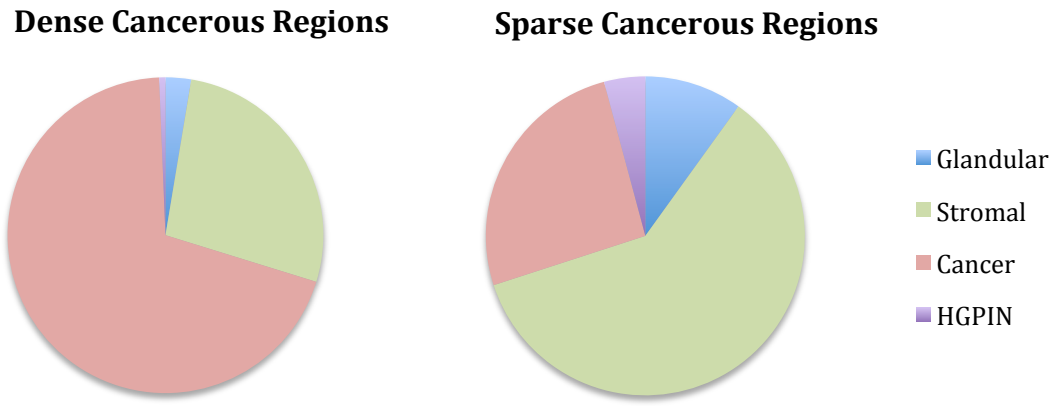

Figure 6.1: Distribution of tissue types within dense and sparse prostatic cancer regions. The presence of glandular, stromal, cancer, and high-grade prostatic intraepithelial neoplasia (HGPIN) tissues in dense and sparse prostatic cancer regions located within the peripheral or the transition zones of the prostate based on histopathological evaluation.

Table 6.3 summarizes the Gleason Score distribution found in the cancerous regions split based on the location within the prostate and the sparsity of the cancerous regions. The 1193 cancerous regions were grouped into 277 lesions; 206 lesions were classified as peripheral zone lesions, while 71 lesions belonged to the transition zone.

Table 6.3 Histopathology: dense and sparse **cancerous regions** separated by zone and Gleason Score

Gleason Score	**Peripheral Zone**		**Transition Zone**	
	Dense	Sparse	Dense	Sparse
2+2	0	1	1	0
2+3	4	4	5	0
3+2	14	2	6	1
3+3	254	298	89	73
3+4	99	12	23	0
3+5	2	1	1	0
4+3	73	23	32	3
4+4	52	8	13	1
4+5	24	7	1	0
5+2	0	1	0	0
5+3	7	3	0	0
5+4	20	5	0	0
5+5	15	0	3	0
3+4+5	1	0	2	0
4+3+5	6	3	0	0
Total (N)	**571**	**368**	**176**	**78**

Sparse cancerous regions were defined as 2D regions with cancer occupying <50% of cross-sectional area of the region

First, the "purely sparse" lesions containing only sparse cancerous regions were studied. Using these criteria, there were 152 dense and 54 sparse PZ lesions, 59 dense and 12 sparse TZ lesions identified. Dense lesions had similar cancer compositions across the prostate zones, with 66.3±10.4% and 67.7±11.9% cancer reported for PZ and TZ lesions. A similar cancer composition was also noted for PZ and TZ sparse lesions with 28.2±10.3% and 28.9±10.3% cancer respectively. Dense lesions were significantly larger than sparse lesions in both PZ (1.03±1.78cc > 0.063±0.08cc, $p=4x10^{-10}$) and TZ (0.61±0.82cc > 0.079±0.06cc, $p=6.4x10^{-6}$). Sparse lesions were also primarily low-grade. Within the PZ, out of the 54 sparse lesions, 53 had a Gleason Score of GS3+3 or lower and only one lesion had a higher Gleason Score of GS4+3+5. Within the TZ, all 12 sparse lesions were GS3+3 (Table 6.4). The distribution of Gleason Scores across dense and sparse lesions in the PZ and TZ are summarized in Table 6.4.

Table 6.4 Histopathology: number of dense and sparse **lesions** separated by zone and Gleason Score

Gleason	**Peripheral Zone**		**Transition Zone**	
Score	Dense	Sparse	Dense	Sparse
≤3+3	67	53	32	12
3+4	17	0	8	0
4+3	25	0	9	0
≥4+4	43	1	10	0
Total (N)	**152**	**54**	**59**	**12**

"Purely sparse" lesions defined as 3D lesions containing only sparse cancerous regions

Second, the "overall sparse" lesions, containing both sparse and dense cancer regions but with the overall percent cancer of less than 50% were studied. This differs from the first approach of "purely sparse" lesions in that these sparse lesions may have foci that are dense, but also contain sufficiently large enough and sparse enough other regions to result in an overall percentage of cancer < 50% of the entire lesion. Using this "overall sparse" approach, there were 128 dense and 79 sparse PZ lesions, 52 dense and 19 sparse TZ lesions. Dense lesions within the PZ and TZ had similar cancer composition, with 66±10.5% and 67±11.7% reported for PZ and

TZ lesions. Once again, dense lesions were statistically larger than sparse lesions in both PZ (1.13±1.88cc > 0.22±0.51cc, $p=7.9x10^{-7}$) and TZ (0.60±0.84cc and 0.22±0.30cc, p=0.008). The distribution of Gleason Scores across dense and sparse lesions in the PZ and TZ is summarized in Table 6.5.

Table 6.5 Histopathology: number of dense and sparse **lesions** separated by zone and Gleason Score

Gleason	**Peripheral Zone**		**Transition Zone**	
Score	Dense	Sparse	Dense	Sparse
≤3+3	64	68	30	19
3+4	26	6	11	0
4+3	18	3	9	0
≥4+4	20	2	2	0
Total (N)	**128**	**79**	**52**	**19**

"Overall sparse" lesions defined as 3D lesions containing <50% cancer overall

Figures 6.2 and 6.3 depict the relationship between the Gleason Scores, the percent cancer, and the lesion volumes for lesions in the PZ and the TZ respectively. The two plots are drawn to the same scale; meaning, the differences in bubble sizes represent the true differences between the lesion volumes within the peripheral and the transition zones. Lesions in the sparse and low-grade regions (low left quadrant) for both PZ and TZ plots were smaller in volume than their dense or more aggressive counterparts ($p=9x10^{-10}$ for PZ and p=0.008 for TZ). The majority of large lesions both within the PZ and TZ were predominantly found in the dense, higher-grade quadrants (upper right quadrant). Within the TZ, there were no higher-grade sparse lesions observed. There was one of each GS8 and GS9 lesions found within the sparse PZ lesions, which were 1.3cc and 3.75cc in volume respectively.

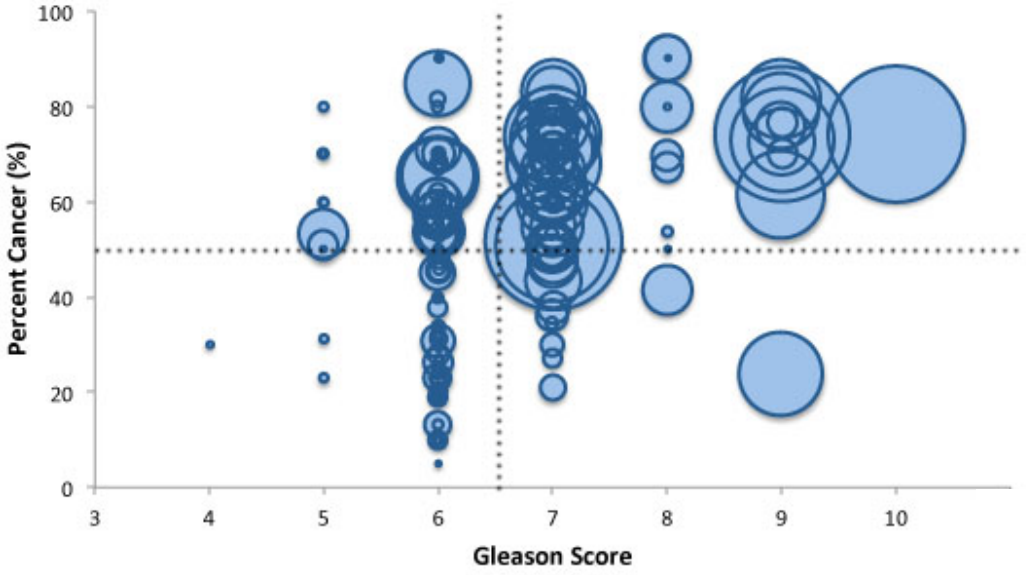

Figure 6.2: Bubble plot of 3D PZ lesions: percent cancer of the lesion plotted against the Gleason Score of the lesion, with the size of the bubbles representing lesion volumes. The horizontal dotted line represents sparsity (everything below 50% cancer considered sparse); the vertical dotted line represents aggressiveness with everything of Gleason Score 6 or lower considered low-grade.

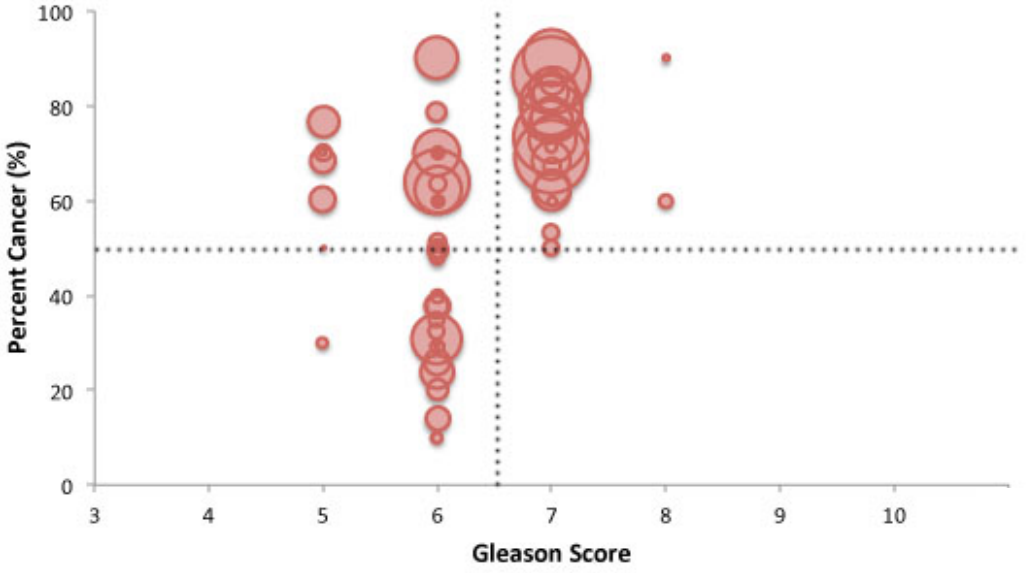

Figure 6.3: Bubble plot of 3D TZ lesions: percent cancer of the lesion plotted against the Gleason Score of the lesion, with the size of the bubbles representing lesion volumes. The horizontal dotted line represents sparsity (everything below 50% cancer considered sparse); the vertical dotted line represents aggressiveness with everything Gleason Score 6 or lower considered low-grade.

6.4.2 mpMRI

On imaging, 246 dense and 45 sparse cancerous 2D ROIs were drawn in the PZ and 109 dense and 8 sparse 2D ROIs were drawn in the TZ. On average, dense and sparse ROIs in the PZ were 0.75±0.83 cm^2 and 0.41±0.22 cm^2 in size with 70.9±11.6% and 29.6±8.8% cancer. Within the TZ, on average dense and sparse ROIs were 0.54±0.32 cm^2 and 0.38±0.19 cm^2 in size containing 76.1±9.9% and 28.4±11.6% cancer. Table 6.6 describes the distribution of Gleason Scores across the regions of interest drawn on MR imaging in the PZ and the TZ.

Table 6.6 MR imaging: dense and sparse **cancerous regions** separated by zone and Gleason Score

Gleason Score	**Peripheral Zone**		**Transition Zone**	
	Dense	Sparse	Dense	Sparse
2+3	0	0	1	0
3+2	1	0	9	1
3+3	55	29	30	7
3+4	78	3	37	0
3+5	0	0	2	0
4+3	42	5	23	0
4+4	22	1	5	0
4+5	19	5	0	0
5+2	0	0	0	0
5+3	8	2	0	0
5+4	9	0	0	0
5+5	10	0	0	0
4+3+5	2	0	2	0
Total (N)	**246**	**45**	**109**	**8**

Sparse 2D cancerous regions were defined as regions with cancer occupying <50% of cross-sectional area of the region

These cancerous 2D regions were grouped into sparse and dense lesions. The distribution of Gleason Scores across sparse and dense lesions outlined on MR imaging in the PZ and the TZ is summarized in Table 6.7. In addition to grouping cancer regions, benign regions were grouped to yield 68 benign volumes in the PZ and 61 benign volumes in the TZ. Normal tissues regions were grouped into 62 normal tissue volumes within the PZ and 42 normal tissue volumes in the TZ.

Table 6.7 MR Imaging: number of dense and sparse lesions separated by zone and Gleason Score

Gleason Score	Peripheral Zone		Transition Zone	
	Dense	Sparse	Dense	Sparse
≤3+3	22	18	14	5
3+4	24	3	11	0
4+3	18	5	8	0
≥4+4	21	4	4	0
Total (N)	**85**	**30**	**37**	**5**

Sparse lesions were defined as 3D lesions containing only sparse cancerous ROIs

Figure 6.4 demonstrates an example of a dense GS4+3 cancer region (top panel) and a sparse G4+3 cancer region (bottom panel) as these regions appear on mpMRI modalities: T2-weighted imaging, ADC maps, and maximal enhancement slope maps. These regions belong to the same lesion; however, while the dense region contains 60% cancer, the sparse region contains only 30% cancer. As expected, the cancer in the dense region appears more aggressive on all modalities than the cancer in the sparse region. Without the knowledge of the histopathological grading, based on its appearance on imaging alone, the sparse cancer region could be confused for a low-grade disease.

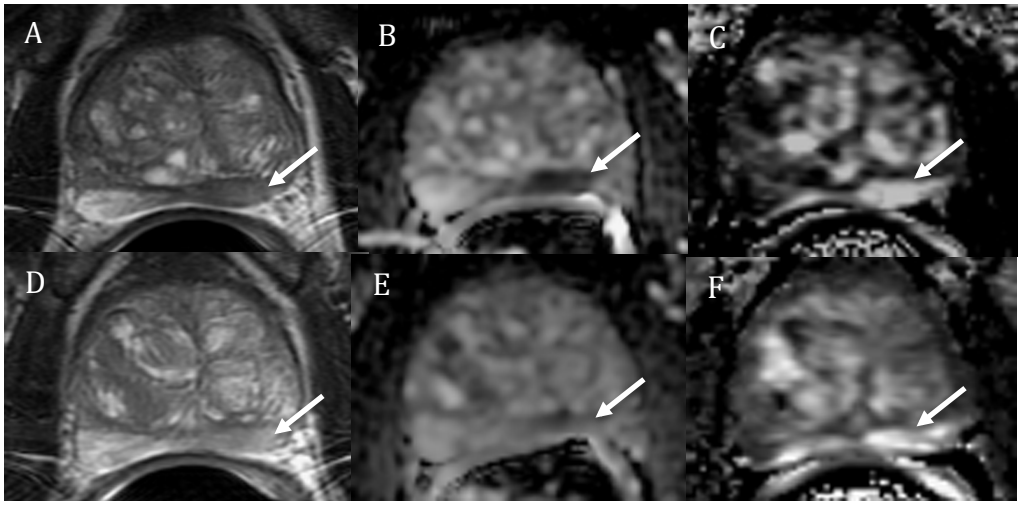

Figure 6.4: A 74 year-old male with serum PSA of 10.3 ng/ml who underwent radical prostatectomy. Top panel: dense GS4+3 cancer (60% cancer): a) coil-corrected T2-weighted image, b) ADC map C) maximal enhancement slope. Bottom panel: sparse GS4+3 cancer (30% cancer): d) coil-corrected T2-weighted image, e) ADC map f) maximal enhancement slope. The arrows designate cancerous regions.

MpMRI results were reviewed to determine whether imaging could be used to distinguish sparse cancers from other tissue types. Within the PZ, no statistically significant differences were found when sparse ≤GS3+3 lesions were compared to sparse ≥G3+4 lesions (N=29) or ≥G4+3 lesions (N=9) for any of the imaging metrics. No statistically significant differences were found between sparse and dense ≤GS3+3 lesions or between sparse ≥G3+4 cancers and dense ≤GS3+3 cancers for any of the parameters. Statistically significant differences were found between sparse ≤GS3+3 cancers and normal PZ tissues on T2-weighted imaging ($p=0.0001$), ADC ($p<0.0001$), peak enhancement ($p=0.037$) and maximal enhancement slope ($p=0.015$). Additionally, statistically significant differences were found between ≤GS3+3 cancers and benign PZ tissues also on the T2-weighted imaging ($p=0.0006$), ADC ($p<0.0001$), peak enhancement ($p=0.043$) and maximal enhancement slope ($p=0.025$) (Figure 6.5).

Within the TZ, the number of sparse lesions was low (N=5) and included only GS3+3 cancers. No statistically significant differences were found between dense and sparse GS3+3 lesions in the TZ. Furthermore, no statistically significant differences were found between sparse GS3+3 cancers and benign TZ tissues, or sparse GS3+3 cancers and normal TZ tissues for any of the imaging modalities.

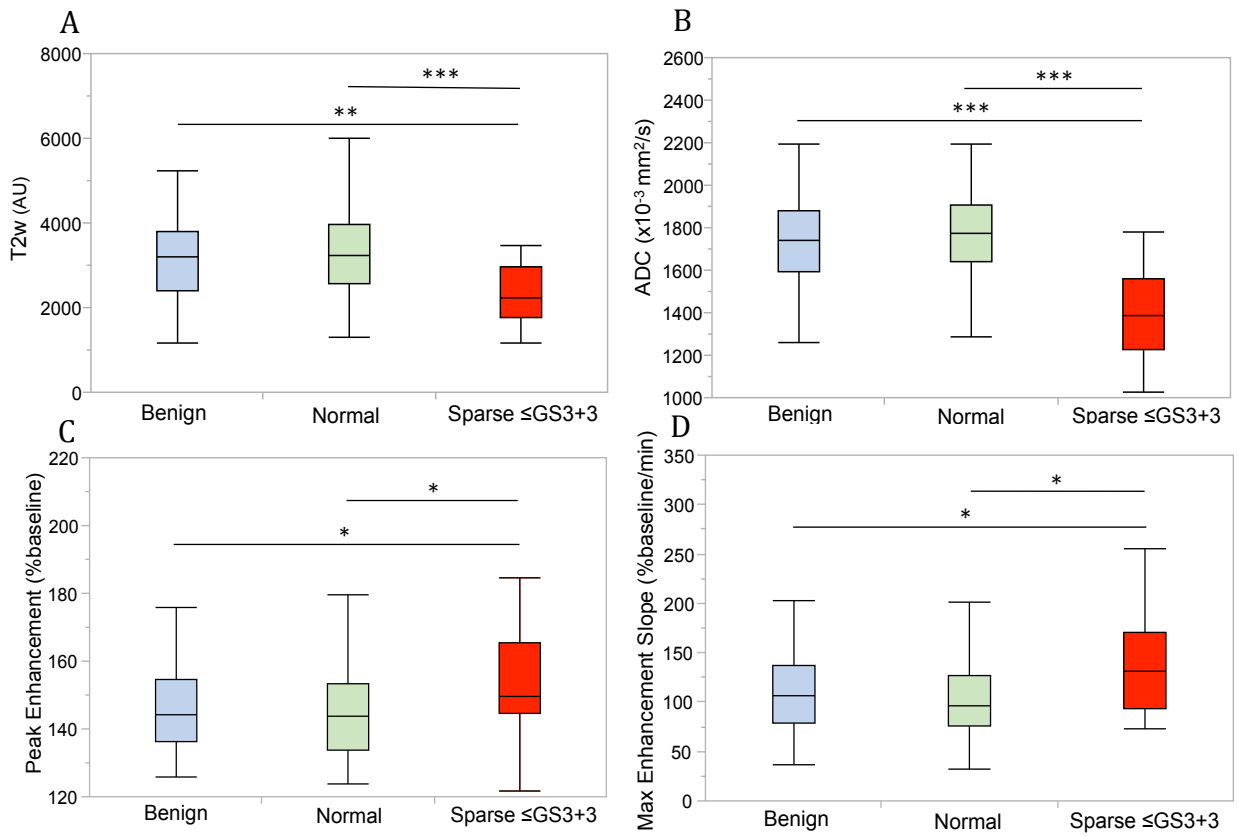

Figure 6.5: Box-plots comparing MR measures in benign, normal, and sparse ≤GS3+3 cancers for A) T2-weighted intensity, B) ADC, C) Peak Enhancement, D) Maximal Enhancement Slope Horizontal lines within the box plots represent the median values. Whiskers are drawn to the furthest points within 1.5x interquartile range, where interquartile range is the difference between the 1st and the 3rd quartiles.
*** <0.0001, ** <0.001, * <0.05

6.5 Discussion

Prostate cancer has been the subject of intense study for decades.[261] A lot is now known about its histological appearance,[11,12,20,31] molecular signatures,[262,263] treatment options,[5,261,264] and imaging characteristics;[39,170,265] however, the concept of cancer sparsity when applied to prostatic lesions has not been thoroughly explored. Very little information is available regarding the incidence of sparse lesions or their clinical significance. To our knowledge no study has looked at the prevalence of sparse cancers in the radical prostatectomy population, nor attempted to characterize the composition, size, or Gleason grading of these sparse cancers. Perhaps not

surprisingly mpMRI characterization of sparse lesions has also been limited; the most widely cited imaging publication available on the subject by Langer *et al.*, with N=10 patients scanned at 1.5T, reported no statistically significant differences between sparse cancers and normal tissues on T2-weighted imaging or ADC.[266]

6.5.1 Histopathology

Consistent with literature,[266] we defined dense regions as those with 50% or more of the cross-sectional area occupied by cancer, while sparse cancerous regions were defined as regions with less than 50% of the cross-sectional area occupied by cancer. Out of the 1193 cancerous regions outlined on histopathology slides obtained from 77 patients, 39% of cancer regions in the PZ and 31% of cancer regions in the TZ were classified as sparse. Sparse regions contained on average 25% cancer (vs. 70% cancer seen for dense regions) and were predominantly low-grade; nearly 83% of sparse PZ cancerous regions were ≤GS3+3 and nearly 95% of sparse TZ cancerous regions were ≤GS3+3.

While it is informative to look at the individual cancerous regions, it is also important to look at sparsity in the context of cancerous lesions. Differences in lesion composition are associated with differences in disease progression and malignant potential, as well as our ability to detect these lesions either through biopsies or imaging. Classifying lesions as sparse is not trivial and can be done in a number of ways. One approach would be to characterize purely sparse 3D lesions. Another approach would be to take a closer look at how sparse regions contribute to the overall composition of a 3D lesion.

Our first approach was to define “purely sparse” lesions as those containing only sparse cancerous regions. Thus, these lesions were homogeneously sparse. When viewed in this way, our prostate cancer histopathological findings suggest that on average “purely sparse” lesions are

much smaller than dense lesions (0.061cc vs 1.03cc in PZ) and (0.079cc vs 0.61cc in TZ) and are primarily low-grade. While the majority of lesions were smaller than 0.1cc in volume, the largest purely sparse lesions found in the PZ and TZ were 0.44cc and 0.22cc in volume, which suggests that sparse cancers as they grow do not necessarily acquire a dense core but may retain their diffuse nature. In the TZ, all 12 sparse lesions were GS3+3; while in the PZ, 53/54 lesions were ≤GS3+3 with only a single higher-grade (GS4+3+5) lesion identified. As small size and low-grade cancers have minimal metastatic potential,[267] these histopathological findings that the purely sparse lesions are small and primarily low grade, suggest they have limited clinical significance. The patient with the single high-grade sparse GS4+3+5 lesion (0.175cc) also had two larger, dense GS4+3 (1.04cc) and GS3+4 (1.13cc) lesions. In the future, it might be informative to study the progression of sparse cancers in the setting of exclusively benign tissues versus in the presence of high-grade prostatic disease.

Our second "overall sparse" approach consisted of defining sparse lesions as containing less than 50% of cancer overall. Sparse and dense regions comprising each lesion were combined with their Gleason Score contributions weight-averaged based on the area of each region. Thus, these "overall sparse" lesions, in addition to sparse regions, had a dense focus to them. Viewed in this way, 86% of sparse lesions in the PZ and 100% of sparse lesions in the TZ were ≤GS3+3, compared to 50% of dense lesions in the PZ and 58% of dense lesion in the TZ being low grade. With this approach, the "overall sparse" lesions were still smaller in size than their dense counterparts but not as drastically as seen above (0.22cc vs 1.13cc for sparse and dense lesions in the PZ) and (0.22 cc vs 0.6cc for sparse and dense lesions in the TZ). A Gleason 4 component identified in 11/79 sparse lesions in the PZ points to the clinical significance of these lesions. The heterogeneity and the diffuse nature of these lesions reemphasizes the drawbacks of TRUS-

guided biopsies that may capture a small segment of a sparse region, missing a dense or a more aggressive portion of the lesion.

6.5.2 mpMRI

Compared to cancer regions drawn on histopathology, cancer regions drawn on MRI images were fewer in number (especially true for low grade regions) and were similar in size for dense lesions but on average slightly smaller in size for sparse lesions ($0.50\pm0.65cm^2$ on histopathology vs. $0.40\pm0.65cm^2$ on MR imaging). This observation foreshadows the fact that sparse cancers (partly due to their diffuse nature and partly due to their predominantly low grade) are not always easy to identify on imaging.

Looking at imaging metrics, no statistically significant differences were found between sparse GS3+3 and ≥GS3+4 cancers or sparse and dense GS3+3 cancers in the PZ. Interestingly, despite our inability to differentiate low-grade sparse and dense lesions, we did find statistically significant differences between GS3+3 sparse and benign tissues on T2-weighted imaging, ADC, peak enhancement, and maximal enhancement slope. An explanation for this may lie in the composition of sparse regions. From Figure 6.1 sparse regions are seen as being composed predominantly of stromal tissues with smaller contributions from cancer and glandular tissues. Stromal tissues typically appear dark and have a “cancer-like” appearance, which could explain why it is hard to distinguish between the dense and the sparse cancers on imaging. It also explains why it is still possible to differentiate between the sparse GS3+3 cancers and benign tissues, which are more glandular in nature and provide a better contrast to stromal-dominated sparse cancer lesions.

Our ability to distinguish between sparse low-grade lesions and benign tissues on mpMR imaging is of clinical significance since accurate evaluation of the extent of the disease is

important for treatment planning. Sparse regions are often found at the periphery of dense cancerous regions, which are more easily detected on mpMRI (chapter 4). Since effective focal treatments are impossible to achieve without identifying accurate lesion margins, our findings suggest that even very straight forward imaging metrics – T2-weighted image intensity, ADC, and semi-quantitative evaluation of DCE studies (especially in the PZ) are capable of providing sufficient cancer margins in the presence of sparse PCa are promising.

Our findings in the TZ were less encouraging. No statistically significant differences were found on imaging parameters for TZ tissues when sparse GS3+3 cancers were compared to dense GS3+3 cancer, nor when sparse G3+3 cancers were compared to benign or normal TZ tissues. While our lack of imaging findings in the TZ may reflect the true standing of sparse cancer imaging in that region, no reliable conclusions can be drawn from this data due to the low number of sparse TZ lesions identified on MR imaging (N=5).

While the majority of sparse lesions are small, low-grade, and may never progress enough to require treatment, there are exceptions. For instance, in Figure 6.2, there are two outliers in the sparse PZ region, representing two high-grade lesions. These sparse GS8 and GS9 lesions are not only aggressive in their Gleason grading but are also concerning due to their large size – 1.3cc and 3.75cc in volume respectively. These lesions cannot be overlooked. The good news is that despite their sparsity, high-grade lesions such as the ones described above are detectable on mpMRI imaging. Figure 6.6 depicts a prostate slice containing a sparse GS4+5 cancerous region (20% cancer). This 2D GS4+5 cancerous region is part of the 3D sparse GS9 lesion discussed above. While the cancer may not be obvious on T2-weighted imaging, a signal reduction on ADC map and an elevated enhancement on maximal enhancement slope map clearly indicate the presence of malignancy.

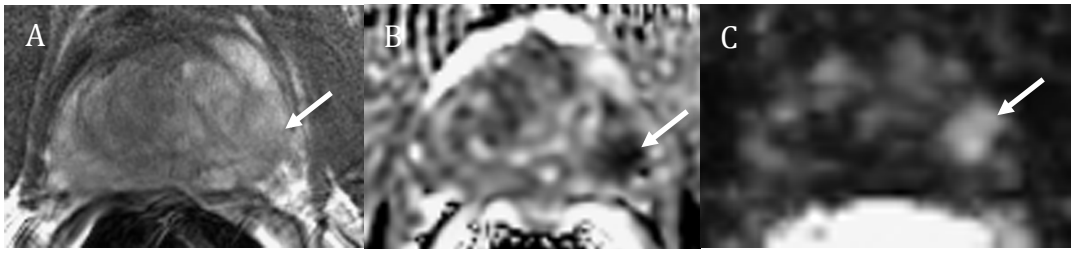

Figure 6.6: A 60 year-old male with serum PSA of 9.3 ng/ml who underwent radical prostatectomy. Sparse GS4+5 cancer (20% cancer) as seen on: a) coil-corrected T2-weighted image, b) ADC map C) maximal enhancement slope. The arrows designate cancerous regions.

This study had several limitations. First, the regions of interest were manually drawn on MR images based on the histopathology; this approach likely introduced the bias toward outlining regions visible on MR, likely corresponding to more aggressive disease. Second, MR sequences were manually aligned to each other based on visual assessment; small shifts in alignment could have taken place and influenced the results. Third, analyses in the TZ were confounded by the low numbers of sparse ROIs drawn on MR images.

In conclusion, we characterized the prevalence of sparse cancers on histopathology. We established that sparse GS3+3 and ≥GS3+4 cancers have similar imaging characteristics to dense GS3+3 cancers, but we were able to find statistically significant differences between sparse low-grade cancers and benign tissues on several imaging modalities in the PZ. This suggests that mpMRI may prove valuable for focal treatment planning and establishing lesion margins even in the setting of cancer sparsity. Further study of sparse cancers on mpMRI especially in the TZ is needed to fully understand the limitations of imaging when it comes to sparse lesion detection. The encouraging news is that based on our histopathology findings, sparse cancers were entirely low grade (≤G3+3) in the TZ and predominantly low-grade (83%) in the PZ and thus overall may pose limited malignant potential for spread and progression.

CHAPTER 7

Improved Multiparametric MRI Discrimination Between Low-Risk Prostate Cancer and Benign Tissues in a Small Cohort of 5-alpha Reductase Inhibitor Treated Individuals as Compared to an Untreated Cohort

Parts of this chapter are reprinted from "Improved multiparametric MRI discrimination between low-risk prostate cancer and benign tissues in a small cohort of 5α-reductase inhibitor treated individuals as compared with an untreated cohort" by Olga Starobinets, John Kurhanewicz, and Susan M Noworolski. The manuscript has been accepted for publication in *NMR in Biomedicine* and is available in early view (doi: 10.1002/nbm.3696).

7.1 Abstract

The purpose of the study was to determine whether 5α-reductase inhibitors (5-ARIs) affect the discrimination between low-grade prostate cancer (PCa) and benign tissues on mpMRI. Twenty men with biopsy-proven Gleason 3+3 PCa and 3T mpMRI were studied. Ten patients (Tx) were receiving 5-ARIs for at least a year at scan time. Ten untreated patients (Un) were matched to the treated cohort. For each subject two regions of interest (ROI) representing cancerous and benign tissues were drawn within the peripheral zone of each prostate, MR measures evaluated, and cancer contrast versus benign [Contrast=$(MR_{Tumor}-MR_{Healthy})/MR_{Healthy}$] calculated. Decreased cancer contrast was noted on T2-weighted images: 0.4 (Un) versus 0.3 (Tx). However, for functional MR measures, a better separation of cancerous and benign tissues was observed in the treated group. Cancer contrast on high-b diffusion weighted images (DWI) was 0.61 (Un) vs. 0.99 (Tx). Logistic regression analysis yielded higher AUC (area under the

curve) values for distinguishing cancerous from benign regions in treated subjects on high-b DWI [0.71 (Un), 0.94 (Tx)], maximal enhancement slope [0.95 (Un), 1 (Tx)], peak enhancement [0.84 (Un), 0.93 (Tx)], washout slope [0.78 (Un), 0.99 (Tx)], K^{trans} [0.9 (Un), 1 (Tx)], and combined measures [0.86 (Un), 0.99 (Tx)]. Coefficients of variation for MR measures were lower in benign and cancerous tissues in the treated group compared to the untreated group. This study's results suggest an increase in homogeneity of benign and malignant peripheral zone prostatic tissues with 5-ARI exposure, observed as reduced variability of MR measures after treatment. Cancer discrimination was lower with T2-weighted imaging, but was higher with functional MR measures in a 5-ARI-treated cohort compared to controls.

7.2 Introduction

One in seven men in the United States will be diagnosed with prostate cancer (PCa) during his lifetime.[268] Currently, prostate cancer is most often detected on systematic ultrasound-guided biopsies prompted by elevated serum prostate specific antigen (PSA) levels. Unfortunately, prostate biopsies are often associated with discomfort, pain, hematuria, rectal bleeding and carry a risk of infection.[214] Additionally, prostate biopsies are inherently limited by sampling errors.[256,257] In recent years, multiparametric magnetic resonance imaging (mpMRI) has emerged as a powerful noninvasive technique for diagnosis, localization, and staging of prostate cancer.[39,142,170,209,258] A growing number of studies attest to the utility of mpMRI in detecting prostate cancer in untreated men[170,209,258] or in identifying recurrent disease in patients treated with definitive therapies (i.e. radiation therapy or radical prostatectomy).[45,269-272] However, some men, such as those taking 5α-reductase inhibitors (5-ARI), fall in-between these two categories. Five alpha-reductase inhibitors such as Finasteride or Dutasteride are marketed for management of prostate enlargement known as benign prostatic hyperplasia (BPH), a

condition that often contributes to the development of lower urinary tract symptoms in older men. BPH is extremely common. It affects 50% of men by the age of 50 and 90% of men in their 80s.[273] Fifty percent of men in their 60s experience low urinary tract symptoms due to BPH[274]. With growing numbers of men receiving mpMRI scans as part of the active surveillance protocol and with BPH being such a prevalent condition in older men, it is important to evaluate how the 5-ARIs affect the MR imaging and the interpretation of the imaging findings.

The health of the prostate is largely dependent on properly regulated actions of androgens through the androgen receptor (AR) complex.[275] Deregulation of the androgen–androgen receptor pathway plays an important role in the development and progression of prostate cancer.[276] The 5α-reductase enzymes convert testosterone, the most abundant circulating androgen, to dihydrotestosterone (DHT). Increased activity of 5α-reductase results in increased production of DHT. DHT has a greater affinity for the androgen receptor than testosterone and is a more effective activator of the AR. Once activated, the AR sets off a cascade of events resulting in increased cell growth and proliferation characteristic to both BPH and prostate cancer (Figure 7.1). One approach in regulating the AR pathway is to block the synthesis of DHT and by decreasing the levels of circulating androgens, limit the rates of AR activation and moderate cellular proliferation.[4]

MpMRI exams probe the prostate gland on a tissue level; diffusion weighted imaging is used to evaluate cell proliferation, while dynamic contrast enhanced imaging is used to assess neovascularity and tissue structure of the prostate. Since 5-ARIs impact prostatic tissues, the use of 5-ARI agents is expected to affect the interpretation of imaging studies in 5-ARI treated patients. In order to accurately stage and assess disease progression in 5-ARI treated patients, the effects of these agents on imaging studies in both benign and malignant prostatic tissues need to

be investigated. The purpose of this study was to determine whether 5-ARIs affect discrimination between low-grade prostate cancer and benign tissues on multiparametric MR imaging.

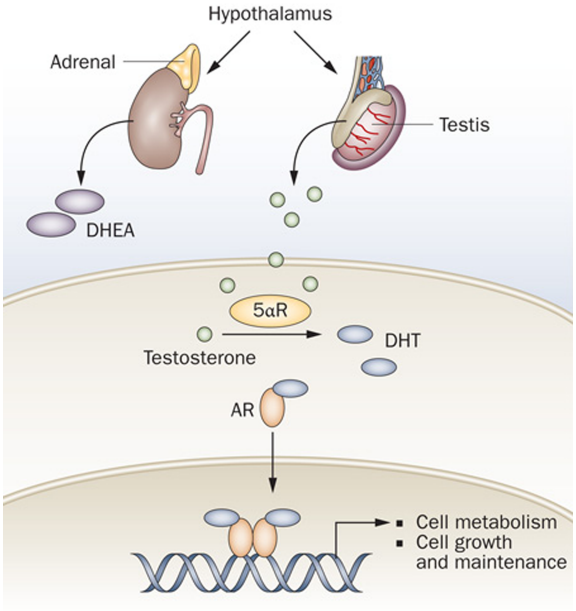

Figure 7.1: This figure demonstrates the diffusion of testosterone into the prostate cell. The testosterone is converted to DHT via 5α-reductase. DHT is then shown to bind to the androgen receptor (AR), leading to an increased cell metabolism and growth, often associated with benign prostatic hyperplasia, as well as prostate cancer[4].

The figure is adapted from Lucas P Nacusi and Donald J Rindall. Targeting 5α-reductase for prostate cancer prevention and treatment. Nat. Rev. Urol. 2011. May 31; 8(7):378-84.

7.3 Materials and Methods

7.3.1 Patients

This study was approved by the Committee on Human Research at this institution and was compliant with the Health Insurance Portability and Accountability Act. Written, informed consent was obtained from all subjects. Twenty patients with biopsy-proven Gleason Score 3+3 (GS3+3) prostate cancer were studied. Ten patients were taking 5-ARIs for at least a year at the time of the study. The ten 5-ARI treated patients were selected from 17 men who were scanned at our institution within the last 2 years, had complete mpMRI studies, were injected with gadopentetate dimeglumine (Gd-DTPA) contrast agent during DCE studies, had GS3+3 disease on biopsy and were taking either Dutasteride or Finasteride for at least a year. Out of these 17 patients, 1 patient was excluded due to a prior cryosurgery and another patient was excluded due

to a prior androgen deprivation hormonal therapy. Out of the remaining 15 men, 10 men had mpMRI visible cancers within the peripheral zone of the prostate as per their radiology report and were included in the study. Four out of ten men in the 5-ARI treated group were taking Dutasteride (0.5mg taken daily), while the remaining six were being treated with Finasteride (5mg taken daily). Ten untreated individuals with GS3+3 biopsy-proven peripheral zone cancers, scanned within the same 2-year period as the treated group, with complete mpMRI studies, Gd-DPTA injections during DCE, and with prostate volumes matched to the individuals in the 5-ARI treated group, were identified in the database and included in the study to serve as controls. Prostate volumes were matched to allow for similar central gland/peripheral zone ratios to facilitate comparable cancer detection. Cancer detection can be more challenging in patients with a significantly compressed peripheral zone due to an enlarged central grand. Prostate volumes were matched within 5cc as estimated on the MRI, except for the largest and the smallest prostates that were matched within 8.3cc and 5.5cc respectively. Despite the prostate volume matching, there are likely differences in the peripheral zone and the central gland volumes between the two groups.

Age, PSA values, the number of previous biopsy procedures, the number of biopsy cores obtained during the most recent biopsy procedure, and the number of days between the most recent biopsy and the MR exam, prostate volume, and benign and cancerous regions of interest (ROI) areas were compared between the two groups. The reported PSA values were obtained within a six-month window of the MRI scan.

7.3.2 MR Imaging

All patients were imaged with an expandable balloon endorectal coil (Medrad, Bayer HealthCare LLC, Whippany, NJ, USA) and a GE phased array on a 3T MR scanner (GE

Healthcare, Waukesha, WI, USA). The balloon coil was inflated with a perfluorocarbon fluid (Galden, Solvay Plastics, West Deptford, NJ, USA). T1-weighted images were examined as part of the clinical radiology review to ensure the biopsy hemorrhage was not corrupting the interpretation of the imaging study. T2-weighted images, diffusion-weighted images (DWI), and dynamic contrast-enhanced (DCE) MRI were acquired. The DCE MRI was performed using a single-dose of Gd-DPTA (Bayer HealthCare LLC, Whippany, NJ, USA) over ~5 minutes. Diffusion weighted imaging (DWI) was acquired using a 2D single-shot spin echo sequence with pixel bandwidth = 1952 (conventional acquisition, n=4: 2 (untreated) and 2 (5-ARI treated)), or pixel bandwidth = 1305 (reduced-field-of-view acquisition,[101] n=16: 8 (untreated) and 8 (5-ARI treated)), with b=0 and 600 s/mm^2, as well as b=0 and b=1350 s/mm^2 over 6 non-coplanar, non-colinear directions. The acquisition parameters are outlined in Table 7.1.

Table 7.1: Imaging parameters

Imaging	Pulse Sequence	TR/TE (ms)	FOV (cm)	Matrix Size	NEX	ST (mm)	In-Plane Res. (mm)	Temp. Res. (s)	b-value (s/mm^2)
T2w	FSE	6000/100	18x18	512x512	1	3	0.35x0.35	N/A	N/A
DCE	3D SPGR	3.5/0.9	26x26	256x256	0	3	1.02x1.02	10.417	N/A
Conv ADC	ss-EPI	4000/90	24x24	128x128	4	3	0.94x0.94	N/A	0, 600
rFOV ADC	ss-EPI	4000/90	18x9	128x64	6	3	0.70x0.70	N/A	0, 600
High-b DWI	ss-EPI	4000/100	24x24	256x256	5	3	0.94x0.94	N/A	0, 1350

FSE=Fast Spin Echo, SPGR = Spoiled Gradient Echo, ss-EPI = Single-Shot Echo-Planar Imaging, ST = Slice Thickness

T2-weighted and diffusion-weighted images were corrected for the reception profile of the endorectal and the pelvic phased-array coils using Prostate Analytical Coil Correction (PACC) software available on the GE scanners. This correction technique as described in the literature[67,277] has been adopted by GE. High quality of the intensity correction was visually confirmed. Apparent diffusion coefficient (ADC) maps were generated for DW b=0, 600 s/mm^2 images. In-house software was used to create the ADC maps. The maps were computed from the combined DWI (b=600 s/mm^2) and T2-weighted reference images (b=0 s/mm^2) using Eq. 7.1,

where b is the b-value used for the diffusion-weighted acquisition, S_{gm} is the geometric mean of the signal intensities acquired over the six gradient directions, and S_0 is the signal intensity of the T2-weighted image acquired without applying diffusion gradients.

$$\mathrm{ADC} = -\frac{1}{\mathrm{b}}\ln\left(\frac{S_{gm}}{S_0}\right) \qquad [7.1]$$

For b=0, 1350 s/mm^2 acquisition, diffusion-weighted images were corrected for the reception profile of the endorectal coil and a mean of the 6 directions was computed to create a high-b value DW image. For completeness, high-b ADC maps were computed for DWI b=0, 1350 s/mm^2 images using Eq. 7.1 and following the same procedure outlined above.

DCE maps were created based on the semi-quantitative tissue enhancement parameters of maximal enhancement slope, peak enhancement, and washout rate.[132] Additionally, pharmacokinetic modeling was performed using the mean signal intensity measurements within individual ROIs. Quantitative DCE parameters of the fractional extravascular, extracellular volume (v_{EES}), the transfer constant (K^{trans}), and the rate constant (K_{ep}) were computed. A widely used two-compartmental extended Tofts-Kermode model was applied since prostate tissue has relatively low permeability and this model is permeability, surface area-limited rather than flow-limited.[173] The concentration of Gd-DTPA in the blood plasma was modeled as a biexponential (Eq. 7.2)[222]

$$\mathrm{C_p} = \mathrm{AmpD}(\mathrm{a_1 e^{-m_1 t}} + \mathrm{a_2 e^{-m_2 t}}) \qquad [7.2]$$

where Amp=5.2, D = 0.1mmol/Kg of Gd-DTPA, a_1 = 3.99 kg/L, m_1 = 0.144 1/min, a_2 = 4.78 kg/L, m_2 = 0.011 1/min. A blood plasma fractional volume of 0.01 was used. The Amp was introduced to account for interpatient differences and was determined by minimizing the root-mean-square error (RMSE) of the fits.

For each subject, a single cancer ROI and a single benign ROI were drawn freeform

within the peripheral zone of each prostate on T2-weighted images, following areas of mpMRI concordance. Lesion placement was based upon agreement of biopsy and imaging findings. Benign ROIs were drawn contralateral to each cancerous region with care taken to avoid areas with positive biopsy findings. Additionally, locations for biopsy cores containing HGPIN or prostatitis were noted and avoided when placing benign regions of interest. All ROIs were drawn in the PZ. The ROIs were drawn without knowledge of the patients' treatment status. T2-weighted image intensity, ADC, high-b value DWI intensity, high-b ADC, maximal enhancement slope, peak enhancement, washout slope, v_{EES}, K^{trans}, and K_{ep} values were computed for each region of interest.

T2-weighted images and high-b value diffusion-weighted images are not measured on an absolute scale. For these measures, changes in gain may contribute additional variability across subjects. To account for this, contrast values between the cancerous and benign tissues were calculated based on Eq. 7.3.

$$\text{Contrast} = \frac{\text{MR}_{\text{Tumor}} - \text{MR}_{\text{Healthy}}}{\text{MR}_{\text{Healthy}}} \qquad [7.3]$$

Where "MR" represents the MR measure of interest, i.e. T2-weighted or high-b value DWI intensity.

7.3.3 Statistical Methods

Statistical analyses were carried out using JMP software (JMP, Version 12, SAS Institute Inc., Cary, NC). Measures are reported as mean ± standard deviation, with median (first quartile, third quartile), as well as minimum and maximum values also reported. Two-tailed, heteroscedastic Student's t-tests were used to compare age, PSA, prostate volume, as well as the sizes of benign and cancerous ROIs between the two groups, with $p \leq 0.05$ considered statistically significant. The number of biopsy procedures, the number of biopsy cores obtained during the

most recent biopsy, and the number of days since the most recent biopsy procedure were compared between the two groups using Mann-Whitney rank-sum test. Two-tailed, heteroscedastic Student's t-tests with a significance level of 0.05 were also used to compare MR measures in the untreated and the 5-ARI treated groups. Ordinal logistic regression analysis was performed for all imaging modalities to evaluate the area under the ROC (receiver operating characteristic) curve (AUC) in benign and cancerous regions for the untreated and the 5-ARI treated groups. A forward stepwise logistic regression with a threshold p-value of 0.1 was used to identify the imaging parameters for inclusion in the combined model. Finally, the coefficient of variation (COV) was evaluated for all imaging modalities for benign and cancerous regions in both the untreated and the 5-ARI treated groups.

7.4 Results

Patient characteristics for the untreated and the 5-ARI treated patients are summarized in Table 7.2 and 7.3 respectively. No significant differences were noted between the two groups. The untreated and the 5-ARI treated groups were similar in age (p=0.1), PSA (p=0.77), the number of previous biopsy procedures (p=0.81), the number of biopsy cores obtained during the most recent biopsy (p=0.85) and prostate volumes (p=0.90). Additionally, none of the subjects included in the analysis were noted to have post biopsy hemorrhage evident on imaging. The number of days between the most recent biopsy procedure and the MR exam was fewer in the untreated group (Table 7.2) than the 5-ARI treated group (Table 7.3); however, the difference between the two groups was not statistically significant p=0.27.

Table 7.2: Patient Characteristics: Untreated

	Untreated		
Metric	Mean±SD	Median (Q1, Q3)	Minimum, Maximum
Prostate Volume (matched) [cc]	48.66±29.6	41 (29.9, 51.1)	24.3, 123.3
Age [years]	64.4±6.6	72.0 (65.6, 76.6)	53.6, 76.4
PSA (within 6 months) [ng/ml]	6.55±3.76	5.93 (4.20, 8.05)	1, 14.1
# Previous Biopsy Procedures	2.1±0.99	2 (1, 3)	1, 4
# Biopsy Cores obtained during the most recent biopsy	15.3±3.0	15 (12, 18)	12, 21
Days between the most recent biopsy and mpMRI	455±326	476 (166, 556)	68, 1093
Size of benign ROIs [cm^2]	0.87±0.55	0.72 (0.54, 0.94)	0.33, 1.89
Size of cancerous ROIs [cm^2]	0.40±0.33	0.28 (0.20, 0.40)	0.11, 0.99

PSA=Prostate Specific Antigen, ROI = Region of Interest, SD = Standard Deviation.

Table 7.3: Patient Characteristics: 5-ARI Treated

	Treated		
Metric	Mean±SD	Median (Q1, Q3)	Minimum, Maximum
Prostate Volume (matched) [cc]	47.03±28.77	41.5 (29.5, 49.1)	18.8, 115
Age [years]	70.8±9.1	65.3 (60.0, 68.1)	57.4, 82.8
PSA (within 6 months) [ng/ml]	5.84±6.56	3.44 (1.90, 6.91)	1.2, 22.6
# Previous Biopsy Procedures	2.1±0.88	2 (1, 3)	1, 3
# Biopsy Cores obtained during the most recent biopsy	15.3±2.1	16 (13.5, 17)	12, 18
Days between the most recent biopsy and mpMRI	1140±1364	624 (351, 988)	220, 4604
Size of benign ROIs [cm^2]	0.62±0.33	0.56 (0.37, 0.65)	0.31, 0.91
Size of cancerous ROIs [cm^2]	0.32±0.26	0.26 (0.13, 0.46)	0.03, 0.84

PSA=Prostate Specific Antigen, ROI = Region of Interest, SD = Standard Deviation.

No statistically significant differences were noted between the sizes of the benign ROI areas for the untreated and the 5-ARI treated groups (p=0.24). Additionally, no statistically significant differences were noted between the sizes of the malignant ROI areas for the untreated and the 5-ARI treated groups (p=0.58). The two groups also had similar incidence of biopsy detected HGPIN and prostatitis. One patient in each group had a single HGPIN core discovered on biopsy. Additionally one patient in each group had biopsy- diagnosed prostatitis.

No significant differences between the untreated and the 5-ARI treated groups were noted for benign or cancerous regions on T2-weighted imaging, ADC, high-b value DWI intensity,

high-b ADC, maximal enhancement slope, peak enhancement, washout slope, or v_{EES}. No significant differences were noted for cancerous tissues between the untreated and the 5-ARI treated groups on K^{trans} and K_{ep} measures. However, significant differences were noted between benign untreated and benign treated tissues on K^{trans} ($p<0.02$) and K_{ep} ($p<0.03$). For benign tissues K^{trans} values were 0.42±0.234 min^{-1} and 0.20±0.09 min^{-1}, while K_{ep} values were 1.86±1.25 min^{-1} and 0.70±0.41 min^{-1} for the untreated and the 5-ARI treated groups respectively.

Example images for a patient with a low-grade biopsy-proven (GS3+3) prostate cancer with a PSA of 4.6 ng/ml are shown in the top row of Figure 7.2. The patient was not taking any medication for BPH or lower urinary tract symptoms. The bottom row in Figure 7.2 depicts example images for another patient with a biopsy-proven (GS3+3) prostate cancer with a PSA of 0.42 ng/ml who had been taking Dutasteride for the prior year. Based on visual assessment, Figure 7.2 demonstrates a better discrimination of benign and malignant tissues on the high-b value intensity images and the washout images in the treated case when compared to the untreated example.

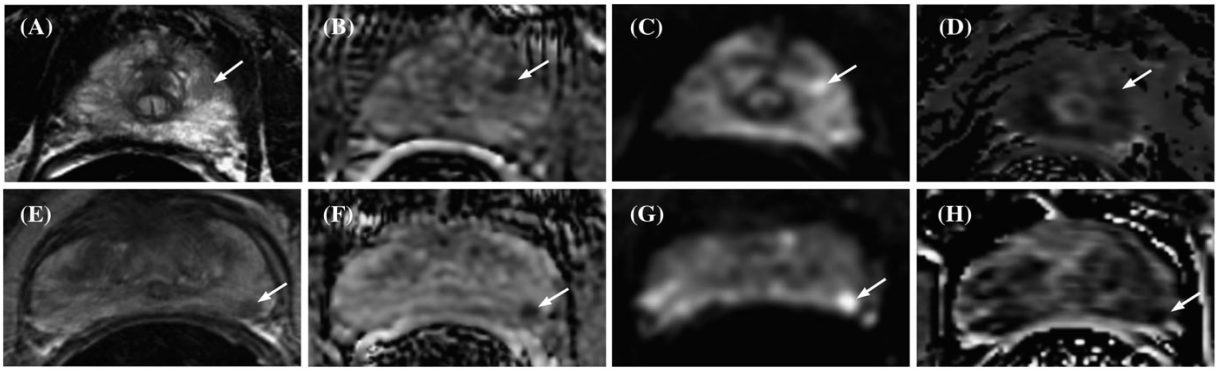

Figure 7.2: Example prostate MR images from a 67-year-old (GS3+3, PSA=4.6 ng/ml) untreated male (top panel: A-D) and from a 57-year-old man (GS3+3, PSA=0.42 ng/ml) treated with 5α-reductase inhibitors (bottom panel: E-H). T2w intensity images (A, E), ADC (B, F), high-b value DWI intensity (C, G), and washout slope (D, H) images are shown. The arrows designate cancerous regions.

Figure 7.3 depicts box-plots for the MR measures and calculated maps in benign and cancerous tissues as observed for the untreated men and the individuals treated with 5-ARIs. For

ADC, high-b value DWI intensity, high-b ADC, peak enhancement, maximal enhancement slope, washout slope, K^{trans}, and K_{ep} a better separation of benign and cancerous tissues was observed for individuals treated with 5-ARIs than for those untreated.

Table 7.4 lists ROC AUC values obtained when stepwise logistic regression was performed for all the imaging modalities for untreated and 5-ARI treated subjects in benign and cancerous regions. The ROC AUC values for distinguishing benign tissues from cancer were consistently higher in the treated group with the exception of T2-weighted images (AUC of 0.82 for the untreated and 0.79 for the 5-ARI treated group) and both sets of ADC images (untreated and 5-ARI treated groups both had an AUC of 1).

Table 7.4: ROC-AUC for cancerous versus benign tissues in untreated and 5-ARI treated patients. The higher AUC values are listed in **BOLD**.

Imaging	Untreated ROC-AUC	**Treated ROC-AUC**
T2-weighted	0.82	**0.79**
ADC (b=600 s/mm^2)	1	**1**
High-b ADC (b=1350 s/mm^2)	1	**1**
High-b DWI	0.71	**0.94**
Maximal Enhancement Slope	0.95	**1**
Washout Slope	0.78	**0.99**
Peak Enhancement	0.84	**0.93**
K^{trans}	0.9	**1**
K_{ep}	0.8	**0.98**
v_{EES}	0.51	**0.57**
Combined	0.86	**0.99**

The combined model used T2-weighted, ADC, maximal enhancement slope, washout slope, peak enhancement, K^{trans}, and K_{ep} for the untreated group and ADC, high-b DWI, maximal enhancement slope, washout slope, peak enhancement, K^{trans}, and K_{ep} for the treated group.

In order to account for the arbitrary intensity scales associated with T2w and high-b DWI, tumor contrast was evaluated. For the T2w, tumor contrast was computed to be 0.40±0.13 and 0.30±0.20 for the untreated and the 5-ARI treated groups, respectively, p=0.19. For high-b DWI intensity measures, contrast values were 0.61±0.43 and 0.99±0.52 for the untreated and the 5-ARI treated groups respectively, p=0.086.

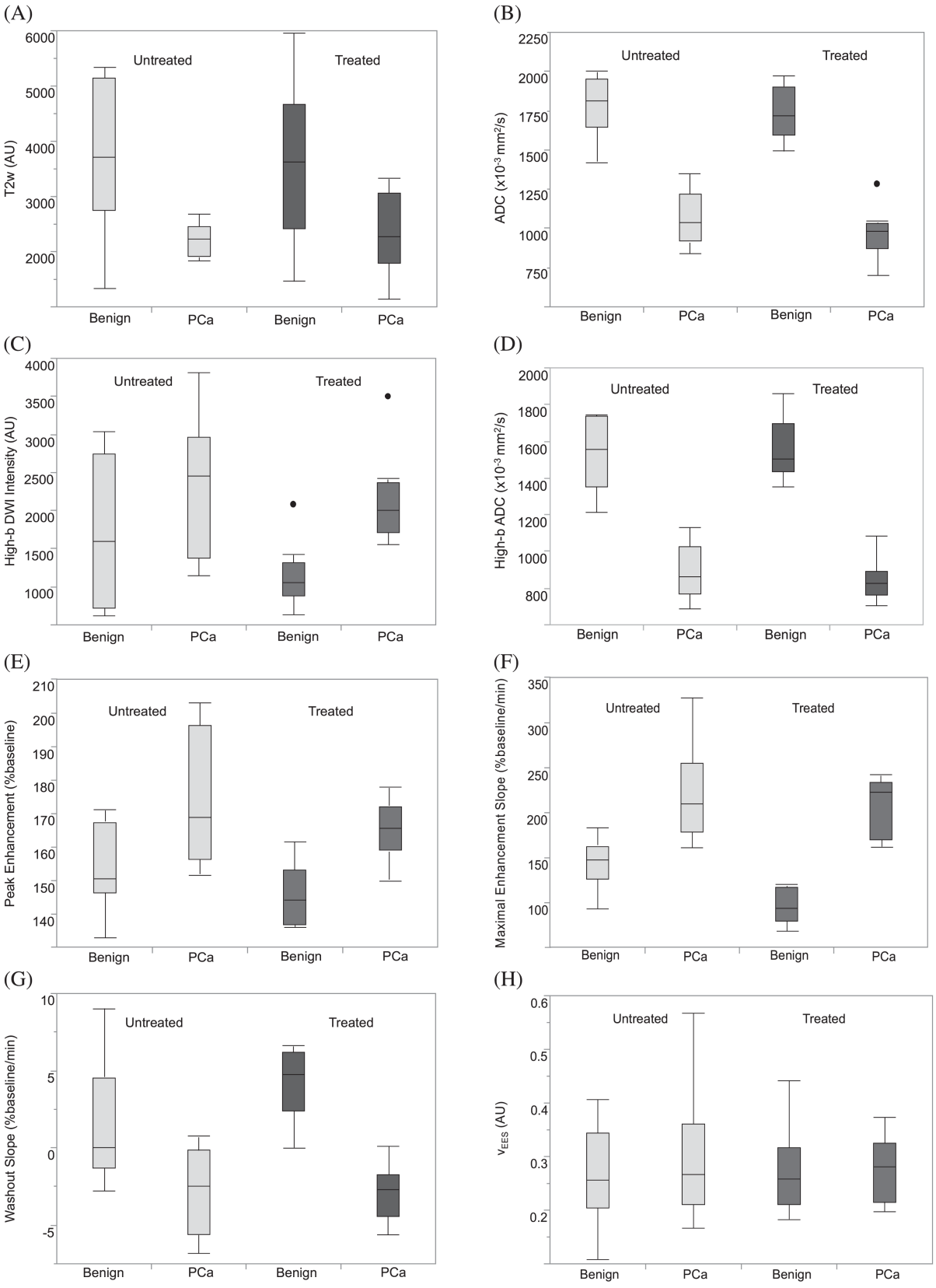
(A)
T2w (AU)
6000
5000
4000
3000
2000
Untreated
Treated
Benign
PCa
Benign
PCa
(B)
ADC (x10-3 mm2/s)
2250
2000
1750
1500
1250
1000
750
Untreated
Treated
Benign
PCa
Benign
PCa
(C)
High-b DWI Intensity (AU)
4000
3500
3000
2500
2000
1500
1000
Untreated
Treated
Benign
PCa
Benign
PCa
(D)
High-b ADC (x10-3 mm2/s)
2000
1800
1600
1400
1200
1000
800
Untreated
Treated
Benign
PCa
Benign
PCa
(E)
Peak Enhancement (%baseline)
210
200
190
180
170
160
150
140
Untreated
Treated
Benign
PCa
Benign
PCa
(F)
Maximal Enhancement Slope (%baseline/min)
350
300
250
200
150
100
Untreated
Treated
Benign
PCa
Benign
PCa
(G)
Washout Slope (%baseline/min)
10
5
0
-5
Untreated
Treated
Benign
PCa
Benign
PCa
(H)
vEES (AU)
0.6
0.5
0.4
0.3
0.2
Untreated
Treated
Benign
PCa
Benign
PCa

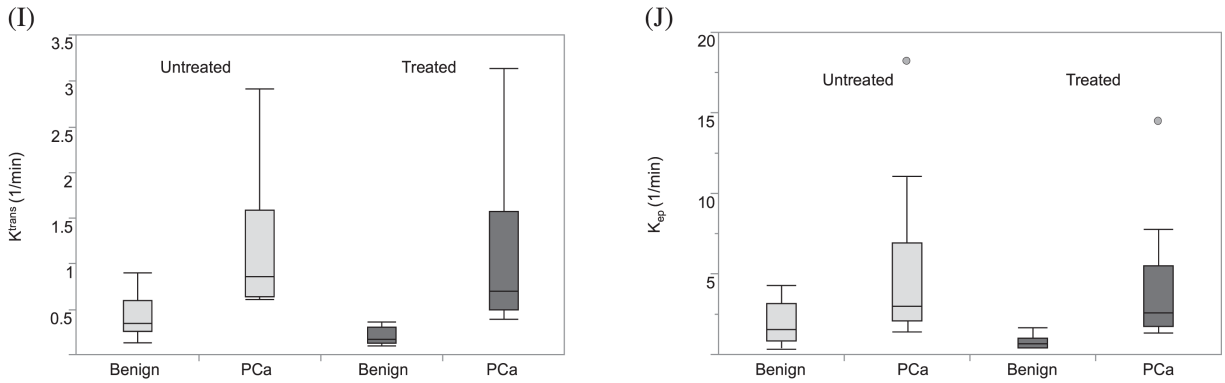

Figure 7.3: Box-plots comparing A) T2w intensity, B) ADC (b=600 s/mm^2), C) high-b value DWI intensity, D) high-b ADC (b=1350 s/mm^2), E) peak enhancement, F) maximal enhancement slope, G) washout slope, H) v_{EES}, I) K^{trans}, and J) K_{ep} values in cancerous and benign prostatic tissues for untreated individuals and those treated with 5α-reductase inhibitors. Horizontal lines within the box plots represent the median values. Whiskers are drawn to the furthest points within 1.5x interquartile range, where interquartile range is the difference between the 1st and the 3rd quartiles.

The absolute coefficients of variation for the measures within the benign tissues and within the cancer are listed in Table 7.5. COV values were lower in both the benign tissues and the cancer for the treated group compared to the untreated group for high-b value DW images, high-b ADC, peak enhancement, washout slope, v_{EES}, K_{ep}, and maximal enhancement slope (cancer only), ADC and K^{trans} (benign only).

Table 7.5: Absolute coefficient of variation of the measures within cancer and benign tissues for the treated and untreated groups. The lower COV values are listed in **BOLD**.

Imaging	Benign		Cancer	
	Untreated	**Treated**	**Untreated**	**Treated**
T2-weighted	**0.34**	0.389	**0.233**	0.303
ADC (b=600 s/mm^2)	0.107	**0.095**	**0.153**	0.174
High-b ADC (b=1350 s/mm^2)	0.13	**0.103**	0.16	**0.13**
High-b DWI	0.567	**0.361**	0.367	**0.264**
Maximal Enhancement Slope	**0.185**	0.204	0.24	**0.153**
Washout Slope	2.556	**0.572**	0.968	**0.611**
Peak Enhancement	0.082	**0.064**	0.113	**0.052**
K^{trans}	0.556	**0.451**	**0.749**	0.83
K_{ep}	0.674	**0.52**	1.05	**0.965**
v_{EES}	0.353	**0.289**	0.394	**0.212**

7.5 Discussion

Dutasteride and Finasteride are two commonly used drugs prescribed for treatment of prostate enlargement. Both agents act as inhibitors to the 5α-reductase enzyme, forming strong irreversible ternary complexes with the 5α-reductase–NADPH complex.[278] In a 2011, multicenter, randomized, double-blind, 12 month-long study of 1630 men, Nickel *et al.* reported that both Dutasteride and Finasteride were effective at reducing prostate volume with no significant difference between the two treatments during the study and with a similar number of adverse events.[279]

This study investigated whether 5-ARIs affect discrimination between low-grade prostate cancer and benign tissues on mpMRI. It was observed that high-b value DWI intensity, maximal enhancement slope, peak enhancement, washout slope, K^{trans}, and K_{ep} acquired as part of a routine prostate mpMRI scan show reduced variability within both low-grade (GS3+3) cancerous tissues and within benign tissues in the treated group. Additionally, a better separation between cancerous and benign regions was noted for the prostate tissues exposed to 5-ARI as compared to the untreated prostate tissues. These results are consistent with the findings of an earlier study that monitored the effects of Dutasteride on untreated prostate cancer using MRI and magnetic resonance spectroscopic imaging (MRSI).[280] The authors reported that in tumors the levels of the metabolite choline, the presence of which signals malignancy, remained unchanged with 5-ARI treatments. However, in benign prostatic tissues, 5-ARI treatments resulted in decreased levels of the prostatic secretory metabolites citrate and polyamines, low levels of which are consistent with 5-ARIs primarily inhibiting metabolism of healthy prostatic glandular tissues and eventually inducing atrophy of these tissues.[280] The reduction of the dominant normal prostatic metabolite MR resonances increases the visibility of the cancerous metabolite signals, elevated

choline to citrate ratio, and therefore the detection of small amounts of cancer.[280] By blocking the AR pathway, 5-ARIs block DHT driven proliferation and vascularization of prostatic tissues, inducing apoptosis and resulting in increased amounts of tissue atrophy. When exposed to 5-ARI therapy, androgen sensitive glandular normal and BPH tissues quickly atrophy, while less androgen sensitive cancers will atrophy more slowly.[281] Based upon this biology and our results, we suggest that 5-ARI therapy results in decreased contribution of glandular tissues to all MR measurements and allows cancerous tissues to become readily apparent against a more uniform background of atrophic tissues.

Untreated benign and 5-ARI treated benign prostatic tissues have different appearances on histopathological examination. Histologically, atrophy is characterized by a reduction in the volume of existing glands and the loss of luminal secretary epithelial cells.[282] Large pools of lumen are observed for healthy untreated prostatic tissues, while significantly diminished luminal spaces and increased surfaces of stromal tissues are typically seen in the treated individuals. Additionally, the shrinking and loss of the basal and the secretory epithelial cells associated with atrophy is often noted in the treated prostatic tissues.

Figure 7.4 shows an example of T2-weighted images for benign tissues for two untreated and one 5-ARI treated patients. Figure 7.4a demonstrates the appearance of healthy glandular tissues in an untreated patient; detecting cancerous lesions against such a uniform and bright background is straightforward. Unfortunately, very few prostates have such an uncomplicated, glandular appearance. Figure 7.4b demonstrates the challenges associated with detecting cancers within mixed tissues, characteristic of the majority of prostates. Against a background of such heterogeneous tissues – some glandular and bright, some stromal and dark, some atrophic, some inflamed, and some malignant - it is much more challenging to confidently identify cancerous

regions in this untreated patient. Figure 7.4c shows why atrophic processes associated with 5-ARI treatments may enhance the diagnostic utility of mpMRI. While the 5-ARI treated prostatic

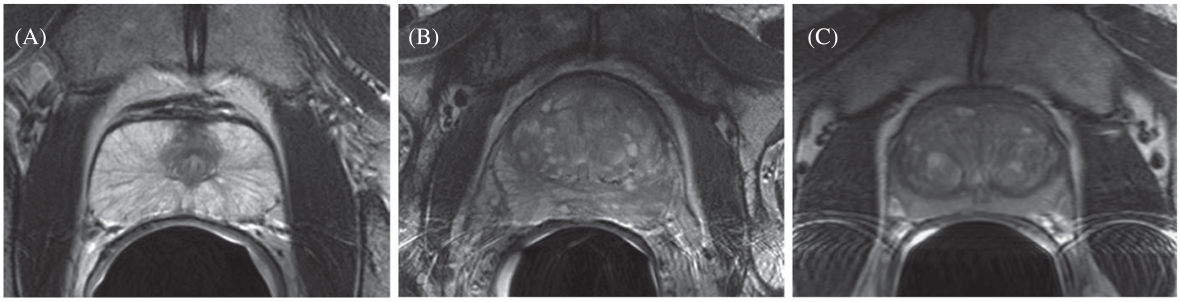

Figure 7.4: T2-weighted images of benign prostatic tissues for A) untreated patient with homogeneous tissue (age = 64.1 years, PSA= 2.14 ng/ml, GS3+3), B) untreated patient with heterogeneous tissue (71.4 years, 5 ng/ml, GS3+3), C) 5-ARI treated patient with homogeneous tissue (50.4 years, 4.44 ng/ml, GS3+3).

tissues of the peripheral zone appear darker than those observed in healthy, untreated tissues (Figure 7.4a), the diffuse nature of the hormone-induced atrophy allows for a more uniform background than the mix of tissues often seen in untreated prostates (Figure 7.4b). The uniformity of the benign prostatic tissues provides a better background against which a malignant lesion can be detected. This may explain why we observe a better separation between benign and malignant tissues and a lower variability in the measures for 5-ARI treated group when compared to untreated controls.

Within the scope of anti-androgen therapies, very few studies review the effects of 5-ARI agents on imaging.[280] For instance, Dutasteride treatment was shown to increase the rate of cancer detection in ultrasound studies.[283-285] However, in the realm of MR imaging, most of the published literature involving 5-ARI agents focuses on the changes in prostate volumes due to androgen deprivation.[286,287] There are, however, studies covering the effects of hormone ablation on both anatomical and functional prostate MR imaging.[47,48,288-291] There is a consensus that glandular atrophy and tissue shrinkage makes prostate cancer detection more challenging on T2-weighted images.[48,291,292] This is a similar observation to what is seen for T2-weighted images in

the 5-ARI treated cases of the current study. For functional imaging, preliminary studies have shown cancerous lesions becoming less apparent on DWI and DCE post-hormonal ablation, which is different than the results of the current study.[47,290] This discrepancy is likely due to the differences in the evaluated populations. Hormonal ablation is typically used to treat aggressive prostate cancer rather than GS3+3 disease (pooling the patients from the two ablation studies - only 4/69 men had GS3+3 prostate cancers),[47,290] which is vastly different from our exclusively low-risk GS3+3 cohort. Pretreatment discrimination of cancer and benign tissues is easier in patients with aggressive prostate cancer as opposed to those with low-risk disease. Thus, inhomogeneity of prostatic tissues plays a small role in identifying aggressive, clear-cut cancers, but is a significant hurdle in diagnosing diffuse or low-grade lesions. For low-risk cancers, as our data suggests, post-treatment cancer detection might be advantaged by the atrophy of benign tissues, especially when considering the challenges of low-risk cancer detection pre-treatment. On the other hand, atrophy of benign glandular tissues post-treatment might make it more challenging to detect aggressive cancers when compared to the ease of detection pre-treatment as suggested by the prior studies of hormone ablation in aggressive cancer.[47,290]

In the current study, while it was noted that the contrast on T2-weighted images between cancerous and benign tissues was lower in the 5-ARI treated than the untreated group, our findings for the functional imaging measures provide reassurance. First, contrast on the high-b value DW images between cancerous and malignant tissues was higher in the 5-ARI treated than the untreated group. Second, the separation between imaging values for cancerous and benign regions was greater on ADC, high-b value DW, maximal enhancement slope, peak enhancement, washout slope, K^{trans}, and K_{ep} images, with an overall reduced variability in the MR measures for individuals in the 5-ARI group. Third, K_{ep} and K^{trans} values obtained for benign regions were

significantly lower for the 5-ARI treated than the untreated groups. Higher K_{ep} and K^{trans} values typically signal higher perfusion and are often indicative of malignancy. Since there were no significant differences between K_{ep} and K^{trans} values for the cancerous 5-ARI treated and untreated groups, the larger separation between cancerous and benign tissues in the treated group may potentially lead to an easier detection of cancerous regions in that cohort.

For patients on active surveillance with emphasis placed on detecting and treating more aggressive disease, why do we care about detecting GS3+3 lesions? Several studies reported that patients with visible lesions on mpMRI have an increased overall risk of cancer progression;[293,294] therefore, identifying these lesions is of clinical importance. If pretreatment with 5-ARI agents makes lesions more conspicuous on imaging, it may aid in identifying patients at a higher risk of cancer progression, prompting a closer observation of these patients while on active surveillance. Additionally, while our study looked at GS3+3 disease in 5-ARI treated and untreated men, we expect our findings to be applicable in detection of higher-grade cancer (i.e. GS3+4 or GS4+3 disease), the detection of which is of clinical significance. In this study, we limited the inclusion criteria to GS3+3 lesions in order to avoid introducing variability associated with Gleason 4 disease, especially when detected on biopsy; however, we expect the underlying principle of elucidating cancer against a more homogeneous atrophic background to be applicable for higher grade cancers. This observation that pretreatment with 5-ARI agents improves PCa detection on mpMRI is very similar to the reported effects of 5-ARI agents on the sensitivity of PSA in detecting prostate cancer in 5-ARI treated individuals. In a large study of 18,882 men, Thompson *et al.* reported that PSA had a better sensitivity for detecting all grades of prostate cancer in the group treated with Finasteride when compared to a placebo cohort.[295] This further supports the idea that reducing the impact of potential confounders such as benign

pathologies improves cancer detection in the prostate.

Another potentially important consequence of our findings pertains to interpretation of mpMR imaging studies acquired in 5-ARI treated patients when using Prostate Imaging – Reporting and Data System (PI-RADS) criteria. For peripheral zone lesions, PI-RADS places a particular importance on conspicuity of prostatic lesions on diffusion-weighted imaging.[296] Our results suggest that 5-ARI treated patients will have prostate cancers that are more conspicuous on functional imaging than lesions of similar grade in the untreated group. This can potentially lead to a misdiagnosis of higher-grade cancer in men with GS3+3 disease, affecting the disease management for those patients. Knowledge of a patient's 5-ARI status prior to interpretation of his imaging study might be an important caveat when applying PI-RADS criteria.

Our study had several limitations. First, with only 10 patients per group our study has a small sample size. Second, biopsy-based Gleason grading of cancerous regions was used, which could be inaccurate due to biopsy sampling errors.[256,257] Third, only men with visible lesions on mpMRI were included in our study, which introduces a selection bias to our sample. However, this selection bias adds clinical significance to our findings. Men with lesions visible on mpMRI have been shown to have an increased risk of cancer progression; therefore, detecting these lesions in 5-ARI treated individuals is important for disease management in this population. Fourth, benign regions were drawn based on imaging (contralateral to cancer); they could potentially include inflammation or even cancer undetected on biopsy. Fifth, T2w measures were reported for completeness; however, these measures are inherently biased since the ROIs were drawn on T2w images, with the size of the lesion providing further bias. Additionally, while untreated patients were matched to the treated individuals and were not significantly different in the demographic, clinical, and biopsy metrics tested, there could be unaccounted for differences

between the two subject groups. For purposes of completeness we are reporting both semi-quantitative parameters, as well as measures derived using quantitative pharmacokinetic modeling. It is important to remember that these measures are not independent but may be attributed to similar biological mechanisms. Similarly, there is a redundancy to ADC (b=600 s/mm^2) and high-b ADC (b=1350 s/mm^2) maps, with the two sets of data representing the same biological processes but at slightly different levels of tissue organization. Finally, patients were treated with either Finasteride (type I 5-ARI) or Dutasteride (type I and II 5-ARI). Differences between the two agents may introduce variability to the data. However, despite these limitations, for the majority of the imaging modalities, we were still able to see reduced coefficients of variation and better discrimination between cancerous and benign tissues in the treated patients as compared to the untreated patients.

In conclusion, this study presented data from 5-ARI treated and untreated men receiving 3T multiparametric MRI scans. A better separation between low-grade cancerous and benign regions was observed for prostatic tissues exposed to 5-ARIs for the majority of the MR measures of interest and overall with an mpMRI approach. Furthermore, a reduction in the coefficient of variation was noted for most of the MR measures in the treated cohort (for both cancerous and benign regions) when compared to the untreated group. The findings in our study suggest that pretreatment with 5-ARI may facilitate a better discrimination of low-grade prostate cancer from benign tissues with mpMRI. Furthermore, this study suggests that interpretation of mpMRI in treated patients may need to be refined, as both more high-risk lesions may be identified and as low-risk lesions may be misdiagnosed as more aggressive. These findings are of clinical importance and require further exploration in a larger cohort.

CHAPTER 8

Conclusion

8.1 Summary of Results

This thesis reviewed the imaging modalities involved in multiparametric MR scans. It discussed the importance of a proper registration and alignment of histopathology slides, which often serve as a reference standard for imaging studies, to the MR images and proposed a semi-automatic registration technique. By closely correlating mpMRI data to histopathology, we characterized the appearance of cancerous tissues on imaging and used mpMRI to predict PCa aggressiveness by creating robust logistic regression models to discriminate benign tissues from PCa, distinguish ≤GS3+3 cancers from clinically significant disease (≥SG3+4), and differentiate low-risk cancers (≤GS3+4) from high-risk cancers (≥GS4+3) within both the peripheral and the transition zones. We also introduced a new semi-automatic technique for segmentation and assessment of cancerous regions outlined on histopathology. This approach was used to characterize all cancerous regions found on histopathology in a post radical prostatectomy cohort of 78 men. Of particular import, sparse lesions, which are poorly studied, were thoroughly characterized not only on histopathology but also on mpMR imaging. Sparse lesions were shown to be predominantly low-grade and thus overall likely to pose limited malignant potential for spread and progression. On imaging, sparse low-grade cancers and sparse higher-grade disease were shown to have similar imaging characteristics to dense low-grade PCa. However, high-grade, aggressive sparse lesions were clearly detectable on mpMRI. Finally, we covered the effect of PCa treatments on prostatic tissues and their appearance on imaging. Specifically, we looked at 5-ARIs (used to slow down and reverse BPH growth) and showed in a small-cohort

study that pretreatment with 5-ARI may facilitate a better discrimination of low-grade prostate cancer from benign tissues with mpMRI.

8.2 Future Directions

Over the past decade mpMRI has been gaining traction as a reasonable alternative for detection and characterization of prostatic lesions.[40,170,258,297,298] By assessing the prostate gland in its entirety, mpMRI offers a better diagnostic approach than the traditional ultrasound guided systematic biopsies, which are plagued with undersampling and undergrading.[256,257] However, histological assessment still remains the most trusted way of assessing PCa. MR-guided and US-MR fusion prostate biopsies provide a direct approach to not only target a dominant lesion but also sample the region with the most aggressive appearing tumor. Preliminary studies found MR-guided prostate biopsies useful in diagnosing a new malignancy or upgrading previously diagnosed disease.[125,299,300] Furthermore, a study by Siddiqui *et al*. reported an increased detection of high-risk (≥G4+3) prostate cancer and decreased detection of low-risk prostate cancer for MR-US fusion biopsies when compared to standard US-guided biopsies.[35,301] Prostate biopsies aided by MR-guidance can potentially increase the diagnosis of clinically significant malignancies, addressing the concerns associated with traditional untargeted US-guided biopsies. mpMRI may also aid in treatment management of prostate cancer.

Furthermore, the ability of mpMRI to localize a prostatic lesion allows the implementation of focal treatments, which could potentially reduce the side effects associated with radical interventions.[302] High-intensity focused ultrasound (HIFU) is one such example. HIFU is a minimally invasive technique that has been used under MR guidance, with MR thermometry in real time to monitor ablation of a localized cancerous region without affecting the entire gland.[303] Preliminary studies report promising results in treatment of small, low to

intermediate grade prostatic lesions.[304,305] Overall, multiparametric MRI has the potential to have a significant impact on the way the prostate cancer is diagnosed and treated. Standardization of acquisition protocols is required to achieve the optimal reproducibility of imaging findings and establish trust. With PSA testing on the decline, based on the USPSTF recommendation,[19] mpMRI may prove the ultimate tool for non-invasive PCa assessment and an apt aid for more accurate prostatic biopsies.

Bibliography

1. De Marzo AM, Platz EA, Sutcliffe S, et al. Inflammation in prostate carcinogenesis. *Nature reviews Cancer.* 2007;7(4):256-269.
2. Crane JC, Olson MP, Nelson SJ. SIVIC: Open-Source, Standards-Based Software for DICOM MR Spectroscopy Workflows. *International journal of biomedical imaging.* 2013;2013:169526.
3. Siegel RL, Miller KD, Jemal A. Cancer Statistics, 2017. *CA: a cancer journal for clinicians.* 2017;67(1):7-30.
4. Nacusi LP, Tindall DJ. Targeting 5alpha-reductase for prostate cancer prevention and treatment. *Nature reviews Urology.* 2011;8(7):378-384.
5. Wilt TJ, MacDonald R, Rutks I, et al. Systematic review: comparative effectiveness and harms of treatments for clinically localized prostate cancer. *Annals of internal medicine.* 2008;148(6):435-448.
6. Xu CY, Prince JL. Snakes, shapes, and gradient vector flow. *Ieee T Image Process.* 1998;7(3):359-369.
7. Klotz L, Vesprini D, Sethukavalan P, et al. Long-term follow-up of a large active surveillance cohort of patients with prostate cancer. *Journal of clinical oncology : official journal of the American Society of Clinical Oncology.* 2015;33(3):272-277.
8. Tosoian JJ, Mamawala M, Epstein JI, et al. Intermediate and Longer-Term Outcomes From a Prospective Active-Surveillance Program for Favorable-Risk Prostate Cancer. *Journal of clinical oncology : official journal of the American Society of Clinical Oncology.* 2015;33(30):3379-3385.

9. Bellardita L, Valdagni R, van den Bergh R, et al. How Does Active Surveillance for Prostate Cancer Affect Quality of Life? A Systematic Review. *Eur Urol.* 2015;67(4):637-645.

10. Jeldres C, Cullen J, Hurwitz LM, et al. Prospective quality-of-life outcomes for low-risk prostate cancer: Active surveillance versus radical prostatectomy. *Cancer-Am Cancer Soc.* 2015;121(14):2465-2473.

11. Humphrey PA. Gleason grading and prognostic factors in carcinoma of the prostate. *Modern pathology : an official journal of the United States and Canadian Academy of Pathology, Inc.* 2004;17(3):292-306.

12. Gleason DF. Classification of prostatic carcinomas. *Cancer chemotherapy reports.* 1966;50(3):125-128.

13. Maurice MJ, Abouassaly R, Kim SP, et al. Contemporary Nationwide Patterns of Active Surveillance Use for Prostate Cancer. *Jama Intern Med.* 2015;175(9):1569-1571.

14. Heidegger I, Skradski V, Steiner E, et al. High risk of under-grading and -staging in prostate cancer patients eligible for active surveillance. *PloS one.* 2015;10(2):e0115537.

15. Brawley OW. Trends in prostate cancer in the United States. *Journal of the National Cancer Institute Monographs.* 2012;2012(45):152-156.

16. Etzioni R, Gulati R, Tsodikov A, et al. The prostate cancer conundrum revisited: treatment changes and prostate cancer mortality declines. *Cancer-Am Cancer Soc.* 2012;118(23):5955-5963.

17. Loeb S, Bjurlin MA, Nicholson J, et al. Overdiagnosis and overtreatment of prostate cancer. *Eur Urol.* 2014;65(6):1046-1055.

18. Schroder FH, Hugosson J, Roobol MJ, et al. Screening and prostate-cancer mortality in a randomized European study. *The New England journal of medicine.* 2009;360(13):1320-1328.

19. Moyer VA, Force USPST. Screening for prostate cancer: U.S. Preventive Services Task Force recommendation statement. *Annals of internal medicine.* 2012;157(2):120-134.

20. McNeal JE. Normal histology of the prostate. *The American journal of surgical pathology.* 1988;12(8):619-633.

21. Akin O, Sala E, Moskowitz CS, et al. Transition zone prostate cancers: features, detection, localization, and staging at endorectal MR imaging. *Radiology.* 2006;239(3):784-792.

22. Bostwick DG, Liu L, Brawer MK, et al. High-grade prostatic intraepithelial neoplasia. *Reviews in urology.* 2004;6(4):171-179.

23. Nadler RB, Humphrey PA, Smith DS, et al. Effect of inflammation and benign prostatic hyperplasia on elevated serum prostate specific antigen levels. *The Journal of urology.* 1995;154(2 Pt 1):407-413.

24. Bozeman CB, Carver BS, Eastham JA, et al. Treatment of chronic prostatitis lowers serum prostate specific antigen. *The Journal of urology.* 2002;167(4):1723-1726.

25. Billis A, Meirelles LR, Magna LA, et al. Extent of prostatic atrophy in needle biopsies and serum PSA levels: is there an association? *Urology.* 2007;69(5):927-930.

26. Lilja H, Ulmert D, Vickers AJ. Prostate-specific antigen and prostate cancer: prediction, detection and monitoring. *Nature reviews Cancer.* 2008;8(4):268-278.

27. Cui T, Kovell RC, Terlecki RP. Is it time to abandon the digital rectal examination? Lessons from the PLCO Cancer Screening Trial and peer-reviewed literature. *Current medical research and opinion.* 2016:1-7.

28. Epstein JI, Partin AW, Sauvageot J, et al. Prediction of progression following radical prostatectomy. A multivariate analysis of 721 men with long-term follow-up. *The American journal of surgical pathology.* 1996;20(3):286-292.

29. Aubry W, Lieberthal R, Willis A, et al. Budget impact model: epigenetic assay can help avoid unnecessary repeated prostate biopsies and reduce healthcare spending. *American health & drug benefits.* 2013;6(1):15-24.

30. Wilson SS, Crawford ED. Screening for prostate cancer. *Clin Prostate Cancer.* 2004;3(1):21-25.

31. Gleason DF. Histologic grading of prostate cancer: a perspective. *Human pathology.* 1992;23(3):273-279.

32. Serefoglu EC, Altinova S, Ugras NS, et al. How reliable is 12-core prostate biopsy procedure in the detection of prostate cancer? *Cuaj-Can Urol Assoc.* 2013;7(5-6):E293-E298.

33. Loeb S, Carter HB, Berndt SI, et al. Complications After Prostate Biopsy: Data From SEER-Medicare. *J Urology.* 2011;186(5):1830-1834.

34. Gulati R, Gore JL, Etzioni R. Comparative effectiveness of alternative prostate-specific antigen--based prostate cancer screening strategies: model estimates of potential benefits and harms. *Annals of internal medicine.* 2013;158(3):145-153.

35. Siddiqui MM, Rais-Bahrami S, Turkbey B, et al. Comparison of MR/ultrasound fusion-guided biopsy with ultrasound-guided biopsy for the diagnosis of prostate cancer. *Jama.* 2015;313(4):390-397.

36. Barentsz JO, Richenberg J, Clements R, et al. ESUR prostate MR guidelines 2012. *European radiology.* 2012;22(4):746-757.

37. Dickinson L, Ahmed HU, Allen C, et al. Scoring systems used for the interpretation and reporting of multiparametric MRI for prostate cancer detection, localization, and characterization: could standardization lead to improved utilization of imaging within the diagnostic pathway? *Journal of magnetic resonance imaging : JMRI.* 2013;37(1):48-58.

38. Fenner A. Prostate cancer: multiparametric MRI scans could be a useful adjunct for active surveillance in prostate cancer. *Nature reviews Urology.* 2013;10(5):247.

39. Hoeks CM, Barentsz JO, Hambrock T, et al. Prostate cancer: multiparametric MR imaging for detection, localization, and staging. *Radiology.* 2011;261(1):46-66.

40. Johnson LM, Turkbey B, Figg WD, et al. Multiparametric MRI in prostate cancer management. *Nature reviews Clinical oncology.* 2014;11(6):346-353.

41. Kurhanewicz J, Vigneron D, Carroll P, et al. Multiparametric magnetic resonance imaging in prostate cancer: present and future. *Current opinion in urology.* 2008;18(1):71-77.

42. Sandler K, Patel M, Lynne C, et al. Multiparametric-MRI and Targeted Biopsies in the Management of Prostate Cancer Patients on Active Surveillance. *Frontiers in oncology.* 2015;5:4.

43. Rouviere O. Imaging techniques for local recurrence of prostate cancer: for whom, why and how? *Diagnostic and interventional imaging.* 2012;93(4):279-290.

44. Kim CK, Park BK, Lee HM. Prediction of locally recurrent prostate cancer after radiation therapy: incremental value of 3T diffusion-weighted MRI. *Journal of magnetic resonance imaging : JMRI.* 2009;29(2):391-397.

45. Westphalen AC, Reed GD, Vinh PP, et al. Multiparametric 3T endorectal mri after external beam radiation therapy for prostate cancer. *Journal of magnetic resonance imaging : JMRI.* 2012;36(2):430-437.

46. Bubley GJ, Bloch BN, Vazquez C, et al. Accuracy of endorectal magnetic resonance/transrectal ultrasound fusion for detection of prostate cancer during brachytherapy. *Urology.* 2013;81(6):1284-1289.

47. Barrett T, Gill AB, Kataoka MY, et al. DCE and DW MRI in monitoring response to androgen deprivation therapy in patients with prostate cancer: a feasibility study. *Magnetic resonance in medicine.* 2012;67(3):778-785.

48. Chen M, Hricak H, Kalbhen CL, et al. Hormonal ablation of prostatic cancer: effects on prostate morphology, tumor detection, and staging by endorectal coil MR imaging. *AJR American journal of roentgenology.* 1996;166(5):1157-1163.

49. Miralbell R, Vees H, Lozano J, et al. Endorectal MRI assessment of local relapse after surgery for prostate cancer: A model to define treatment field guidelines for adjuvant radiotherapy in patients at high risk for local failure. *International journal of radiation oncology, biology, physics.* 2007;67(2):356-361.

50. Pucar D, Sella T, Schoder H. The role of imaging in the detection of prostate cancer local recurrence after radiation therapy and surgery. *Current opinion in urology.* 2008;18(1):87-97.

51. Charnley N, Morgan A, Thomas E, et al. The use of CT-MR image registration to define target volumes in pelvic radiotherapy in the presence of bilateral hip replacements. *The British journal of radiology.* 2005;78(931):634-636.

52. Rosewall T, Kong V, Vesprini D, et al. Prostate delineation using CT and MRI for radiotherapy patients with bilateral hip prostheses. *Radiotherapy and oncology : journal of the European Society for Therapeutic Radiology and Oncology.* 2009;90(3):325-330.

53. Rudisch A, Kremser C, Peer S, et al. Metallic artifacts in magnetic resonance imaging of patients with spinal fusion. A comparison of implant materials and imaging sequences. *Spine.* 1998;23(6):692-699.

54. Delongchamps NB, Beuvon F, Eiss D, et al. Multiparametric MRI is helpful to predict tumor focality, stage, and size in patients diagnosed with unilateral low-risk prostate cancer. *Prostate cancer and prostatic diseases.* 2011;14(3):232-237.

55. Delongchamps NB, Rouanne M, Flam T, et al. Multiparametric magnetic resonance imaging for the detection and localization of prostate cancer: combination of T2-weighted, dynamic contrast-enhanced and diffusion-weighted imaging. *BJU international.* 2011;107(9):1411-1418.

56. Franiel T, Stephan C, Erbersdobler A, et al. Areas suspicious for prostate cancer: MR-guided biopsy in patients with at least one transrectal US-guided biopsy with a

negative finding--multiparametric MR imaging for detection and biopsy planning. *Radiology.* 2011;259(1):162-172.

57. Futterer JJ, Heijmink SW, Scheenen TW, et al. Prostate cancer localization with dynamic contrast-enhanced MR imaging and proton MR spectroscopic imaging. *Radiology.* 2006;241(2):449-458.

58. Haider MA, van der Kwast TH, Tanguay J, et al. Combined T2-weighted and diffusion-weighted MRI for localization of prostate cancer. *AJR American journal of roentgenology.* 2007;189(2):323-328.

59. Langer DL, van der Kwast TH, Evans AJ, et al. Prostate tissue composition and MR measurements: investigating the relationships between ADC, T2, K(trans), v(e), and corresponding histologic features. *Radiology.* 2010;255(2):485-494.

60. Langer DL, van der Kwast TH, Evans AJ, et al. Prostate cancer detection with multi-parametric MRI: logistic regression analysis of quantitative T2, diffusion-weighted imaging, and dynamic contrast-enhanced MRI. *J Magn Reson Imaging.* 2009;30(2):327-334.

61. Mazaheri Y, Hricak H, Fine SW, et al. Prostate tumor volume measurement with combined T2-weighted imaging and diffusion-weighted MR: correlation with pathologic tumor volume. *Radiology.* 2009;252(2):449-457.

62. Weinreb JC, Blume JD, Coakley FV, et al. Prostate cancer: sextant localization at MR imaging and MR spectroscopic imaging before prostatectomy--results of ACRIN prospective multi-institutional clinicopathologic study. *Radiology.* 2009;251(1):122-133.

63. Hricak H, Choyke PL, Eberhardt SC, et al. Imaging prostate cancer: a multidisciplinary perspective. *Radiology.* 2007;243(1):28-53.

64. Noworolski SM, Crane JC, Vigneron DB, et al. A clinical comparison of rigid and inflatable endorectal-coil probes for MRI and 3D MR spectroscopic imaging (MRSI) of the prostate. *Journal of magnetic resonance imaging : JMRI.* 2008;27(5):1077-1082.

65. Eilenberg SS, Tartar VM, Mattrey RF. Reducing magnetic susceptibility differences using liquid fluorocarbon pads (Sat Pad): results with spectral presaturation of fat. *Artificial cells, blood substitutes, and immobilization biotechnology.* 1994;22(4):1477-1483.

66. Rosen Y, Bloch BN, Lenkinski RE, et al. 3T MR of the prostate: reducing susceptibility gradients by inflating the endorectal coil with a barium sulfate suspension. *Magnetic resonance in medicine.* 2007;57(5):898-904.

67. Noworolski SM, Reed GD, Kurhanewicz J, et al. Post-processing correction of the endorectal coil reception effects in MR spectroscopic imaging of the prostate. *Journal of magnetic resonance imaging : JMRI.* 2010;32(3):654-662.

68. Bloch BN, Rofsky NM, Baroni RH, et al. 3 Tesla magnetic resonance imaging of the prostate with combined pelvic phased-array and endorectal coils; Initial experience(1). *Academic radiology.* 2004;11(8):863-867.

69. Chang KJ, Kamel IR, Macura KJ, et al. 3.0-T MR imaging of the abdomen: comparison with 1.5 T. *Radiographics : a review publication of the Radiological Society of North America, Inc.* 2008;28(7):1983-1998.

70. Park BK, Kim B, Kim CK, et al. Comparison of phased-array 3.0-T and endorectal 1.5-T magnetic resonance imaging in the evaluation of local staging accuracy for prostate cancer. *Journal of computer assisted tomography.* 2007;31(4):534-538.

71. Shah ZK, Elias SN, Abaza R, et al. Performance comparison of 1.5-T endorectal coil MRI with 3.0-T nonendorectal coil MRI in patients with prostate cancer. *Academic radiology.* 2015;22(4):467-474.

72. Sosna J, Pedrosa I, Dewolf WC, et al. MR imaging of the prostate at 3 Tesla: comparison of an external phased-array coil to imaging with an endorectal coil at 1.5 Tesla. *Academic radiology.* 2004;11(8):857-862.

73. Turkbey B, Merino MJ, Gallardo EC, et al. Comparison of endorectal coil and nonendorectal coil T2W and diffusion-weighted MRI at 3 Tesla for localizing prostate cancer: correlation with whole-mount histopathology. *Journal of magnetic resonance imaging : JMRI.* 2014;39(6):1443-1448.

74. Vargas C, Saito AI, Hsi WC, et al. Cine-magnetic resonance imaging assessment of intrafraction motion for prostate cancer patients supine or prone with and without a rectal balloon. *American journal of clinical oncology.* 2010;33(1):11-16.

75. Wilder RB, Chittenden L, Mesa AV, et al. A prospective study of intrafraction prostate motion in the prone vs. supine position. *International journal of radiation oncology, biology, physics.* 2010;77(1):165-170.

76. Pasoglou V, Michoux N, Peeters F, et al. Whole-body 3D T1-weighted MR imaging in patients with prostate cancer: feasibility and evaluation in screening for metastatic disease. *Radiology.* 2015;275(1):155-166.

77. Pano B, Sebastia C, Bunesch L, et al. Pathways of lymphatic spread in male urogenital pelvic malignancies. *Radiographics : a review publication of the Radiological Society of North America, Inc.* 2011;31(1):135-160.

78. Qayyum A, Coakley FV, Lu Y, et al. Organ-confined prostate cancer: effect of prior transrectal biopsy on endorectal MRI and MR spectroscopic imaging. *AJR American journal of roentgenology.* 2004;183(4):1079-1083.

79. Sharif-Afshar AR, Feng T, Koopman S, et al. Impact of post prostate biopsy hemorrhage on multiparametric magnetic resonance imaging. *The Canadian journal of urology.* 2015;22(2):7698-7702.

80. Sala E, Akin O, Moskowitz CS, et al. Endorectal MR imaging in the evaluation of seminal vesicle invasion: diagnostic accuracy and multivariate feature analysis. *Radiology.* 2006;238(3):929-937.

81. Tempany CM, Rahmouni AD, Epstein JI, et al. Invasion of the neurovascular bundle by prostate cancer: evaluation with MR imaging. *Radiology.* 1991;181(1):107-112.

82. de Rooij M, Hamoen EH, Witjes JA, et al. Accuracy of Magnetic Resonance Imaging for Local Staging of Prostate Cancer: A Diagnostic Meta-analysis. *Eur Urol.* 2015.

83. Schiebler ML, Schnall MD, Pollack HM, et al. Current role of MR imaging in the staging of adenocarcinoma of the prostate. *Radiology.* 1993;189(2):339-352.

84. Rosenkrantz AB, Neil J, Kong X, et al. Prostate cancer: Comparison of 3D T2-weighted with conventional 2D T2-weighted imaging for image quality and tumor detection. *AJR American journal of roentgenology.* 2010;194(2):446-452.

85. Westphalen AC, Noworolski SM, Harisinghani M, et al. High-Resolution 3-T Endorectal Prostate MRI: A Multireader Study of Radiologist Preference and

Perceived Interpretive Quality of 2D and 3D T2-Weighted Fast Spin-Echo MR Images. *AJR American journal of roentgenology.* 2016;206(1):86-91.

86. desouza NM, Reinsberg SA, Scurr ED, et al. Magnetic resonance imaging in prostate cancer: the value of apparent diffusion coefficients for identifying malignant nodules. *The British journal of radiology.* 2007;80(950):90-95.

87. Gibbs P, Pickles MD, Turnbull LW. Diffusion imaging of the prostate at 3.0 tesla. *Investigative radiology.* 2006;41(2):185-188.

88. Kim CK, Park BK, Lee HM, et al. Value of diffusion-weighted imaging for the prediction of prostate cancer location at 3T using a phased-array coil: preliminary results. *Investigative radiology.* 2007;42(12):842-847.

89. Turkbey B, Pinto PA, Choyke PL. Imaging techniques for prostate cancer: implications for focal therapy. *Nature reviews Urology.* 2009;6(4):191-203.

90. Vargas HA, Akin O, Franiel T, et al. Diffusion-weighted endorectal MR imaging at 3 T for prostate cancer: tumor detection and assessment of aggressiveness. *Radiology.* 2011;259(3):775-784.

91. Nagarajan R, Margolis D, Raman S, et al. Correlation of Gleason scores with diffusion-weighted imaging findings of prostate cancer. *Advances in urology.* 2012;2012:374805.

92. Pang Y, Turkbey B, Bernardo M, et al. Intravoxel incoherent motion MR imaging for prostate cancer: an evaluation of perfusion fraction and diffusion coefficient derived from different b-value combinations. *Magnetic resonance in medicine.* 2013;69(2):553-562.

93. Wang XZ, Wang B, Gao ZQ, et al. Diffusion-weighted imaging of prostate cancer: correlation between apparent diffusion coefficient values and tumor proliferation. *Journal of magnetic resonance imaging : JMRI.* 2009;29(6):1360-1366.

94. Katahira K, Takahara T, Kwee TC, et al. Ultra-high-b-value diffusion-weighted MR imaging for the detection of prostate cancer: evaluation in 201 cases with histopathological correlation. *European radiology.* 2011;21(1):188-196.

95. Rosenkrantz AB, Sabach A, Babb JS, et al. Prostate cancer: comparison of dynamic contrast-enhanced MRI techniques for localization of peripheral zone tumor. *AJR American journal of roentgenology.* 2013;201(3):W471-478.

96. Ueno Y, Takahashi S, Kitajima K, et al. Computed diffusion-weighted imaging using 3-T magnetic resonance imaging for prostate cancer diagnosis. *European radiology.* 2013;23(12):3509-3516.

97. Thoeny HC, Ross BD. Predicting and monitoring cancer treatment response with diffusion-weighted MRI. *Journal of magnetic resonance imaging : JMRI.* 2010;32(1):2-16.

98. Farahani K, Sinha U, Sinha S, et al. Effect of field strength on susceptibility artifacts in magnetic resonance imaging. *Computerized medical imaging and graphics : the official journal of the Computerized Medical Imaging Society.* 1990;14(6):409-413.

99. Mazaheri Y, Vargas HA, Nyman G, et al. Diffusion-weighted MRI of the prostate at 3.0 T: comparison of endorectal coil (ERC) MRI and phased-array coil (PAC) MRI-The impact of SNR on ADC measurement. *European journal of radiology.* 2013;82(10):e515-520.

100. Metens T, Miranda D, Absil J, et al. What is the optimal b value in diffusion-weighted MR imaging to depict prostate cancer at 3T? *European radiology.* 2012;22(3):703-709.

101. Korn N, Kurhanewicz J, Banerjee S, et al. Reduced-FOV excitation decreases susceptibility artifact in diffusion-weighted MRI with endorectal coil for prostate cancer detection. *Magnetic resonance imaging.* 2015;33(1):56-62.

102. Kurhanewicz J, Vigneron DB, Hricak H, et al. Prostate cancer: metabolic response to cryosurgery as detected with 3D H-1 MR spectroscopic imaging. *Radiology.* 1996;200(2):489-496.

103. Shukla-Dave A, Hricak H, Moskowitz C, et al. Detection of prostate cancer with MR spectroscopic imaging: an expanded paradigm incorporating polyamines. *Radiology.* 2007;245(2):499-506.

104. Costello LC, Franklin RB. Concepts of citrate production and secretion by prostate. 1. Metabolic relationships. *The Prostate.* 1991;18(1):25-46.

105. Costello LC, Franklin RB. Novel role of zinc in the regulation of prostate citrate metabolism and its implications in prostate cancer. *The Prostate.* 1998;35(4):285-296.

106. Kaji Y, Kurhanewicz J, Hricak H, et al. Localizing prostate cancer in the presence of postbiopsy changes on MR images: role of proton MR spectroscopic imaging. *Radiology.* 1998;206(3):785-790.

107. Kurhanewicz J, Vigneron DB. Advances in MR spectroscopy of the prostate. *Magnetic resonance imaging clinics of North America.* 2008;16(4):697-710, ix-x.

108. Kurhanewicz J, Vigneron DB, Hricak H, et al. Three-dimensional H-1 MR spectroscopic imaging of the in situ human prostate with high (0.24-0.7-cm3) spatial resolution. *Radiology.* 1996;198(3):795-805.

109. Ackerstaff E, Pflug BR, Nelson JB, et al. Detection of increased choline compounds with proton nuclear magnetic resonance spectroscopy subsequent to malignant transformation of human prostatic epithelial cells. *Cancer research.* 2001;61(9):3599-3603.

110. Hricak H. MR imaging and MR spectroscopic imaging in the pre-treatment evaluation of prostate cancer. *The British journal of radiology.* 2005;78 Spec No 2:S103-111.

111. Podo F. Tumour phospholipid metabolism. *NMR in biomedicine.* 1999;12(7):413-439.

112. Kurhanewicz J, Swanson MG, Nelson SJ, et al. Combined magnetic resonance imaging and spectroscopic imaging approach to molecular imaging of prostate cancer. *Journal of magnetic resonance imaging : JMRI.* 2002;16(4):451-463.

113. Ganie FA, Wani MS, Shaheen F, et al. Endorectal coil MRI and MR-spectroscopic imaging in patients with elevated serum prostate specific antigen with negative trus transrectal ultrasound guided biopsy. *Urology annals.* 2013;5(3):172-178.

114. Kobus T, Wright AJ, Scheenen TW, et al. Mapping of prostate cancer by 1H MRSI. *NMR in biomedicine.* 2014;27(1):39-52.

115. Cunningham CH, Vigneron DB, Chen AP, et al. Design of flyback echo-planar readout gradients for magnetic resonance spectroscopic imaging. *Magnetic resonance in medicine.* 2005;54(5):1286-1289.

116. Lagemaat MW, Breukels V, Vos EK, et al. H MR spectroscopic imaging of the prostate at 7T using spectral-spatial pulses. *Magnetic resonance in medicine.* 2015.

117. Tran TK, Vigneron DB, Sailasuta N, et al. Very selective suppression pulses for clinical MRSI studies of brain and prostate cancer. *Magnetic resonance in medicine.* 2000;43(1):23-33.

118. Males RG, Vigneron DB, Star-Lack J, et al. Clinical application of BASING and spectral/spatial water and lipid suppression pulses for prostate cancer staging and localization by in vivo 3D 1H magnetic resonance spectroscopic imaging. *Magnetic resonance in medicine.* 2000;43(1):17-22.

119. Star-Lack J, Nelson SJ, Kurhanewicz J, et al. Improved water and lipid suppression for 3D PRESS CSI using RF band selective inversion with gradient dephasing (BASING). *Magnetic resonance in medicine.* 1997;38(2):311-321.

120. Schricker AA, Pauly JM, Kurhanewicz J, et al. Dualband spectral-spatial RF pulses for prostate MR spectroscopic imaging. *Magnetic resonance in medicine.* 2001;46(6):1079-1087.

121. Cunningham CH, Vigneron DB, Chen AP, et al. Design of symmetric-sweep spectral-spatial RF pulses for spectral editing. *Magnetic resonance in medicine.* 2004;52(1):147-153.

122. Maudsley AA, Darkazanli A, Alger JR, et al. Comprehensive processing, display and analysis for in vivo MR spectroscopic imaging. *NMR in biomedicine.* 2006;19(4):492-503.

123. Wilson M, Reynolds G, Kauppinen RA, et al. A constrained least-squares approach to the automated quantitation of in vivo (1)H magnetic resonance spectroscopy data. *Magnetic resonance in medicine.* 2011;65(1):1-12.

124. Nelson SJB, T. R. A study of the accuracy of quantification which can be obtained from 1-D NMR spectra using the PIQABLE algorithm. *Journal of Magnetic Resonance.* 1989;84(1):95-109.

125. Jung JA, Coakley FV, Vigneron DB, et al. Prostate depiction at endorectal MR spectroscopic imaging: investigation of a standardized evaluation system. *Radiology.* 2004;233(3):701-708.

126. Futterer JJ, Scheenen TW, Heijmink SW, et al. Standardized threshold approach using three-dimensional proton magnetic resonance spectroscopic imaging in prostate cancer localization of the entire prostate. *Invest Radiol.* 2007;42(2):116-122.

127. Kobus T, Hambrock T, Hulsbergen-van de Kaa CA, et al. In vivo assessment of prostate cancer aggressiveness using magnetic resonance spectroscopic imaging at 3 T with an endorectal coil. *Eur Urol.* 2011;60(5):1074-1080.

128. Selnaes KM, Gribbestad IS, Bertilsson H, et al. Spatially matched in vivo and ex vivo MR metabolic profiles of prostate cancer -- investigation of a correlation with Gleason score. *NMR in biomedicine.* 2013;26(5):600-606.

129. Verma S, Rajesh A, Futterer JJ, et al. Prostate MRI and 3D MR spectroscopy: how we do it. *AJR American journal of roentgenology.* 2010;194(6):1414-1426.

130. Sciarra A, Panebianco V, Ciccariello M, et al. Magnetic resonance spectroscopic imaging (1H-MRSI) and dynamic contrast-enhanced magnetic resonance (DCE-

MRI): pattern changes from inflammation to prostate cancer. *Cancer investigation.* 2010;28(4):424-432.

131. Shukla-Dave A, Hricak H, Eberhardt SC, et al. Chronic prostatitis: MR imaging and 1H MR spectroscopic imaging findings--initial observations. *Radiology.* 2004;231(3):717-724.

132. Noworolski SM, Henry RG, Vigneron DB, et al. Dynamic contrast-enhanced MRI in normal and abnormal prostate tissues as defined by biopsy, MRI, and 3D MRSI. *Magnetic resonance in medicine.* 2005;53(2):249-255.

133. Noworolski SMR, G. R.; Kurhanewicz, J. A Novel Luminal Water Model for DCE MRI of Prostatic Tissues. Proc. Intl. Soc. Mag. Reson. Med. 19 2011; Montreal, Canada.

134. Bergers G, Benjamin LE. Tumorigenesis and the angiogenic switch. *Nature reviews Cancer.* 2003;3(6):401-410.

135. Ferrer FA, Miller LJ, Andrawis RI, et al. Vascular endothelial growth factor (VEGF) expression in human prostate cancer: in situ and in vitro expression of VEGF by human prostate cancer cells. *The Journal of urology.* 1997;157(6):2329-2333.

136. Huss WJ, Hanrahan CF, Barrios RJ, et al. Angiogenesis and prostate cancer: identification of a molecular progression switch. *Cancer research.* 2001;61(6):2736-2743.

137. Latil A, Bieche I, Pesche S, et al. VEGF overexpression in clinically localized prostate tumors and neuropilin-1 overexpression in metastatic forms. *International journal of cancer Journal international du cancer.* 2000;89(2):167-171.

138. Russo G, Mischi M, Scheepens W, et al. Angiogenesis in prostate cancer: onset, progression and imaging. *BJU international.* 2012;110(11 Pt C):E794-808.

139. Bigler SA, Deering RE, Brawer MK. Comparison of microscopic vascularity in benign and malignant prostate tissue. *Human pathology.* 1993;24(2):220-226.

140. McDonald DM, Baluk P. Significance of blood vessel leakiness in cancer. *Cancer research.* 2002;62(18):5381-5385.

141. Sottnik JL, Zhang J, Macoska JA, et al. The PCa Tumor Microenvironment. *Cancer microenvironment : official journal of the International Cancer Microenvironment Society.* 2011;4(3):283-297.

142. Isebaert S, Van den Bergh L, Haustermans K, et al. Multiparametric MRI for prostate cancer localization in correlation to whole-mount histopathology. *Journal of magnetic resonance imaging : JMRI.* 2013;37(6):1392-1401.

143. Ito H, Kamoi K, Yokoyama K, et al. Visualization of prostate cancer using dynamic contrast-enhanced MRI: comparison with transrectal power Doppler ultrasound. *The British journal of radiology.* 2003;76(909):617-624.

144. Jackson AS, Reinsberg SA, Sohaib SA, et al. Dynamic contrast-enhanced MRI for prostate cancer localization. *The British journal of radiology.* 2009;82(974):148-156.

145. Kim JK, Hong SS, Choi YJ, et al. Wash-in rate on the basis of dynamic contrast-enhanced MRI: usefulness for prostate cancer detection and localization. *Journal of magnetic resonance imaging : JMRI.* 2005;22(5):639-646.

146. Ocak I, Bernardo M, Metzger G, et al. Dynamic contrast-enhanced MRI of prostate cancer at 3 T: a study of pharmacokinetic parameters. *AJR American journal of roentgenology.* 2007;189(4):849.

147. Chen YJ, Chu WC, Pu YS, et al. Washout gradient in dynamic contrast-enhanced MRI is associated with tumor aggressiveness of prostate cancer. *Journal of magnetic resonance imaging : JMRI.* 2012;36(4):912-919.

148. Vos EK, Litjens GJ, Kobus T, et al. Assessment of prostate cancer aggressiveness using dynamic contrast-enhanced magnetic resonance imaging at 3 T. *Eur Urol.* 2013;64(3):448-455.

149. Rosenkrantz AB, Taneja SS. Radiologist, be aware: ten pitfalls that confound the interpretation of multiparametric prostate MRI. *AJR American journal of roentgenology.* 2014;202(1):109-120.

150. Hoeks CM, Hambrock T, Yakar D, et al. Transition zone prostate cancer: detection and localization with 3-T multiparametric MR imaging. *Radiology.* 2013;266(1):207-217.

151. Kershaw LE, Buckley DL. Precision in measurements of perfusion and microvascular permeability with T1-weighted dynamic contrast-enhanced MRI. *Magnetic resonance in medicine.* 2006;56(5):986-992.

152. Fennessy FM, Fedorov A, Penzkofer T, et al. Quantitative pharmacokinetic analysis of prostate cancer DCE-MRI at 3T: comparison of two arterial input functions on cancer detection with digitized whole mount histopathological validation. *Magnetic resonance imaging.* 2015;33(7):886-894.

153. Perdona S, Di Lorenzo G, Autorino R, et al. Combined magnetic resonance spectroscopy and dynamic contrast-enhanced imaging for prostate cancer detection. *Urologic oncology.* 2013;31(6):761-765.

154. Quon J, Kielar AZ, Jain R, et al. Assessing the utilization of functional imaging in multiparametric prostate MRI in routine clinical practice. *Clinical radiology.* 2015;70(4):373-378.

155. Turkbey B, Mani H, Aras O, et al. Prostate cancer: can multiparametric MR imaging help identify patients who are candidates for active surveillance? *Radiology.* 2013;268(1):144-152.

156. Zhang X, Quan X, Lu S, et al. The clinical value of dynamic contrast-enhanced magnetic resonance imaging at 3.0T to detect prostate cancer. *The Journal of international medical research.* 2014;42(5):1077-1084.

157. Rosenkrantz AB, Geppert C, Grimm R, et al. Dynamic contrast-enhanced MRI of the prostate with high spatiotemporal resolution using compressed sensing, parallel imaging, and continuous golden-angle radial sampling: preliminary experience. *Journal of magnetic resonance imaging : JMRI.* 2015;41(5):1365-1373.

158. Fennessy FM, McKay RR, Beard CJ, et al. Dynamic contrast-enhanced magnetic resonance imaging in prostate cancer clinical trials: potential roles and possible pitfalls. *Translational oncology.* 2014;7(1):120-129.

159. Rosenkrantz AB, Chandarana H, Hindman N, et al. Computed diffusion-weighted imaging of the prostate at 3 T: impact on image quality and tumour detection. *European radiology.* 2013;23(11):3170-3177.

160. Verma S, Turkbey B, Muradyan N, et al. Overview of dynamic contrast-enhanced MRI in prostate cancer diagnosis and management. *AJR American journal of roentgenology.* 2012;198(6):1277-1288.

161. Alonzi R, Padhani AR, Allen C. Dynamic contrast enhanced MRI in prostate cancer. *European journal of radiology.* 2007;63(3):335-350.

162. Girouin N, Mege-Lechevallier F, Tonina Senes A, et al. Prostate dynamic contrast-enhanced MRI with simple visual diagnostic criteria: is it reasonable? *European radiology.* 2007;17(6):1498-1509.

163. Hansford BG, Peng Y, Jiang Y, et al. Dynamic Contrast-enhanced MR Imaging Curve-type Analysis: Is It Helpful in the Differentiation of Prostate Cancer from Healthy Peripheral Zone? *Radiology.* 2015;275(2):448-457.

164. Ogura K, Maekawa S, Okubo K, et al. Dynamic endorectal magnetic resonance imaging for local staging and detection of neurovascular bundle involvement of prostate cancer: correlation with histopathologic results. *Urology.* 2001;57(4):721-726.

165. Pallares J, Rojo F, Iriarte J, et al. Study of microvessel density and the expression of the angiogenic factors VEGF, bFGF and the receptors Flt-1 and FLK-1 in benign, premalignant and malignant prostate tissues. *Histology and histopathology.* 2006;21(8):857-865.

166. Weidner N, Carroll PR, Flax J, et al. Tumor angiogenesis correlates with metastasis in invasive prostate carcinoma. *The American journal of pathology.* 1993;143(2):401-409.

167. Isebaert S, De Keyzer F, Haustermans K, et al. Evaluation of semi-quantitative dynamic contrast-enhanced MRI parameters for prostate cancer in correlation to whole-mount histopathology. *European journal of radiology.* 2012;81(3):e217-222.

168. Oto A, Yang C, Kayhan A, et al. Diffusion-weighted and dynamic contrast-enhanced MRI of prostate cancer: correlation of quantitative MR parameters with Gleason score and tumor angiogenesis. *AJR American journal of roentgenology.* 2011;197(6):1382-1390.

169. Peng Y, Jiang Y, Yang C, et al. Quantitative analysis of multiparametric prostate MR images: differentiation between prostate cancer and normal tissue and correlation with Gleason score--a computer-aided diagnosis development study. *Radiology.* 2013;267(3):787-796.

170. Hegde JV, Mulkern RV, Panych LP, et al. Multiparametric MRI of prostate cancer: an update on state-of-the-art techniques and their performance in detecting and localizing prostate cancer. *Journal of magnetic resonance imaging : JMRI.* 2013;37(5):1035-1054.

171. Sourbron SP, Buckley DL. On the scope and interpretation of the Tofts models for DCE-MRI. *Magnetic resonance in medicine.* 2011;66(3):735-745.

172. Sourbron SP, Buckley DL. Classic models for dynamic contrast-enhanced MRI. *NMR in biomedicine.* 2013;26(8):1004-1027.

173. Tofts PS, Brix G, Buckley DL, et al. Estimating kinetic parameters from dynamic contrast-enhanced T(1)-weighted MRI of a diffusable tracer: standardized quantities and symbols. *Journal of magnetic resonance imaging : JMRI.* 1999;10(3):223-232.

174. Fennessy FM, Fedorov A, Gupta SN, et al. Practical considerations in T1 mapping of prostate for dynamic contrast enhancement pharmacokinetic analyses. *Magnetic resonance imaging.* 2012;30(9):1224-1233.

175. Fedorov A, Fluckiger J, Ayers GD, et al. A comparison of two methods for estimating DCE-MRI parameters via individual and cohort based AIFs in prostate cancer: a step towards practical implementation. *Magnetic resonance imaging.* 2014;32(4):321-329.

176. Port RE, Knopp MV, Brix G. Dynamic contrast-enhanced MRI using Gd-DTPA: interindividual variability of the arterial input function and consequences for the assessment of kinetics in tumors. *Magnetic resonance in medicine.* 2001;45(6):1030-1038.

177. Sanz-Requena R, Prats-Montalban JM, Marti-Bonmati L, et al. Automatic individual arterial input functions calculated from PCA outperform manual and population-averaged approaches for the pharmacokinetic modeling of DCE-MR images. *Journal of magnetic resonance imaging : JMRI.* 2015;42(2):477-487.

178. Ortuno JE, Ledesma-Carbayo MJ, Simoes RV, et al. DCE@urLAB: a dynamic contrast-enhanced MRI pharmacokinetic analysis tool for preclinical data. *BMC bioinformatics.* 2013;14:316.

179. Schmid VJ, Whitcher B, Padhani AR, et al. Bayesian methods for pharmacokinetic models in dynamic contrast-enhanced magnetic resonance imaging. *IEEE transactions on medical imaging.* 2006;25(12):1627-1636.

180. Schmid VJ, Whitcher B, Padhani AR, et al. A Bayesian hierarchical model for the analysis of a longitudinal dynamic contrast-enhanced MRI oncology study. *Magnetic resonance in medicine.* 2009;61(1):163-174.

181. Smith DS, Li X, Arlinghaus LR, et al. DCEMRI.jl: a fast, validated, open source toolkit for dynamic contrast enhanced MRI analysis. *PeerJ.* 2015;3:e909.

182. Zollner FG, Weisser G, Reich M, et al. UMMPerfusion: an open source software tool towards quantitative MRI perfusion analysis in clinical routine. *Journal of digital imaging.* 2013;26(2):344-352.

183. Dickinson L, Ahmed HU, Allen C, et al. Magnetic resonance imaging for the detection, localisation, and characterisation of prostate cancer: recommendations from a European consensus meeting. *Eur Urol.* 2011;59(4):477-494.

184. Kirkham AP, Haslam P, Keanie JY, et al. Prostate MRI: who, when, and how? Report from a UK consensus meeting. *Clinical radiology.* 2013;68(10):1016-1023.

185. Kitajima K, Kaji Y, Fukabori Y, et al. Prostate cancer detection with 3 T MRI: comparison of diffusion-weighted imaging and dynamic contrast-enhanced MRI in combination with T2-weighted imaging. *Journal of magnetic resonance imaging : JMRI.* 2010;31(3):625-631.

186. MR Prostate Imaging Reporting and Data System version 2.0. http://www.acr.org/~/media/ACR/Documents/PDF/QualitySafety/Resources/PIRADS/PIRADS V2.pdf. Accessed February 7th, 2015.

187. Society AC. Cancer Facts and Figures 2016. *Atlanta: American Cancer Society.* 2016.

188. Grossfeld GD, Carroll PR. Prostate cancer early detection: a clinical perspective. *Epidemiol Rev.* 2001;23(1):173-180.

189. Sanda MG, Dunn RL, Michalski J, et al. Quality of life and satisfaction with outcome among prostate-cancer survivors. *N Engl J Med.* 2008;358(12):1250-1261.

190. Makarov DV, Partin AW. Focal therapy for prostate cancer. *Rev Urol.* 2008;10(1):81-82.

191. Fuchsjager M, Akin O, Shukla-Dave A, et al. The role of MRI and MRSI in diagnosis, treatment selection, and post-treatment follow-up for prostate cancer. *Clin Adv Hematol Oncol.* 2009;7(3):193-202.

192. Bomers JG, Sedelaar JP, Barentsz JO, et al. MRI-guided interventions for the treatment of prostate cancer. *AJR Am J Roentgenol.* 2012;199(4):714-720.

193. Hricak H, White S, Vigneron D, et al. Carcinoma of the prostate gland: MR imaging with pelvic phased-array coils versus integrated endorectal--pelvic phased-array coils. *Radiology.* 1994;193(3):703-709.

194. Kim Y, Hsu IC, Pouliot J, et al. Expandable and rigid endorectal coils for prostate MRI: impact on prostate distortion and rigid image registration. *Med Phys.* 2005;32(12):3569-3578.

195. Jonmarker S, Valdman A, Lindberg A, et al. Tissue shrinkage after fixation with formalin injection of prostatectomy specimens. *Virchows Arch.* 2006;449(3):297-301.

196. Schned AR, Wheeler KJ, Hodorowski CA, et al. Tissue-shrinkage correction factor in the calculation of prostate cancer volume. *Am J Surg Pathol.* 1996;20(12):1501-1506.

197. Jager GJ, Ruijter ET, van de Kaa CA, et al. Local staging of prostate cancer with endorectal MR imaging: correlation with histopathology. *AJR Am J Roentgenol.* 1996;166(4):845-852.

198. Orczyk C, Mikheev A, Rosenkrantz A, et al. Imaging of prostate cancer: a platform for 3D co-registration of in-vivo MRI ex-vivo MRI and pathology. 2012:83162M-83162M.

199. Ward AD, Crukley C, McKenzie CA, et al. Prostate: Registration of Digital Histopathologic Images to in Vivo MR Images Acquired by Using Endorectal Receive Coil. *Radiology.* 2012;263(3):856-864.

200. Samavati N, McGrath DM, Lee J, et al. Biomechanical model-based deformable registration of MRI and histopathology for clinical prostatectomy. *J Pathol Inform.* 2011;2:S10.

201. Chappelow J, Bloch BN, Rofsky N, et al. Elastic registration of multimodal prostate MRI and histology via multiattribute combined mutual information. *Med Phys.* 2011;38(4):2005-2018.

202. Patel P, Chappelow J, Tomaszewski J, et al. Spatially weighted mutual information (SWMI) for registration of digitally reconstructed ex vivo whole mount histology and in vivo prostate MRI. *Conf Proc IEEE Eng Med Biol Soc.* 2011;2011:6269-6272.

203. Park H, Piert MR, Khan A, et al. Registration methodology for histological sections and in vivo imaging of human prostate. *Acad Radiol.* 2008;15(8):1027-1039.

204. Kimm SY, Tarin TV, Lee JH, et al. Methods for registration of magnetic resonance images of ex vivo prostate specimens with histology. *J Magn Reson Imaging.* 2012;36(1):206-212.

205. Mazaheri Y, Bokacheva L, Kroon DJ, et al. Semi-automatic deformable registration of prostate MR images to pathological slices. *J Magn Reson Imaging.* 2010;32(5):1149-1157.

206. Cheung MR, Krishnan K. Using manual prostate contours to enhance deformable registration of endorectal MRI. *Comput Methods Programs Biomed.* 2012.

207. Noworolski SM, Reed GD, Kurhanewicz J, et al. Post-Processing Correction of the Endorectal Coil Reception Effects in MR Spectroscopic Imaging of the Prostate. *Journal of Magnetic Resonance Imaging.* 2010;32(3):654-662.

208. Shah V, Pohida T, Turkbey B, et al. A method for correlating in vivo prostate magnetic resonance imaging and histopathology using individualized magnetic resonance-based molds. *Rev Sci Instrum.* 2009;80(10):104301.

209. Turkbey B, Pinto PA, Mani H, et al. Prostate cancer: value of multiparametric MR imaging at 3 T for detection--histopathologic correlation. *Radiology.* 2010;255(1):89-99.

210. Trivedi H, Turkbey B, Rastinehad AR, et al. Use of patient-specific MRI-based prostate mold for validation of multiparametric MRI in localization of prostate cancer. *Urology.* 2012;79(1):233-239.

211. Siegel RL, Miller KD, Jemal A. Cancer statistics, 2016. *CA: a cancer journal for clinicians.* 2016;66(1):7-30.

212. Resnick MJ, Koyama T, Fan KH, et al. Long-term functional outcomes after treatment for localized prostate cancer. *The New England journal of medicine.* 2013;368(5):436-445.

213. Gustafsson O, Norming U, Almgard LE, et al. Diagnostic methods in the detection of prostate cancer: a study of a randomly selected population of 2,400 men. *The Journal of urology.* 1992;148(6):1827-1831.

214. Loeb S, Vellekoop A, Ahmed HU, et al. Systematic review of complications of prostate biopsy. *Eur Urol.* 2013;64(6):876-892.

215. Wang L, Mazaheri Y, Zhang J, et al. Assessment of biologic aggressiveness of prostate cancer: correlation of MR signal intensity with Gleason grade after radical prostatectomy. *Radiology.* 2008;246(1):168-176.

216. Hambrock T, Somford DM, Huisman HJ, et al. Relationship between Apparent Diffusion Coefficients at 3.0-T MR Imaging and Gleason Grade in Peripheral Zone Prostate Cancer. *Radiology.* 2011;259(2):453-461.

217. Peng YH, Jiang YL, Yang C, et al. Quantitative Analysis of Multiparametric Prostate MR Images: Differentiation between Prostate Cancer and Normal Tissue and Correlation with Gleason Score-A Computer-aided Diagnosis Development Study. *Radiology.* 2013;267(3):787-796.

218. Turkbey B, Shah VP, Pang Y, et al. Is apparent diffusion coefficient associated with clinical risk scores for prostate cancers that are visible on 3-T MR images? *Radiology.* 2011;258(2):488-495.

219. Zakian KL, Sircar K, Hricak H, et al. Correlation of proton MR spectroscopic imaging with Gleason score based on step-section pathologic analysis after radical prostatectomy. *Radiology.* 2005;234(3):804-814.

220. Chen YJ, Chu WC, Pu YS, et al. Washout gradient in dynamic contrast-enhanced MRI is associated with tumor aggressiveness of prostate cancer. *Journal of magnetic resonance imaging : JMRI.* 2012;36(4):912-919.

221. Chen AP, Cunningham CH, Ozturk-Isik E, et al. High-speed 3T MR spectroscopic imaging of prostate with flyback echo-planar encoding. *Journal of magnetic resonance imaging : JMRI.* 2007;25(6):1288-1292.

222. Tofts PS, Kermode AG. Measurement of the blood-brain barrier permeability and leakage space using dynamic MR imaging. 1. Fundamental concepts. *Magnetic resonance in medicine.* 1991;17(2):357-367.

223. Noworolski SM, Reed GD, Kurhanewicz J. A Novel Luminal Water Model for DCE MRI of Prostatic Tissues. Paper presented at: International Society for Magnetic Resonance in Medicine 2011; Montreal.

224. *R: A language and environment for statistical computing* [computer program]. Vienna, Austria: R Foundation for Statistical Computing; 2015.

225. Giusti S, Caramella D, Fruzzetti E, et al. Peripheral zone prostate cancer. Pre-treatment evaluation with MR and 3D (1)H MR spectroscopic imaging: correlation with pathologic findings. *Abdominal imaging.* 2010;35(6):757-763.

226. Dwivedi DK, Kumar R, Bora GS, et al. Stratification of the aggressiveness of prostate cancer using pre-biopsy multiparametric MRI (mpMRI). *NMR in biomedicine.* 2016;29(3):232-238.

227. Vos EK, Kobus T, Litjens GJ, et al. Multiparametric Magnetic Resonance Imaging for Discriminating Low-Grade From High-Grade Prostate Cancer. *Investigative radiology.* 2015;50(8):490-497.

228. Fehr D, Veeraraghavan H, Wibmer A, et al. Automatic classification of prostate cancer Gleason scores from multiparametric magnetic resonance images. *Proc Natl Acad Sci USA.* 2015;112(46):E6265-6273.

229. Liu L, Tian Z, Zhang Z, et al. Computer-aided Detection of Prostate Cancer with MRI: Technology and Applications. *Academic radiology.* 2016;23(8):1024-1046.

230. Niaf E, Rouviere O, Mege-Lechevallier F, et al. Computer-aided diagnosis of prostate cancer in the peripheral zone using multiparametric MRI. *Physics in medicine and biology.* 2012;57(12):3833-3851.

231. Dikaios N, Alkalbani J, Sidhu HS, et al. Logistic regression model for diagnosis of transition zone prostate cancer on multi-parametric MRI. *European radiology.* 2015;25(2):523-532.

232. Hambrock T, Vos PC, Hulsbergen-van de Kaa CA, et al. Prostate cancer: computer-aided diagnosis with multiparametric 3-T MR imaging--effect on observer performance. *Radiology.* 2013;266(2):521-530.

233. Lavery HJ, Droller MJ. Do Gleason Patterns 3 and 4 Prostate Cancer Represent Separate Disease States? *The Journal of urology.* 2012;188(5):1667-1675.

234. Klein EA, Cooperberg MR, Magi-Galluzzi C, et al. A 17-gene assay to predict prostate cancer aggressiveness in the context of Gleason grade heterogeneity, tumor multifocality, and biopsy undersampling. *European urology.* 2014;66(3):550-560.

235. Priolo C, Pyne S, Rose J, et al. AKT1 and MYC induce distinctive metabolic fingerprints in human prostate cancer. *Cancer research.* 2014;74(24):7198-7204.

236. Barentsz JO, Weinreb JC, Verma S, et al. Synopsis of the PI-RADS v2 Guidelines for Multiparametric Prostate Magnetic Resonance Imaging and Recommendations for Use. *European urology.* 2016;69(1):41-49.

237. Kitajima K, Takahashi S, Ueno Y, et al. Clinical utility of apparent diffusion coefficient values obtained using high b-value when diagnosing prostate cancer using 3 tesla MRI: comparison between ultra-high b-value (2000 s/mm(2)) and standard high b-

value (1000 s/mm(2)). *Journal of magnetic resonance imaging : JMRI.* 2012;36(1):198-205.

238. Ueno Y, Kitajima K, Sugimura K, et al. Ultra-high b-value diffusion-weighted MRI for the detection of prostate cancer with 3-T MRI. *Journal of magnetic resonance imaging : JMRI.* 2013;38(1):154-160.

239. Kass M, Witkin A, Terzopoulos D. Snakes - Active Contour Models. *Int J Comput Vision.* 1987;1(4):321-331.

240. Ivins J, Porrill J. Everything you always wanted to know about snakes (but were afraid to ask). *AIVRU Technical Memo 86.* 1993;July(Revised June 1995, March 2000, 2000.).

241. Zhao JH, Chen BY, Sun MG, et al. Improved Algorithm for Gradient Vector Flow Based Active Contour Model Using Global and Local Information. *Sci World J.* 2013.

242. Zhao F, Xie XH. Energy minimization in medical image analysis: Methodologies and applications. *Int J Numer Meth Bio.* 2016;32(2).

243. Kirkpatrick S, Gelatt CD, Jr., Vecchi MP. Optimization by simulated annealing. *Science.* 1983;220(4598):671-680.

244. Kolmogorov V, Zabih R. What energy functions can be minimized via graph cuts? *Ieee T Pattern Anal.* 2004;26(2):147-159.

245. Szeliski R, Zabih R, Scharstein D, et al. A comparative study of energy minimization methods for Markov random fields. *Lect Notes Comput Sc.* 2006;3952:16-29.

246. Chan TF, Vese LA. Active contours without edges. *Ieee T Image Process.* 2001;10(2):266-277.

247. Boscolo R, Brown MS, McNitt-Gray MF. Medical image segmentation with knowledge-guided robust active contours. *Radiographics : a review publication of the Radiological Society of North America, Inc.* 2002;22(2):437-448.

248. Li B, Acton ST. Active contour external force using vector field convolution for image segmentation. *Ieee T Image Process.* 2007;16(8):2096-2106.

249. Bing X, Wei Y, Charoensak C. Face contour tracking in video using active contour model. *Ieee Image Proc.* 2004:1021-1024.

250. Pardas M, Sayrol E. Motion estimation based tracking of active contours. *Pattern Recogn Lett.* 2001;22(13):1447-1456.

251. Xu CY, Prince JL. Gradient vector flow: A new external force for snakes. *Proc Cvpr Ieee.* 1997:66-71.

252. Prince JL, Xu C. A new external force model for snakes. *Proc 1996 Image and Multidimensional Signal Processing Workshop.* 1996:30-31.

253. Cohen LD. On Active Contour Models and Balloons. *Cvgip-Imag Understan.* 1991;53(2):211-218.

254. Cohen LD, Cohen I. Finite-Element Methods for Active Contour Models and Balloons for 2-D and 3-D Images. *Ieee T Pattern Anal.* 1993;15(11):1131-1147.

255. Xu CY, Prince JL. Generalized gradient vector flow external forces for active contours. *Signal Process.* 1998;71(2):131-139.

256. Fernandes ET, Sundaram CP, Long R, et al. Biopsy Gleason score: how does it correlate with the final pathological diagnosis in prostate cancer? *British journal of urology.* 1997;79(4):615-617.

257. Steinberg DM, Sauvageot J, Piantadosi S, et al. Correlation of prostate needle biopsy and radical prostatectomy Gleason grade in academic and community settings. *The American journal of surgical pathology.* 1997;21(5):566-576.

258. de Rooij M, Hamoen EH, Futterer JJ, et al. Accuracy of multiparametric MRI for prostate cancer detection: a meta-analysis. *AJR American journal of roentgenology.* 2014;202(2):343-351.

259. Rouvière O, Champagnac J. Prostate Cancer Imaging: An Ongoing Change of Paradigm. In: Bolla M, van Poppel H, eds. *Management of Prostate Cancer: A Multidisciplinary Approach*. Cham: Springer International Publishing; 2017:111-126.

260. Turkbey B, Brown AM, Sankineni S, et al. Multiparametric prostate magnetic resonance imaging in the evaluation of prostate cancer. *CA: a cancer journal for clinicians.* 2016;66(4):326-336.

261. Denmeade SR, Isaacs JT. A history of prostate cancer treatment. *Nature reviews Cancer.* 2002;2(5):389-396.

262. Irshad S, Bansal M, Castillo-Martin M, et al. A molecular signature predictive of indolent prostate cancer. *Science translational medicine.* 2013;5(202):202ra122.

263. Mitchell T, Neal DE. The genomic evolution of human prostate cancer. *British journal of cancer.* 2015;113(2):193-198.

264. Trewartha D, Carter K. Advances in prostate cancer treatment. *Nature reviews Drug discovery.* 2013;12(11):823-824.

265. Bonekamp D, Jacobs MA, El-Khouli R, et al. Advancements in MR imaging of the prostate: from diagnosis to interventions. *Radiographics : a review publication of the Radiological Society of North America, Inc.* 2011;31(3):677-703.

266. Langer DL, van der Kwast TH, Evans AJ, et al. Intermixed normal tissue within prostate cancer: effect on MR imaging measurements of apparent diffusion coefficient and T2--sparse versus dense cancers. *Radiology.* 2008;249(3):900-908.

267. Ahmed HU, Arya M, Freeman A, et al. Do low-grade and low-volume prostate cancers bear the hallmarks of malignancy? *The Lancet Oncology.* 2012;13(11):e509-517.

268. Siegel RL, Miller KD, Jemal A. Cancer Statistics, 2016. *Ca-Cancer J Clin.* 2016;66(1):7-30.

269. Arumainayagam N, Kumaar S, Ahmed HU, et al. Accuracy of multiparametric magnetic resonance imaging in detecting recurrent prostate cancer after radiotherapy. *BJU international.* 2010;106(7):991-997.

270. Barchetti F, Panebianco V. Multiparametric MRI for recurrent prostate cancer post radical prostatectomy and postradiation therapy. *BioMed research international.* 2014;2014:316272.

271. Tamada T, Sone T, Jo Y, et al. Locally recurrent prostate cancer after high-dose-rate brachytherapy: the value of diffusion-weighted imaging, dynamic contrast-enhanced MRI, and T2-weighted imaging in localizing tumors. *AJR American journal of roentgenology.* 2011;197(2):408-414.

272. Vargas HA, Wassberg C, Akin O, et al. MR imaging of treated prostate cancer. *Radiology.* 2012;262(1):26-42.

273. Roehrborn CG. Benign prostatic hyperplasia: an overview. *Reviews in urology.* 2005;7 Suppl 9:S3-S14.

274. Chute CG, Panser LA, Girman CJ, et al. The prevalence of prostatism: a population-based survey of urinary symptoms. *The Journal of urology.* 1993;150(1):85-89.

275. Heinlein CA, Chang C. Androgen receptor in prostate cancer. *Endocrine reviews.* 2004;25(2):276-308.

276. Knudsen KE, Penning TM. Partners in crime: deregulation of AR activity and androgen synthesis in prostate cancer. *Trends in endocrinology and metabolism: TEM.* 2010;21(5):315-324.

277. Moyher SE, Vigneron DB, Nelson SJ. Surface Coil Mr-Imaging of the Human Brain with an Analytic Reception Profile Correction. *Jmri-J Magn Reson Im.* 1995;5(2):139-144.

278. Aggarwal S, Thareja S, Verma A, et al. An overview on 5alpha-reductase inhibitors. *Steroids.* 2010;75(2):109-153.

279. Nickel JC, Gilling P, Tammela TL, et al. Comparison of dutasteride and finasteride for treating benign prostatic hyperplasia: the Enlarged Prostate International Comparator Study (EPICS). *BJU international.* 2011;108(3):388-394.

280. Chung HT, Noworolski SM, Kurhanewicz J, et al. A pilot study of endorectal magnetic resonance imaging and magnetic resonance spectroscopic imaging changes with dutasteride in patients with low risk prostate cancer. *BJU international.* 2011;108(8 Pt 2):E164-170.

281. Rittmaster RS, Norman RW, Thomas LN, et al. Evidence for atrophy and apoptosis in the prostates of men given finasteride. *The Journal of clinical endocrinology and metabolism.* 1996;81(2):814-819.

282. Wang X, Kruithof-de Julio M, Economides KD, et al. A luminal epithelial stem cell that is a cell of origin for prostate cancer. *Nature.* 2009;461(7263):495-500.

283. Halpern EJ, Gomella LG, Forsberg F, et al. Contrast enhanced transrectal ultrasound for the detection of prostate cancer: a randomized, double-blind trial of dutasteride pretreatment. *The Journal of urology.* 2012;188(5):1739-1745.

284. Ives EP, Gomella LG, Halpern EJ. Effect of dutasteride therapy on Doppler US evaluation of prostate: preliminary results. *Radiology.* 2005;237(1):197-201.

285. Mitterberger M, Pinggera G, Horninger W, et al. Dutasteride prior to contrast-enhanced colour Doppler ultrasound prostate biopsy increases prostate cancer detection. *Eur Urol.* 2008;53(1):112-117.

286. Truong H, Logan J, Turkbey B, et al. MRI characterization of the dynamic effects of 5alpha-reductase inhibitors on prostate zonal volumes. *The Canadian journal of urology.* 2013;20(6):7002-7007.

287. Robertson NL, Moore CM, Ambler G, et al. MAPPED study design: a 6 month randomised controlled study to evaluate the effect of dutasteride on prostate cancer volume using magnetic resonance imaging. *Contemporary clinical trials.* 2013;34(1):80-89.

288. Groenendaal G, van Vulpen M, Pereboom SR, et al. The effect of hormonal treatment on conspicuity of prostate cancer: implications for focal boosting radiotherapy. *Radiotherapy and oncology : journal of the European Society for Therapeutic Radiology and Oncology.* 2012;103(2):233-238.

289. Hotker AM, Mazaheri Y, Zheng J, et al. Prostate Cancer: assessing the effects of androgen-deprivation therapy using quantitative diffusion-weighted and dynamic contrast-enhanced MRI. *European radiology.* 2015;25(9):2665-2672.

290. Kim AY, Kim CK, Park SY, et al. Diffusion-weighted imaging to evaluate for changes from androgen deprivation therapy in prostate cancer. *AJR American journal of roentgenology.* 2014;203(6):W645-650.

291. Padhani AR, MacVicar AD, Gapinski CJ, et al. Effects of androgen deprivation on prostatic morphology and vascular permeability evaluated with mr imaging. *Radiology.* 2001;218(2):365-374.

292. Nakashima J, Imai Y, Tachibana M, et al. Effects of endocrine therapy on the primary lesion in patients with prostate carcinoma as evaluated by endorectal magnetic resonance imaging. *Cancer-Am Cancer Soc.* 1997;80(2):237-241.

293. Fradet V, Kurhanewicz J, Cowan JE, et al. Prostate Cancer Managed with Active Surveillance: Role of Anatomic MR Imaging and MR Spectroscopic Imaging. *Radiology.* 2010;256(1):176-183.

294. Park BH, Jeon HG, Choo SH, et al. Role of multiparametric 3.0-Tesla magnetic resonance imaging in patients with prostate cancer eligible for active surveillance. *BJU international.* 2014;113(6):864-870.

295. Thompson IM, Chi C, Ankerst DP, et al. Effect of finasteride on the sensitivity of PSA for detecting prostate cancer. *Journal of the National Cancer Institute.* 2006;98(16):1128-1133.

296. Weinreb JC, Barentsz JO, Choyke PL, et al. PI-RADS Prostate Imaging - Reporting and Data System: 2015, Version 2. *Eur Urol.* 2016;69(1):16-40.

297. Abd-Alazeez M, Kirkham A, Ahmed HU, et al. Performance of multiparametric MRI in men at risk of prostate cancer before the first biopsy: a paired validating cohort

study using template prostate mapping biopsies as the reference standard. *Prostate cancer and prostatic diseases.* 2014;17(1):40-46.

298. De Visschere PJ, Naesens L, Libbrecht L, et al. What kind of prostate cancers do we miss on multiparametric magnetic resonance imaging? *European radiology.* 2015.

299. Hambrock T, Somford DM, Hoeks C, et al. Magnetic resonance imaging guided prostate biopsy in men with repeat negative biopsies and increased prostate specific antigen. *The Journal of urology.* 2010;183(2):520-527.

300. Pondman KM, Futterer JJ, ten Haken B, et al. MR-guided biopsy of the prostate: an overview of techniques and a systematic review. *Eur Urol.* 2008;54(3):517-527.

301. Costa DN, Pedrosa I, Donato F, Jr., et al. MR Imaging-Transrectal US Fusion for Targeted Prostate Biopsies: Implications for Diagnosis and Clinical Management. *Radiographics : a review publication of the Radiological Society of North America, Inc.* 2015;35(3):696-708.

302. Cordeiro ER, Cathelineau X, Thuroff S, et al. High-intensity focused ultrasound (HIFU) for definitive treatment of prostate cancer. *BJU international.* 2012;110(9):1228-1242.

303. Chaussy C, Thuroff S. The status of high-intensity focused ultrasound in the treatment of localized prostate cancer and the impact of a combined resection. *Current urology reports.* 2003;4(3):248-252.

304. Maestroni U, Ziveri M, Azzolini N, et al. High Intensity Focused Ultrasound (HIFU): a useful alternative choice in prostate cancer treatment. Preliminary results. *Acta bio-medica : Atenei Parmensis.* 2008;79(3):211-216.

305. Napoli A, Anzidei M, De Nunzio C, et al. Real-time magnetic resonance-guided high-intensity focused ultrasound focal therapy for localised prostate cancer: preliminary experience. *Eur Urol.* 2013;63(2):395-398.

Publishing Agreement

It is the policy of the University to encourage the distribution of all theses, dissertations, and manuscripts. Copies of all UCSF theses, dissertations, and manuscripts will be routed to the library via the Graduate Division. The library will make all theses, dissertations, and manuscripts accessible to the public and will preserve these to the best of their abilities, in perpetuity.

Please sign the following statement:

I hereby grant permission to the Graduate Division of the University of California, San Francisco to release copies of my thesis, dissertation, or manuscript to the Campus Library to provide access and preservation, in whole or in part, in perpetuity.

Olga Stanoleinet — March 28, 2017

Author Signature — Date